MICROMECHANICAL MECHANISMS OF FETAL MEMBRANE FAILURE

by

Erinn Marie Joyce

Bachelor of Science, Mechanical Engineering, The Ohio State University, 2004

Submitted to the Graduate Faculty of

The Swanson School of Engineering in partial fulfillment

of the requirements for the degree of

Doctor of Philosophy

University of Pittsburgh

2009

UNIVERSITY OF PITTSBURGH

SWANSON SCHOOL OF ENGINEERING

This dissertation was presented

by

Erinn Marie Joyce

It was defended on

July 2, 2009

and approved by

John J. Moore M.D., Professor of Pediatrics, Departments of Pediatrics and Reproductive Biology

Steven Abramowitch Ph.D., Assistant Professor, Department of Bioengineering

Richard Debski Ph.D., Associate Professor, Department of Bioengineering

Joseph Mansour Ph.D., Professor, Department of Mechanical and Aerospace Engineering

Dissertation Director: Michael S. Sacks Ph.D., Professor, Department of Bioengineering

MICROMECHANICAL MECHANISMS OF FETAL MEMBRANE FAILURE

Erinn Marie Joyce, PhD

University of Pittsburgh, 2009

Premature birth is a major public health problem accounting for over 13,000 deaths and 30,000 surviving infants with life-long morbidity yearly. Preterm premature rupture of the fetal membranes (FM) is the initiating event leading to preterm birth of 40% of these premature infants. The mechanisms which cause FM failure and thereby rupture are not understood. A "weak zone" in the FM region overlying the cervix has recently been discovered, which demonstrates both biophysical weakness and concomitant biochemical evidence of tissue remodeling and apoptosis. This "weak zone" has been the subject of limited biomechanical investigation. A full understanding of FM failure requires a complete characterization of structural and biomechanical behavior of the FM at near/full term under sub-failure (forces well below that which induce rupture) and failure conditions as well as elucidating the biological factors which modulate its failure. The goals of this study were to (1) characterize the sub-failure structure-strength behavior of the FM under physiological loading conditions, (2) implement a structural constitutive model to investigate the sub-failure responses of FM, and (3) characterize the structural/strength sequelae during failure of the FM in the "non-weak" regions. The first two aims of this study established the baseline structure-strength relation of "non-weak zone" FM tissue. Specifically, the stress-strain relationship from an unloaded state up to failure was established. It was found that the FM behaves as an effectively isotropic material and that collagen fibers of the FM are recruited rapidly once they are loaded, which may be an important

mechanism in the facilitation of FM rupture. Finally, a novel membrane inflation device revealed that upon loading, there was a small increase in collagen fiber alignment, although not significant, and there was no change in collagen fiber direction. More importantly, FM failure occurs catastrophically, suggesting that particular collagen fibers are not predisposed to failure. The results obtained in this study further our understanding of this unique physiological event, failure, and provide a basis for establishing how the structure-function relationship of the FM is altered the "weak zone," which has unique mechanical properties that facilitates membrane rupture.

TABLE OF CONTENTS

LIST OF TABLES

LIST OF FIGURES

NOMENCLATURE

FM – fetal membrane

PROM – premature rupture of membranes

PPROM – preterm premature rupture of membranes

ECM – extracellular matrix

RER – rough endoplasmic reticulum

MMPs – matrix metalloproteinases

TIMPs – tissue inhibitor of metalloproteinases

SALS – small angle light scattering

OI – orientation index

NOI – normalized orientation index

MTM – maximum tangent modulus

PBS – phosphate buffered solution

PREFACE

Firstly, I would like to thank the Department of Bioengineering at the University of Pittsburgh and its chair, Dr. Harvey S. Borovetz. I would also like to thank Ms. Lynette Spataro and Mrs. Joan Williamson for their administrative assistance. Additionally, I would like to thank the collaborations that have grown from this Dissertation. In particular, I would like to thank Dr. John J. Moore for undertaking a very difficult problem facing women (preterm birth) and for his wisdom and input. I truly respect him as a person and scientist. Additionally, I would like to thank the members of this Dissertation committee for their guidance and contribution to this work. Finally, I would like to thank Dr. Michael S. Sacks for the opportunity to work in a competitive research environment and for his guidance and mentoring.

I would like to thank Dr. Jun Liao for his mentorship during the early years of my graduate career. Also, I would like to thanks Jennifer DeBarr for her help in histological sectioning and staining. A big thanks goes to the Moore Laboratory at Case Western Reserve University for their assistance in tissue procurement. In particular, I would like to thank Robert Moore for all his help with tissue procurement and technical input. I would further like to thank the administrative assistants of the ETM^{2}L for all their help: Anna Goldman, Lynn Ekis, Beth Markocic, and Karen Connor. I would like to thank the past and present members of the ETM^{2}L for their friendships and support over the course of the past 5 years. I would like to extend special thanks, in no particular order: Dr. Rebecca Long, Silvia Wognum, John Stella, Diana

Gaitan, Bahar Fata, Chad Eckert, Antonio D'Amore, David Schmidt, and Donna Haworth. Their friendship and support in the last few months of my graduate career has truly humbled me and attaining a Ph.D. without them would not have been possible.

Most importantly, I would like to thank my family and fiancé Jacob Moore. To my parents and sister, thank you for all your encouragement and support over the years. Jacob, thank you for always helping me see the humor in all situations. I love you and look forward to starting our future together.

1.0 INTRODUCTION

1.1 THE HUMAN FETAL MEMEBRANE

The fetal membrane (FM) is structurally soft membrane surrounding the fetus during gestation. A normal pregnancy requires physical integrity of the FM until term delivery, where timely rupture is a vital part of term labor [1]. During gestation, the FM is subjected to applied stresses and must support the bulk loads of the fetus and amniotic fluid as well as tolerate local deformations due to fetal movement. Additionally, the FM secretes substances both into the amniotic fluid and towards the uterus and guards the fetus against infection ascending from the reproductive tract. The FM is composed of two closely adherent layers, the amnion and the chorion, and consists of several cell types, including epithelial cells, mesenchymal cells, and trophoblast cells, embedded in a collagenous matrix.

1.1.1 FM formation

Fertilization begins when a spermatozoon makes contact with a secondary oocyte, which results in the formation of a one celled embryo. During the first 2-3 days of development, a cleaving embryo proceeds along the uterine tube by means of tubal contractions and movement of cilia [2]. Mitotic divisions occur at a rate of about one per day, increasing the number of cells or blastomeres, and each blastomere is considered totipotent [2]. The embryo enters the uterine

cavity after about half a week, where approximately 8-12 cells are present. When 8-16 cells are present, compaction occurs [3] [2]. During compaction the blastomeres become flattened against neighbors, which maximizes intercellular contact and minimizes intercellular spaces, resulting in a uniform cellular mass, the morula [2, 3]. Additionally cell-to-cell adhesion as well as gap and tight junctions first appear during compaction [3]. The embryo is termed the morula when 12 or more cells are present and until the blastocystic cavity appears. After 4-5 days and when 16-32 cells are present, a cavity can be detected in the cellular mass of the morula, and the morula is now termed a blastocyst (Figure 1-1).

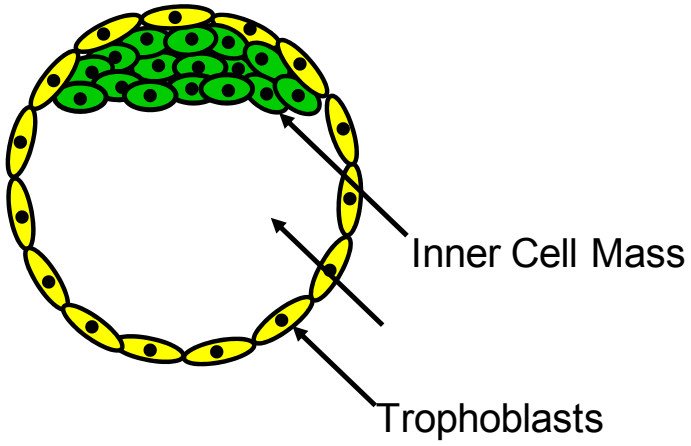

Figure 1-1. The blastocycst is composed of the inner cell mass and blastocystic cavity which are surrounded by trophoblast.

The appearance of the blastocyst demonstrates the differentiation into (1) the peripherally situated trophoblast cells and the first formation of epithelium and (2) embryonic cells proper, which forms the inner cell mass (Figure 1-1) [2, 4].

The trophoblast differentiates into two chief varieties (day 6): (1) an inner layer of cytotrophoblast, and (2) a multinucleated outer cell layer, the syncytiotrophoblast [2, 4, 5]. The

cytotrophoblast surrounds the blastocystic cavity [2]. The syncytiotrophoblast develops from the cytotrophoblast, and it synthesizes and secretes chorionic gonadotrophin and other placental hormones [2, 4]. Additionally, the syncytiotrophoblast starts to invade the connective tissue of the uterus [5].

Prior to implantation, the inner cell mass begins to differentiate into external and internal cell layers [5]. The two layers are termed the epiblast (ectoderm), which is the external cell layer, and the hypoblast (endoderm), which is the internal cell layer [2, 5]. The epiblast gives rise to the endoderm [2, 5]. Eventually, the combination of the epiblast and hypoblast forms the embryonic disc (occurs soon after implantation; Figure 1-2a) [2, 6]. The fluid within the blastocystic cavity is believed to be derived from the trophoblast [2].

At 6 days, the blastocyst begins to attach to the uterine lining (endometrium), which marks the beginning of implantation [2, 5]. Once the blastocyst begins to penetrate the uterine epithelium, the endometrium is termed the decidua [2]. Decidualization, or the decidual reaction, is the series of endometrial changes that occur in response to invading blastocyst into the endometrium [2, 7]. The endometrium begins to store glycogen and lipids, which serve as energy sources for the fetus [2, 7].

The first indication of mesenchym is the production of extra-embryonic mesoblast from a caudally situated area of proliferation at approximately 7-8 days. The combination of the trophoblast fronting the uterine tissue and the extra-embryonic mesoblast is known as the chorion (8-12 days; Figure 1-2). Originally the trophoblast is solid (7-8 days; Figure 1-2 a) [2]. However, by day 9, the trophoblast layer forms lacunae as it extends into the endometrium (8-10 days; Figure 1-2b) [2, 8]. As the synctium of the trophoblast invades the endometrium, it erodes

and penetrates the maternal sinusoids, or blood vessels, which then spills the maternal blood into the lacunae (10-12 days; Figure 1-2c) [2, 8].

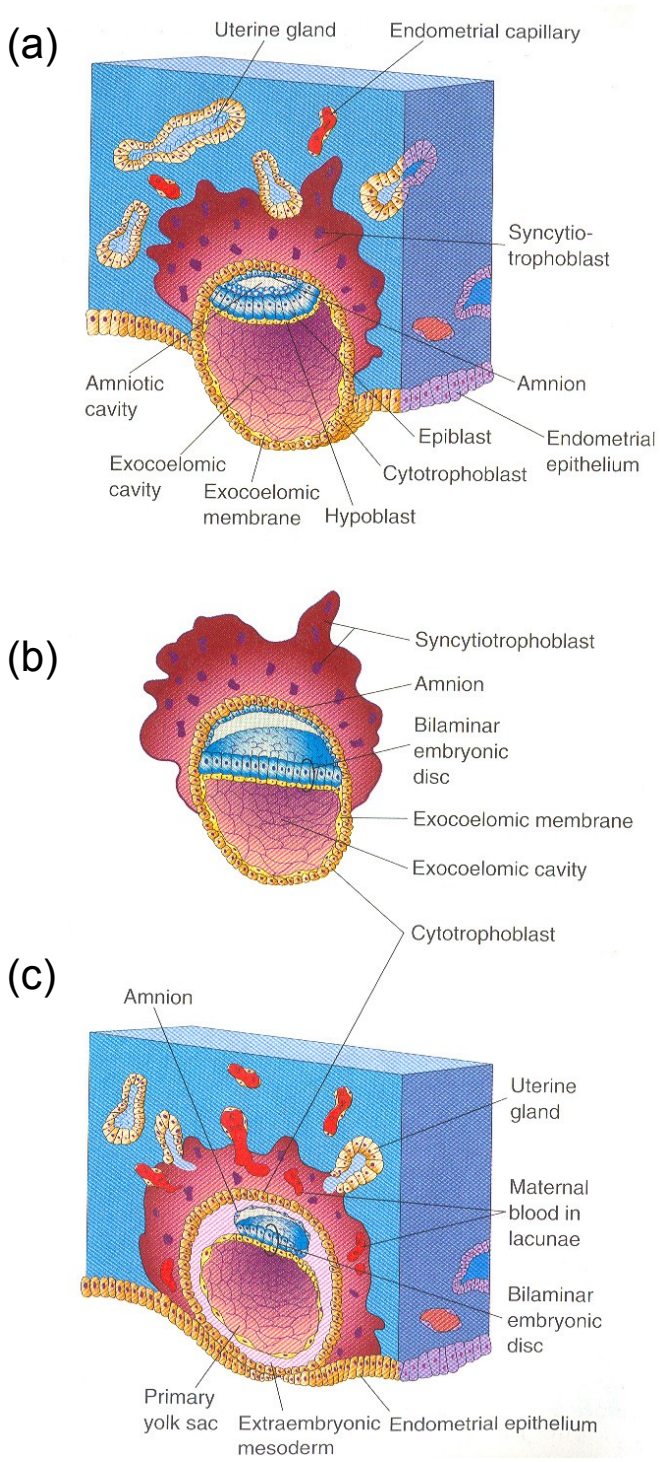

Figure 1-2. (a) The trophoblast is originally solid (7-8 days). (b) An enlarge view of an older blastocyst removed from the endometrium. (c) However, by day 9, the trophoblast layer forms lacunae. Eventually, the trophoblast invade, the endometrium and erodes and penetrates the maternal blood vessels causing maternal blood to fill the lacunae and forms the basis for placental circulation [2]. (Reprinted with permission from [9]. Copyright @ Saunders, 2003.)

This junction of the maternal blood vessels and trophoblast is the basis of placental circulation [2]. As the lacunae coalesce, maternal blood begins to flow through them, and exchange of oxygen, carbon dioxide and nutrients occurs [2, 8]. Note that while the lacunae usually contain blood, but it has been shown that the intervillous space lacks blood flow during the first trimester and is filled mainly with acellular fluid, probably plasma [2].

The amniotic cavity appears within the inner cell mass, conceivably by rearrangement of epiblastic cells (7-8days; Figure 1-2), and is enclosed by the amnion [2, 5]. The cavity is bounded by the epiblast, and dorsally, by a layer of amniotic ectoderm [2]. On the ventral aspect of the embryonic disc, extra-embryonic endoderm grows around to enclose a cavity termed the primary umbilical vesicle (or yolk sac) (Figure 1-2c) [2].

The placenta is a device which allows for intra-uterine pregnancy to occur, and thus, facilitates fetal growth. The placenta synthesizes a large variety of hormones and functions in nutrition, respiration, secretion, and excretion [2]. Chorionic villi are the basic feature of the placenta and form at approximately 17-23 days [2]. Solid cords of cytotrophoblast, or cytotrophoblastic clumps (Figure 1-3), follow the syncytiotrophoblast into the endometrium and penetrate into blood-filled lacunar spaces as primary chorionic villi, or stem villi (Figure 1-3) [2, 10]. Thus, these villi contain a cytotrophoblast core, which is covered by syncytial cells (Figure 1-3) [2, 10]. The mesoblast penetrates the center of cytotrophoblastic clumps and forms the secondary chorionic (stem) villi (Figure 1-3) [10]. As a result, the secondary chorionic villi contain a core formed by mesoblastic crests, cytotrophoblastic caps, and are covered by syncytial cells [10]. Early in the embryonic period, some chorionic villi develop dense masses of trophoblastic cells at their tips [2]. These cytrophoblastic cell columns make contact with the eroded endometrium and spread out as part of the lining of the intervillous space (the

cytotrophoblastic shell or early basal plate) (Figure 1-3) [2]. This shell firmly attaches the placenta to the endometrium [10]. Later the villous cores extend through the cell columns to become anchored to the decidua (anchoring villi) (Figure 1-3) [2]. Most villi, however, retain free tips in the intervillous space (floating villi) (Figure 1-3) [2, 10]. The capillaries within the villi become connected with the embryonic heart via of the umbilical vessels [2]. The arrangement of the villi is that of a deciduous tree with roots in the chorionic plate and trunk; branches and twigs, suspended in the pool of maternal blood, occupy the intervillous space [2].

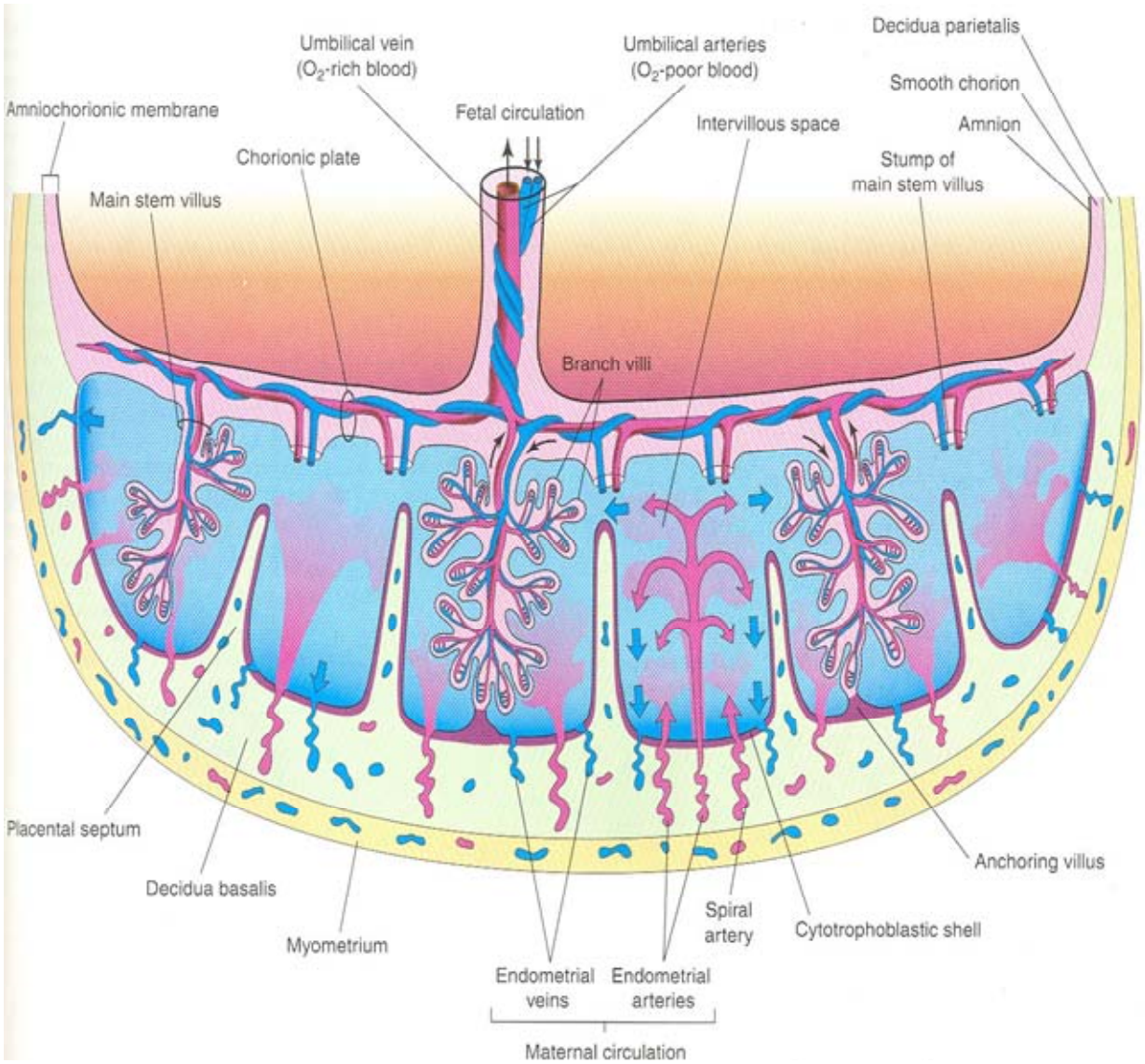

Figure 1-3. Simplification of the formation of the placenta. In summary, Cytotrophoblastic clumps follow the syncytiotrophoblast into the endometrium and penetrate into the blood-filled lacunar spaces as stem villi. The mesoblast penetrates the center of the cytotrophoblastic clumps and form secondary stem villi. Some of the chorionic villi form dense masses of trophoblastic cells at their tips forming cell columns, which make contact with the eroded endometrium and spread out as part of the lining of the intervillous space and form the cytotrophoblastic shell). Later the villous cores extend through the cell columns forming the anchoring villi. However, most villi retain free tips in the intervillous space and are termed the floating villi. (Reprinted with permission from [9]. Copyright @ Saunders, 2003.)

At 56 days, the extra-embryonic coelom, the space between the mesoderm of the chorion and the mesoderm covering the yolk sack, is obliterated, and the uterine cavity becomes diminished (Figure 1-4). By 17-20 weeks, the amnion and chorion become fused (Figure 1-4) [11].

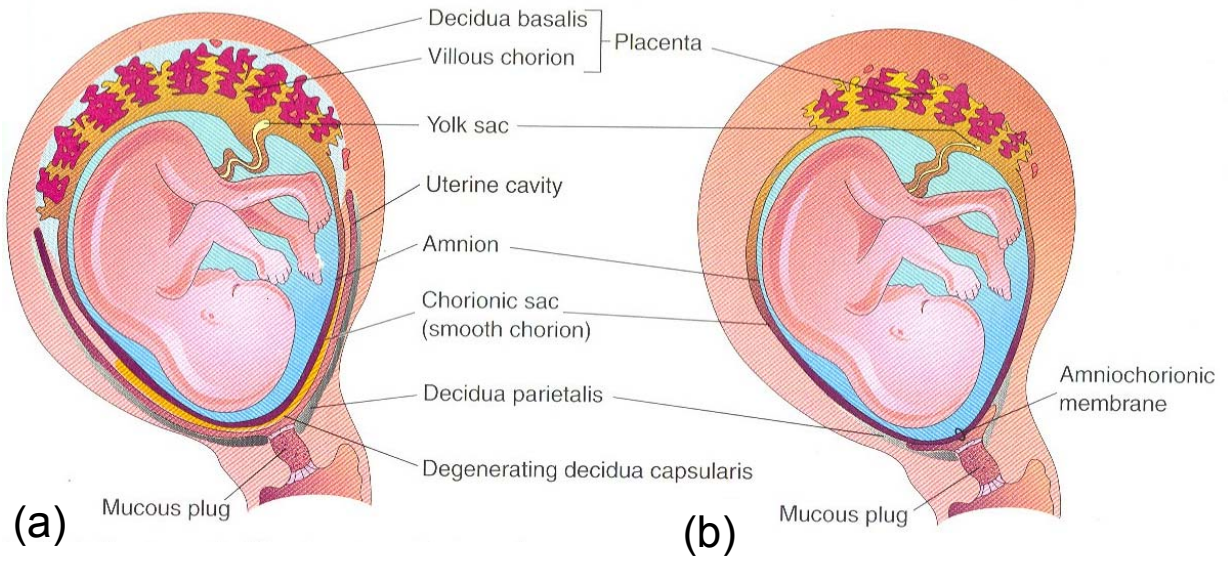

Figure 1-4. (a) Late in the first trimester, the space between the mesoderm and the chorion is obliterated and the uterine cavity is diminished. (b) Also, by 17-20 weeks, the amnion and the chorion fuse forming the amniochorionic membrane, or the fetal membrane. (Reprinted with permission from [9]. Copyright @ Saunders, 2003.)

1.1.2 FM layers and cell types

The FM is a bilayer structure composed of the amnion layer and the choriodecidua layer. The choriodecidua layer is thick and more cellular, and the amnion layer is stiff and strong. The amnion layer accounts for ~20% of the FM thickness but dominates the mechanical response of

the FM[12]. It has been confirmed that the amnion and the choriodecidua layers contain collagen types I and III in addition to collagen types IV and V [13].

The amnion layer is avascular and is composed of 5 sublayers (Figure 1-5, Figure 1-6) [14]. The innermost layer, nearest the fetus, is composed of epithelial cells (Figure 1-5, Figure 1-6a), which secrete collagen types III and IV and noncollagenous glycoprotiens, such as laminin, nidogen, and fibronectin, forming the subsequent basement membrane (Figure 1-5) [14]. The compact layer of connective tissue is adjacent to the basement membrane, forming the fibrous framework of the amnion (Figure 1-5, Figure 1-6) [14]. The collagens of the compact layer, types I and III, are secreted in parallel bundles from the mesenchymal cells in the subsequent fibroblast layer and are responsible for the mechanical integrity of the amnion (Figure 1-5, Figure 1-6) [14, 15]. Collagen types V and VI form fibrous connections between the interstitial collagens (types I and III) and the basement membrane [14]. In addition to mesenchymal cells, the fibroblast sub-layer of the amnion layer contains macrophages [14]. Below the fibroblast layer is the intermediate spongy layer, which lies between the amnion and the chorion layer and allows the amnion to slide on the underlying chorion (Figure 1-5) [14]. The spongy layer is composed of hydrated proteoglycans and glycoproteins along with a nonfibrillar meshwork of mostly type III collagen [14].

The chorion layer is thicker than the amion layer and contains a connective tissue sublayer and cytotrophoblasts (Figure 1-5) [14]. The cytotrophoblast cells are surrounded by collagen type IV [14]. The chorion layer is firmly adhered to the maternal decidua, where the decidual cells are surrounded by collagen types III, IV, and V. Thus, when the fetal membranes separate from the uterus at delivery, some adherent uterine tissue, part of the decidua, remains attached to the chorion [16]. The resulting layer is the “choriodecidua” layer (Figure 1-5).

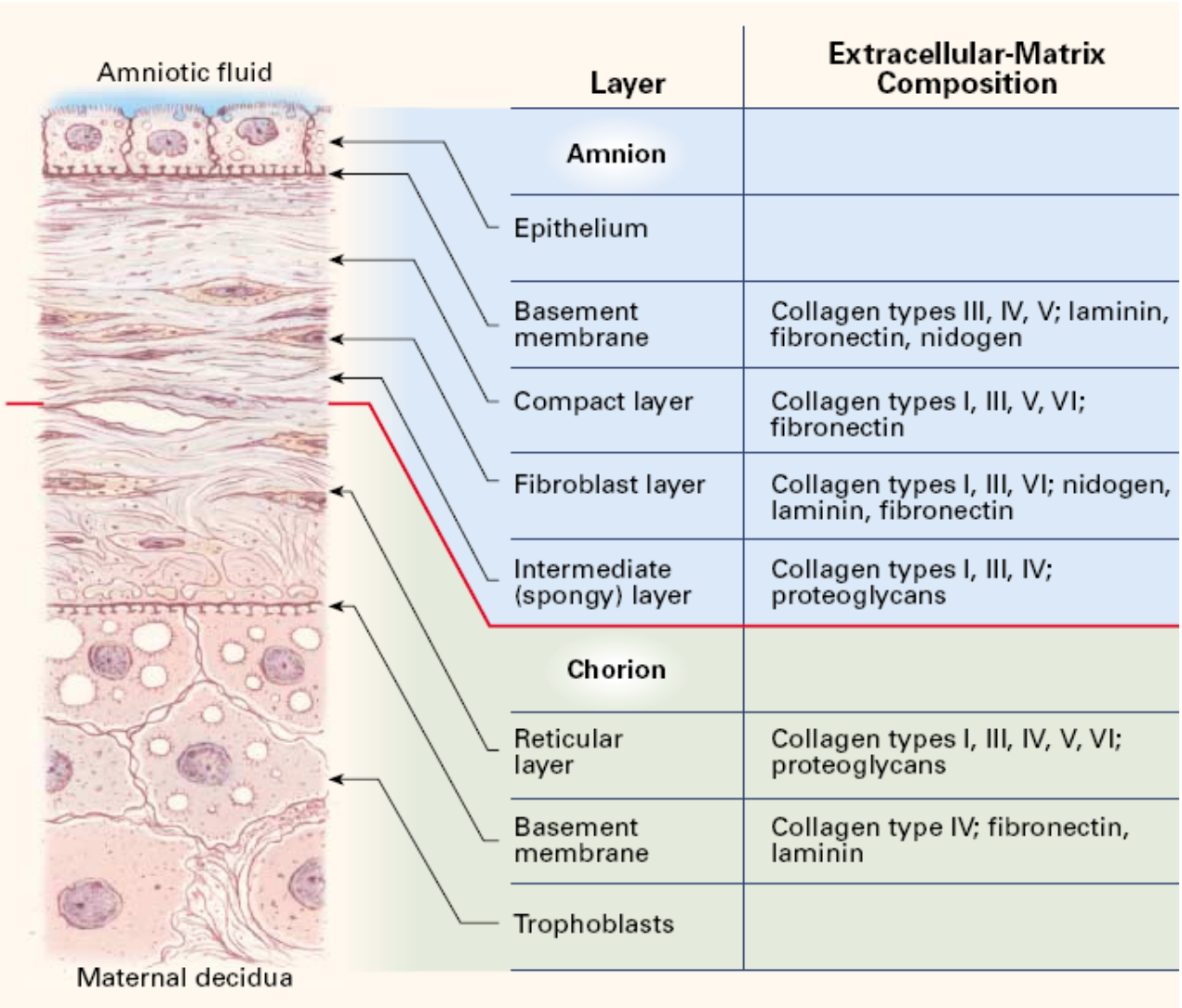

Figure 1-5. Schematic representation of the various sublayer of the FM. (Reprinted with permission from: Parry, S., Strauss, J.F., Premature Rupture of The Fetal Membranes. New England Journal of Medicine, 1998. 338(10): p. 663-670. Copyright @ 1998 Massachusetts Medical Society. All rights reserved.)

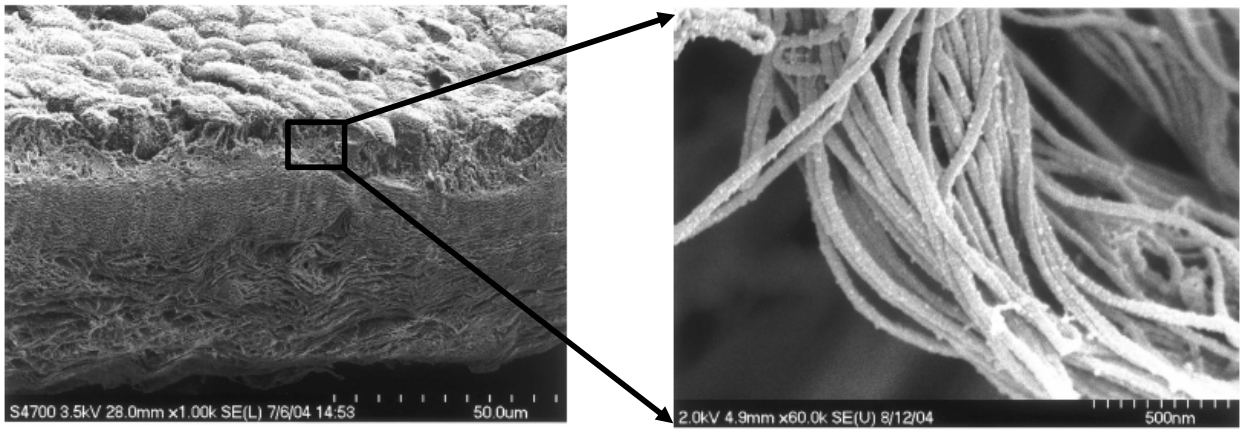

Figure 1-6. (a) Scanning electron micrograph of the amnion layer. Note the dense epithelial cell layer followed by a dense collagen network. (B) Below the dense cellular layer is the basement membrane and compact layer. The compact layer contains parallel bundles of collagen fibrils and provides mechanical integrity. (Reprinted with permission from [15]. Copyright @ Materials Research Society, 2005)

1.2 THE PROBLEM: PREMATURE RUPTURE OF MEMBRANES

Premature birth is a major public problem accounting for over 13,000 deaths and 30,000 surviving infants with life-long morbidity yearly [17-19]. Preterm rupture of membranes is a major cause of preterm birth and is associated with infant morbidity and mortality, with the greatest risk of mortality and morbidity in infants born at earlier gestational ages [1, 20]. Preterm premature rupture of the FM (PPROM) occurs prior to 37 weeks' gestation and prior to the onset of the contractions of labor, and PPROM is the initiating event leading to preterm birth in about 40% of premature infants [21-23].

Although significant progress has been made recently [1], the physiological mechanisms which cause membranes to rupture, term or preterm, are not completely understood. In order

understand FM failure, and thereby provide insight into how we may anticipate, and when appropriate, intervene to prevent preterm FM rupture, we need to elucidate:

1. How the FM mechanically fails
2. What biological factors modulate its failure

1.3 COLLAGENOUS SOFT TISSUES

The extracellular matrix (ECM) of connective tissues is a complex composite material, which is comprised of insoluble fibers, microfibrils and a wide range of soluble proteins and glycoprotiens. The ECM provides tissues with their specific mechanical and physiochemical properties as well as providing scaffolding for cell attachment and migration [24]. The most abundant protein in the body and the predominant component of the ECM are members of the collagen family of proteins, which form the major structural elements of connective tissues [24, 25]. Collagens are the major structural component of all connective tissues as well as the interstitial tissue of virtually all functional organs. Collagens contribute to the stability of the tissues and organs and maintain their structural integrity [26]. The physiological roles of collagen are achieved by aggregates of the molecules, and construction of these aggregates is vital to the integrity of a tissue. Thus, while the focus of this study was at the collagen fiber level of the FM, it is important to understand the how the collagen fiber is formed from the microscopic level (molecule) to the macroscopic level (tissue).

All types of collagens contain a unique tertiary structure called the collagen triple helix molecule, or tropocollagen (Figure 1-7). The triple helix molecule is composed of three individual α-chains, which coil into left handed minor helices. The three chains, staggered by

one residue relative to each other, intertwine with one another to form a right handed super helix [24, 25, 27]. The triple helical regions have a general structure comprised of tandem repeats of Gly-X-Y tripeptide units (Figure 1-7) [24, 25]. The X and Y positions are occupied by proline and hydorxyproline residues, respectively [25]. The glycine residue, which is the smallest amino acid, allows close packing along the central axis and hydrogen bonding between the three chains. The number of Gly-X-Y repeats varies between collagen types. The Gly-X-Y repeat in fibrillar collagen is continuous over the ~1000 amino acid length of the three α-chain subunits of the molecule. However, non-fibrillar collagens contain imperfections and non-collagenous interruptions in the Gly-X-Y sequence [24].

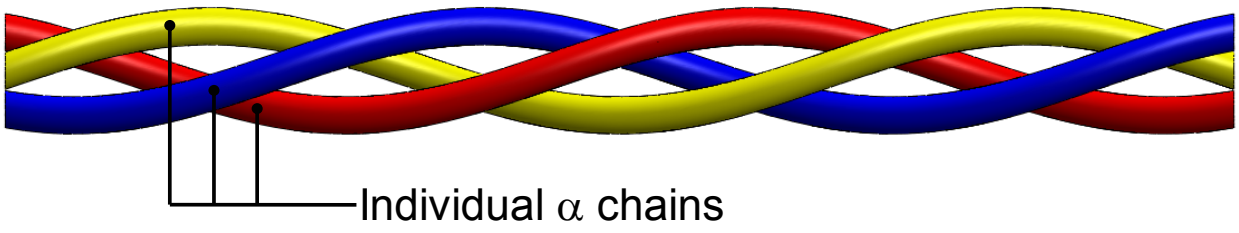

Figure 1-7. Schematic representation of the triple helix molecule, or tropocollagen. Tropocollagen consists of three individual α chains, which are left handed helices. The chains are coiled around each other to form a right handed helix. The three chains are staggered by one residue relative to each other. Hydrogen bonds form between opposing residues in different chains in order to stabilize the triple helix.

To date, 19 different collagen types have been identified, which are comprised of at least 33 individual genetically distinct polypeptide chains [24]. Collagens can be grouped into various categories based on their structures and supramolecular organizations. For example, collagens can be classified as fibril-forming collagens and basement membrane collagens, in addition to others with unique functions [26]. While there is a large diversity in the collagen family, the

supramolecular structures maintain the physical integrity of tissues and organs [28]. Additionally, collagen fibers have the ability to bind cells and thereby influence their migratory behavior as well as their differentiation and biosynthetic capabilities [28]. The most abundant and widespread family of collagens, which comprises approximately 90% of the total collagen, is represented by the fibril-forming collagens [26]. Collagen types I, II, III, and V are fibrillar collagens, which provide most of the biomechanical properties essential for the function of various organs, where collagen type IV assembles into meshworks restricted to basement membranes [26]. Collagen type I is the most abundant collagen and represents the principle fibrillar component of many tissues and is considered a heterotrimer of two identical α1(I) chains and one α2(I) chain [24, 27]. Collagen type I is a major component of tendon and bone [27]. Collagen type I provides tensile stiffness to most organs and defines biomechanical properties concerning load bearing, tensile strength, and torsional stiffeness in bone [26]. A rare form collagen type I has been identified as collagen type I trimer, which consists of three identical α1(I) chains [24, 27]. Collagen type II is the predominant collagen in cartilage and is comprised of three α1(II) chains [27]. Collagen type II is similar in size and biomechanical properties to that of collagen type I [26]. Collagen type III can be found in skin, blood vessels, synovial, and placental tissues [27], and is considered a homotrimer with three α1(III) chains. It is an important component of reticular fibers in interstitial tissues such as lungs, liver, dermis, spleen and vessels [26]. Collagen type V accounts for 10% of the total collagen in any tissue, and although it is thought to be of interstitial origin, it has not been well characterized. It is comprised of two α1(V) and one α2(V) chains. Collagen type V typically forms heterofibrils with collagen type I and type III and contributes to the organic bone matrix, the corneal stroma, and the interstitial matrix of muscles, liver, lungs, and placenta [26]. Finally, collagen type IV is

determined to be a basement membrane collagen and contains a more flexible triple helix structure [26, 27]. Originally, collagen type IV, was thought to be comprised of three α1(IV) chains. However, recent studies have suggested that collagen type IV consists of two α1(IV) chain and one α2(IV) chains [27].

1.3.1 Structure of collagen

Collagen synthesis is a complex multi-step process involving gene transcription within the nucleus to aggregation of collagen heterotrimes/homotrimers into larger scale super-structures. The first step in collagen formation is the production of specific m-RNAs for different pro-collagen chains called pre-proα chains. Different m-RNAs are synthesized in order to produce different forms of collagen. As the pre-proα chains are synthesized in the rough endoplamic reticulum (RER), important co-translational events occur during this process. More specifically, proline residues are hydroxylated via 3-proline hydroxylase and 4-proline hydroxylase resulting in hydroxylysine, and lysine is hydroxylated by lysyl hydroxylase resulting in hydroxylysine. Note that the degree of hydroxylation varies between tissues and probably with the availability of substrate, rates of synthesis and turnover, enzyme concentration, and time that the molecule remains in the presence of the hydroxylating enzymes [29]. Next, hydroxylysine is glycosylated by galactosyl-transferase, and glucose is added by a glucosyltransferase. A pre-proα chain containing a large N-terminal hydrophobic signal is the final translational product. This N-terminus signal peptide is probably removed by an intramembranous endopeptidase after facilitating the transfer of the pre-proα chain into the lumen of the RER, resulting in proα chains. However, the proα chains must be properly aligned to form the triple helix. It is unclear whether

alignment occurs when the polypeptide chains are still attached to the ribosome or if they have detached, or if the N-terminus peptide plays a role in this connection. Nonetheless, the appropriate cysteine residues should be aligned side by side as a prerequisite for the formation of disulfide bonds that link the individual proα chains at the C-terminus end. Disulfide bond formation occurs before triple helix formation. Formation of a nucleus of triple helical conformation at the C-terminus end occurs and nucleation progresses in a zipper-like manner to the N-terminus forming procollagen [30].

The procollagen molecule emerges from the RER and progresses towards the Golgi apparatus, where it is packaged into vesicles. The vesicles then fuse with the cell membrane, and the procollagen molecule is secreted into extracellular space through exocytosis. It is likely that the basic mechanism of triple helix formation is similar for each type collagen molecule [26]. However, the steps required after secretion of procollagen to form supramolecule appears to vary between collagen types.

For fibrillar collagens, after secretion into the extracellular space, the nonhelical peptide regions are cleaved by procollagen peptidase and tropocollagen is formed (Figure 1-7, Figure 1-8a). The next stage in collagen development is the formation of the collagen fibril. Five rows of tropocollagen molecules are aggregated to form a microfibril, where each molecule is quarter-staggered 1D unit in relation to its neighbor (Figure 1-8b) [29, 31]. Each tropocollagen molecule is 4.4D long, which results in a 0.6D gap between consecutive molecules in the same row (Figure 1-8b) [31]. The tropocollagens are intertwined in a slow left-handed helical manner forming a "super-helix" [31, 32]. Orderly packing of the tropocollagen molecules into the 5 stranded microfibiril is accomplished by hydrophobic interactions between amnio acids in adjacent rows (maximum interactions occur when molecules are displaced by 234 residues or

1D). Next, a large number of microfibrils are packed together for form a fibril, where some evidence suggests that microfibrils intertwine in a right-handed helical pattern with a pitch of about 1000nm to form a fibril [31]. The fibril displays a characteristic longitudinal banding pattern with a repeat of 67 nm (1D). The fibril banding pattern is due to precise replication of the peptide sequence of the tropocollagen chains and to their quarter-stagger microfibril packing arrangement (Figure 1-8c) [33]. The fibril diameter was found to be ~50-200 nm [31].

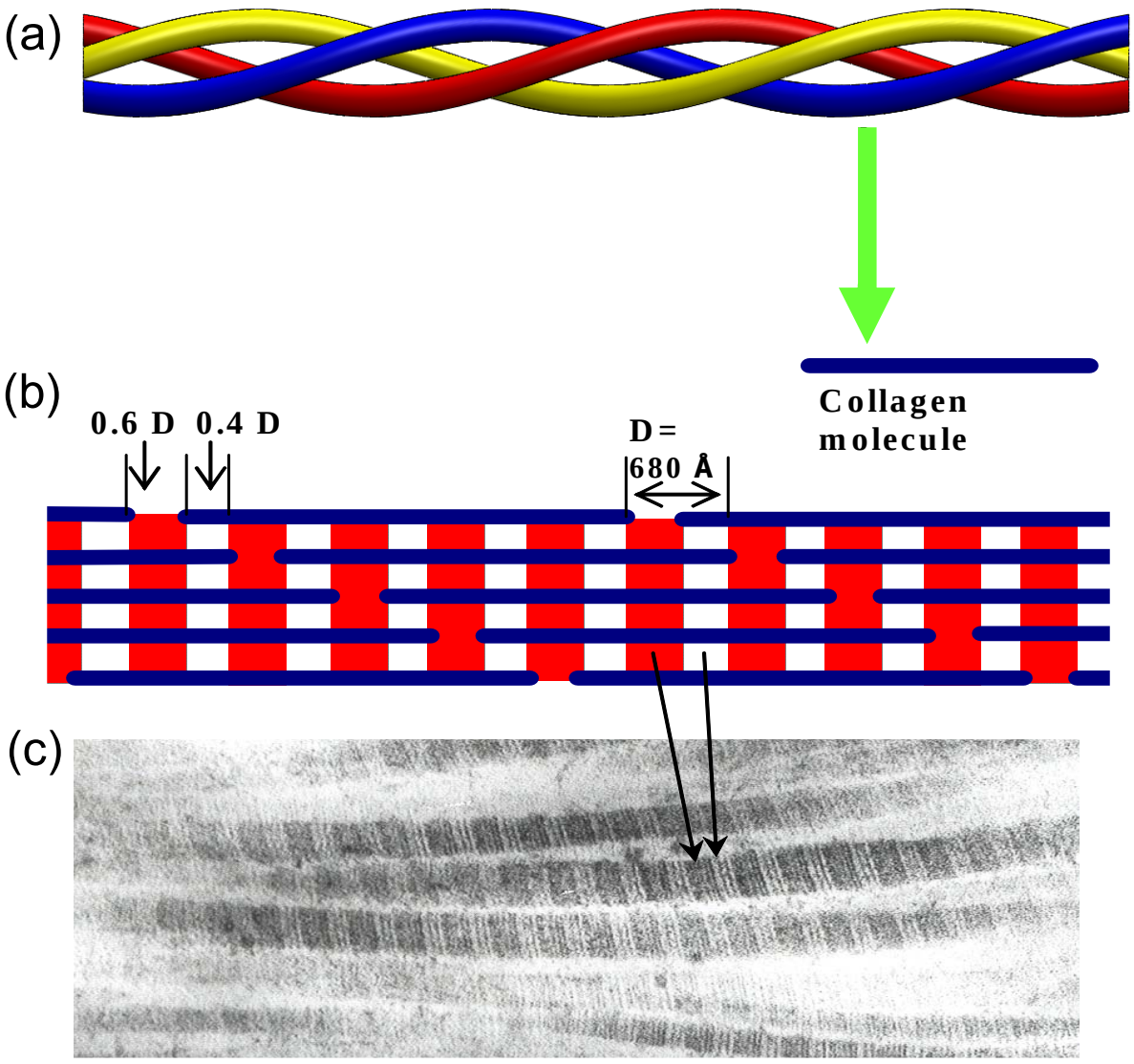

Figure 1-8. Schematic representation of the formation of a collagen fibril. Five rows of (a) tropocollagen molecules aggregate to form a (b) microfibril. Each molecule is quarter-staggered 1D unit in relation to its neighbor. Each tropocollagen molecule is 4.4D long, which results in a 0.6D gap between consecutive molecules in the same row. (c) Next, a large number of microfibrils aggregate to form a fibril. A transmission electron micrograph (TEM) of the fibril depicts the a characteristic longitudinal banding pattern with a repeat of 67 nm (1D) due to precise replication of the peptide sequence of the tropocollagen chains and to their quarter-stagger microfibril packing arrangement.

The next aggregate in collagen formation is the collagen fiber. The collagen fiber involves lateral association and axial displacement of molecules arranged in parallel [29]. Collagen fibrils are organized into tissue-specific suprafibrillar structures. Fibrils are aggregated side-by-side in parallel bundles to form fibers in tissues such as tendons and ligaments, but individual fibrils form a network in tissues such as skin, cartilage, and cornea [34, 35]. Fiber diameters can range from 200 nm to 12000 nm [36]. The crimp structure, which is the alternating dark and light banding pattern apparent between crossed polarizer, can be observed at this level of collagen aggregation.

Basement membrane collagen, collagen type IV, differs from interstitial fibril-forming collagen in that when the procollagen is secreted into the extracellular space, the nonhelical peptide regions are not cleaved by procollagen peptidase. Thus, the non-triple-helical domains are retained. The collagen type IV molecule consists of a 360-nm long triple helix which is bordered at its N-terminus by a short non-triple-helical interruption followed by the 30-nm long helical 7S domain and at its C-terminus by the globular NC1 domain [37]. After secretion, the collagen molecules interact to form supramolecular assemblies form [37]. Four collagen IV molecules interact by means of their 7S domains to form a spider-like structure and two molecules bind each other in a head-to-head fashion by way of their NC1 domains. A combination of these interactions forms a loose network. Additionally, lateral aggregation of collagen type IV occurs, which results in a layered hexagonal planar array. Lateral associations and supramolecular helices can be seen under ultrastructural investigations of the human amniotic basement membrane [37].

1.3.2 Collagen packing theories

In any structure, whether it is natural or synthetic, the ultimate strength of tension-bearing elements depends on the substance they are composed of and their cross-sectional area [38]. Mechanical and physical properties of a tissue are dependent on a hierarchical spatial arrangement of collagen fibrils [39]. Thus, considering the correlation of the inner architecture of collagen fibrils, their diameter, and their spatial layout with functional requirements, fibril formation from their molecular precursors are of concern [38]. Electron micrographic and X-ray diffraction data provide evidence that there is a regular arrangement of molecules that may result from ordered packing within collagen fibrils. However, while several theories exist, it is still unknown how the fibrils are formed from their molecules. It has become apparent that shape of the fibril is dependent on where the molecule is added. Ramachandran (1967) originally suggested a hexagonal packing of molecules but realized that this would result in hexagonal fibrils, which are thought to be round (Figure 1-9). Thus, the suggested a cylindrical structure or a modified cylindrical structure, where the molecules were in a spiral orientation (Figure 1-8) [40].

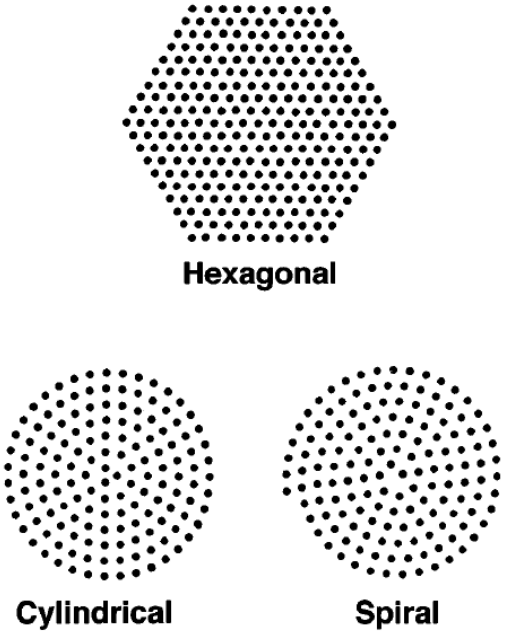

Figure 1-9. Possible modes of collagen molecule packing as proposed by Ramachandran. (Reprinted from Prockop and Fertala, The Collagen Fibril: The Almost Crystalline Structure. Journal of Structural Biology, 1998. 122: p. 111-118. Copyright @ Academic Press, 1998.)

Galloway (1985) latter suggested that the molecules were packed into cylindrical arrays (Figure 1-10) [40]. In this model the outer layers become "lattice-like and allow packing of some molecules as quasi-hexagonal unit cells" (Figure 1-9) [40]. However, this theory was disputed by Silver, Miller and Prockop (unpublished observations) due to large discontinuities between the unit cells in the outer layers of the model [40].

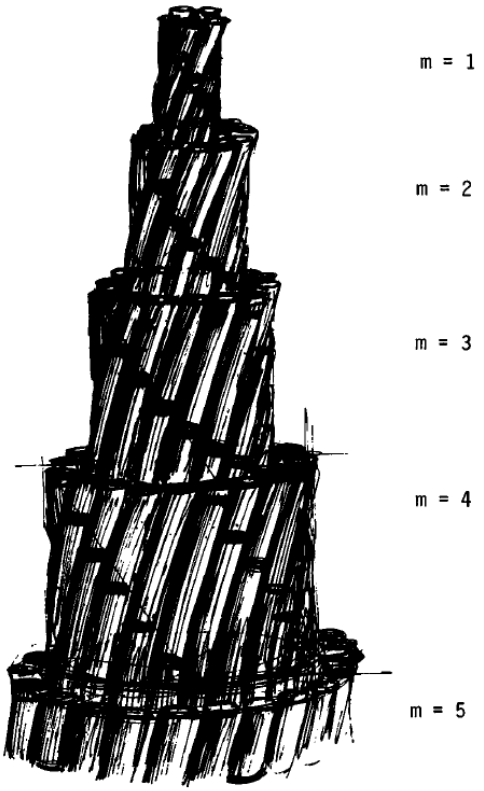

Figure 1-10. Galloway's proposed model for collagen fibrils. Galloway suggested that the collagen molecules were packed in concentric cylindrical arrays. . (Reprinted from Prockop and Fertala, The Collagen Fibril: The Almost Crystalline Structure. Journal of Structural Biology, 1998. 122: p. 111-118. Copyright @ Academic Press, 1998.)

Prockop's group performed a study wherein they developed procedures to generate collagen molecules that had a solubility of less than 1 μg/ml and that spontaneously assembled in to tightly packed collagen fibrils under physiological conditions [40]. They found that fibril formations were entropy driven, which was in agreement with previous findings, and fibril assembly demonstrated features typical of a crystallization process. Additionally, it was demonstrated that the diameters of fibrils varied with temperature. Kadler (1990) used dark field microscopy on relatively large diameter fibrils formed at 30^{o}C and found that the first structure formed had a blunt end and a pointed end [40]. Moreover, fibrils grew by extension of the

pointed tips with no apparent change in the diameter of the initial structure. Scanning transmission electron microscopy (STEM) analysis demonstrated that the pointed tips showed a linear increase in mass with length, and the tips were paraboloids [40]. These finding prompted speculation as to how the symmetry of the tips was maintained as the fibrils grew. Thus, Silver *et al.* (1992) developed a model for tip growth based on a helical structure (Figure 1-11) [40].

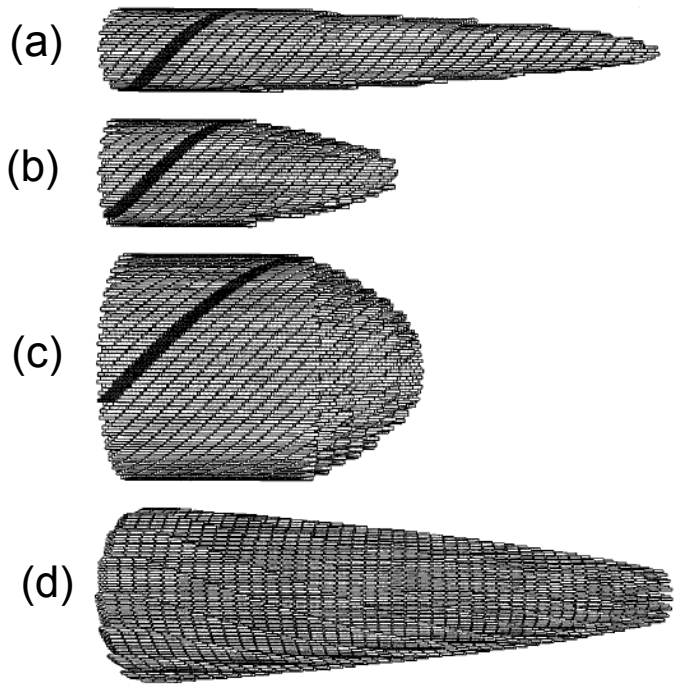

Figure 1-11. Computer simulation of helical models proposed by (a-c) Silver et al. and the spiral model proposed by (c) Humes et al. It has become apparent that shape of the fibril is dependent on where the molecule is added. (Reprinted from Prockop and Fertala, The Collagen Fibril: The Almost Crystalline Structure. Journal of Structural Biology, 1998. 122: p. 111-118. Copyright @ Academic Press, 1998.)

Parkinson *et al.* (1995) then developed a model based on the principle of limited diffusion, which is seen in electrochemical depositions or snowflake formation. This model assumed that molecules had a tendency to bind through D period overlaps. The model predicted aggregates that displayed common features of collagen fibrils. Specifically, these feature included an elongated morphology, a preference for tip growth, and a linear relationship between

mass and distance from the tip. Hulmes *et al.* (1995) went on to develop a model that combined the single crystal theory proposed by Fraser, Miller, and associates, the limited diffusion theory proposed by Parkinson *et al.,* and the hard disk model proposed by Fratzl. While many models have been proposed, it remains unclear which model is most accurate [40]. A summary of these models can be found in Table 1-1.

Table 1-1. Summary of models proposed for fibril packing. (Reprinted from Prockop and Fertala, The Collagen Fibril: The Almost Crystalline Structure. Journal of Structural Biology, 1998. 122: p. 111-118. Copyright @ Academic Press, 1998.)

	Fit to Criteria			
Model	**X-ray of round fibril**	**Growth from tips**	**Stepwise increase in diameters**	**Micro fibrillar substructures**
1. Single crystal (Fraser/Miller/Wess)	**No**	**No**	**No**	**Yes**
2. Hard disk/liquid-crystal/limited diffusion (Fratzl, Parkinson)	**No**	**Yes**	**No**	**No**
3. Spiral (Hulmes)	**Yes**	**Yes**	**No**	**Yes**
4. Cylindrical:				
a. Galloway *et al.*	**No**	**No**	**Yes**	**Yes**
b. Silver *et al.*	**No**	**Yes**	**Yes**	**Yes**
c. Hulmes *et al.*	**Yes**	**No**	**Yes**	**Yes**

1.3.3 Collagen crimp

When tendons are placed between crossed polarized and viewed under a light microscope, an alternating dark and light banding appears when the tendon is placed parallel and perpendicular to the polarizer direction [41]. This banding pattern is referred to as crimp. Crimp is not restricted to tendons and can be found in the fibrillar collagens (i.e. collagen types I-III) of most mammalian tissues with the exception of bone and articular cartilage [42]. Although collagen crimp is observed at the fiber level, Diamant *et al.* determined that fiber crimp is a property of individual collagen fibrils [41, 42]. In spite the ubiquitous nature of collagen crimp, the cause of crimping has yet to be determined. An early explanation for collagen crimp was that contraction of elastin fibers within the collagen structure induced crimp [43]. This theory was dispelled because rat tail tendon, which does not contain elastin, clearly demonstrates collagen crimp [43]. Some speculate that contraction of mucopolysaccharide matrix, in which the fibrils are embedded, causes the fibrils to buckle [43]. Also, determination of the crimp pattern, a result of fibril aggregation, is not trivial and has led to various theories (Figure 1-12) [42]. Various models have been proposed for the crimp pattern found in tendons and ligaments. The models propose are as follows: (1) a flat crimping ribbon model (Figure 1-12a) [44], (2) planar waviness model (Figure 1-12b) [33, 41, 45], (3) a skewed register model (Figure 1-12c) [46], and (4) a helix model [47].

The flat crimping ribbon model assumes that fibrils aggregate laterally to form a tendon unit, and the tendon units are bundled together with elastic fibers and fibroblasts resulting in the macroscopic tendon. This model assumes that the fibrils have a ribbon like cross-section that results in the flattened cylinder cross-section of the tendon unit, which gives rise to the horizontally elongated tendon cross-section. Polarizing microscopy demonstrated that the

ribbons crimp all in phase, with their ribbon planes parallel throughout the tendon. Note, that the flat crimping ribbons are thought to be responsible for the extinction bands that are evident under polarizing light.

It the planar waviness model, fibrils are not straight and follow a wavy or zig-zag crimped course and are packed cylindrically to form a collagen fiber [33, 45]. Diamant *et al*. (1972) claim that the fibril cross-sectional appears cylindrical as opposed to a flat ribbon, which was claimed by Baer *et al.* (1976) [41, 44]. Diamant *et al*. employed polarizing microscopy and demonstrated that collagen fibers of native tendons display a planar zig-zag morphology. Under polarizing light, collagen fibers give rise to a periodic pattern of light and dark bands which appeared and disappeared systematically as the crossed polarizers were rotated, or as the specimen was rotated about its longitudinal axis [33]. Small angle X-ray data presented by Gathercole and Keller (1975) supported this zig-zag morphology.

Rowe *et al.* (1985) presented the skewed register crimp model and concluded that their findings do not support the cylindrical symmetry model of fibril packing. Instead, collagen fibrils appear to aggregate side by side with flexibility in any direction in the register of wave patterns across the thickness of the fiber [46].

In the helix model, fibrils are helically organized around the fiber axis with a helical angle, θ, and a half pitch, h. In this model, the entire fiber is periodically collapsed in two dimensions, and the collapse direction forms an angle α relating to the long axis of the fiber. The collapse results in an undulated surface morphology. This configuration demonstrates that the peripheral fibrils are undulated helices with the central ones are normal helices [47].

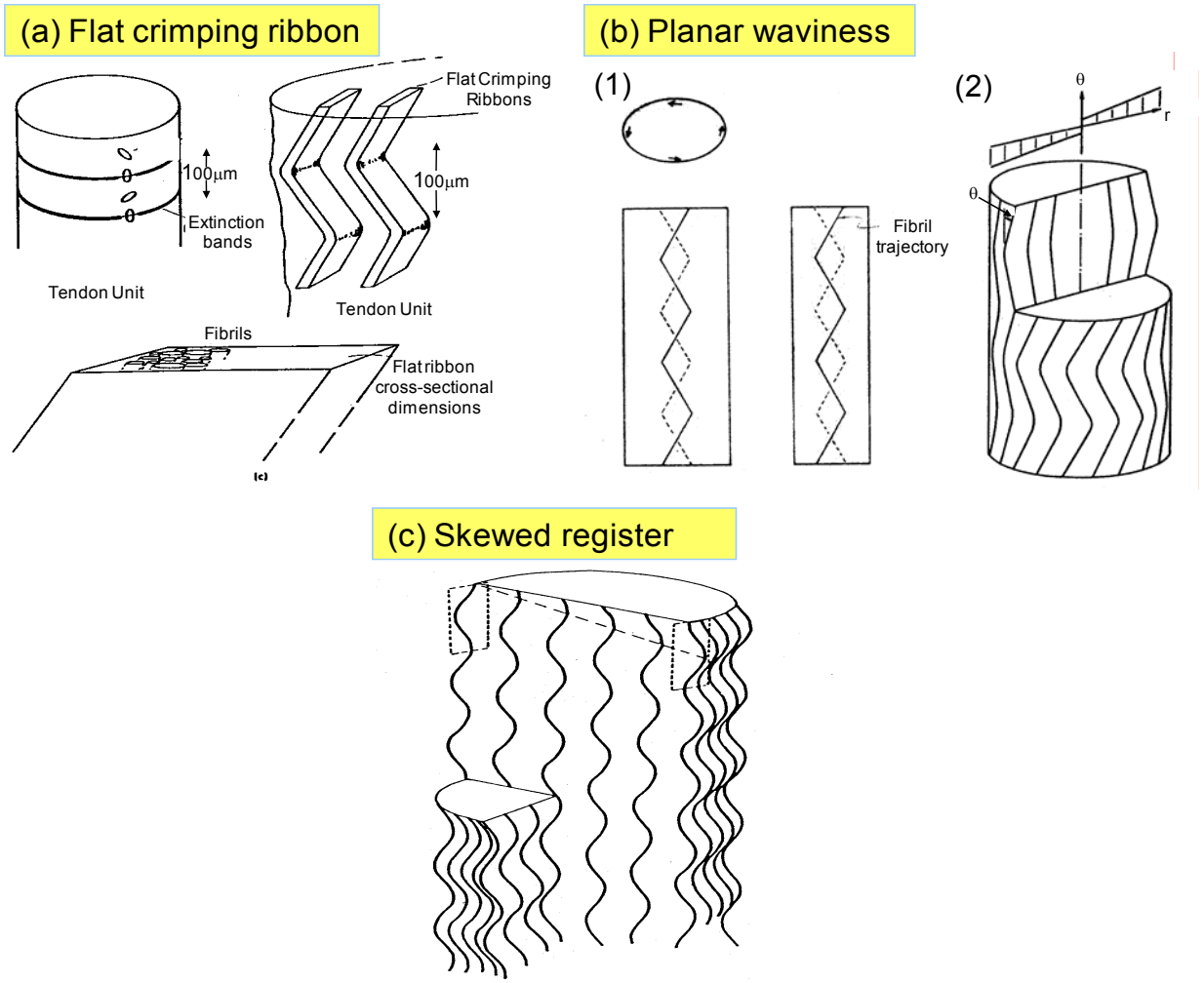

Figure 1-12. Proposed models for collagen crimp patterns. (a) Baer *et al*. proposed a flat crimping ribbon model. In this model, it is assumed that the fibrils have a ribbon like cross-section that results in the flattened cylinder cross-section of the tendon unit, i.e. fibers, which gives rise to horizontally elongated tendon cross-section. (With kind permission from Springer Science+Business Media: Structureal hierarchies and interactions in the tendon composite, vol 12, 1976, Baer, E., Hiltner, A., Friedman, B., Figure 5, Plenum Publishing Corporations) (b) Kastelic *et al*. proposed that fibrils follow a wavy or zig-zag crimped course and are packed cylindrically.(1. Reproduced from Kastelic et al. 1978) (2. Repinted from Journal of Biomechanics, vol 13, A Structural Mechanical Model for Tendon Crimping, Copyright 1980, with permission from Elsevier (Pregamon Press, Inc)) (c) *Rowe et al*. suggested the skewed register crimp model and state that their findings do not support the cylindrical symmetry model of fibril packing. (Reproduced from Rowe et al. 1985)

1.3.4 Structure-function relationship of collagenous tissues

Collagens are the major structural element of all connective tissues where they contribute to the stability of tissues and organs as well as maintain their structural integrity [26]. The ultimate strength of any material, natural or synthetic, depends on the substance in which it is composed. Thus, the ability of collagen to transmit load and maintain the structural integrity of tissue is a consequence of the aggregation of collagen fibrils, which have a well-defined tensile function, into collagen fibers.

It has been experimentally demonstrated that fibrils can have wide range of diameters. The ultimate tensile strength of fibrils is dictated by their diameter size. For example, fibrils with large diameters, which have a wider cross section, have a larger ultimate tensile strength as compared to smaller fibrils. As a result, when tissue undergoes high tensile loading, the collagen fibers will have a larger cross sectional area due to the large fibril diameters, allowing the tissue to maintain its integrity in the harsh loading environment [38].

Additionally, there appears to be a strong correlation between fiber orientation and the functional requirements of tissues. When an oriented stress needs to be withstood, proper fiber orientation becomes highly desirable because it provides an optimal match of structure and function. Thus, collagen fiber orientation significantly affects the mechanical properties of a tissue. For example, when a tissue is loaded in only one direction *in vivo*, the collagen fibers of that tissue will orient in one direction only, and the resulting mechanical properties will be anisotropic. However, if a tissue is loaded in all directions, the collagen fibers of that tissue will

be oriented in all directions, and the tissue will possess an isotropic mechanical behavior. Figure 1-13 is a schematic demonstrating these structure-function relationships. Consider three samples of tissue in an unloaded state. Sample 1 contains collagen fibers coursing in one direction only, which means this tissue has a preferred fiber direction (i.e. the x_1 direction) (Figure 1-13a). Sample 2 contains randomly oriented collagen fibers (Figure 1-13b). Sample 3 is an intermediate between sample 1 and sample 2 (Figure 1-13c). It does have fibers coursing in the x1 direction, but it also has some fibers oriented in random directions. Thus, sample 3 does not have a strong preferred direction, but it does have some consistent fiber orientation. Note that in the unloaded state, the collagen fibers are crimped (Figure 1-13a-c). Collagen crimp has a significant effect on the mechanical behavior of a tissue, and it is believed to be a significant factor in preventing damage if a tissue were loaded rapidly. When load is applied equally in the x_1 and x_2 directions, sample 1 displays an anisotropic mechanical response, meaning that the tissue response in the x_1 direction was very different compared to the tissue response in the x_2 direction. This type of behavior can be seen in heart valves, tendons, and ligaments. However, this was not the case in sample 2. Sample 2 exhibited an isotropic mechanical response where the mechanical response in the x_1 and x_2 directions were nearly identical, such is the case in the fetal membrane or cartilage. Note that these two situations are extremes. Sample 3 demonstrated a modest degree of mechanical anisotropy evidenced by the resulting stress-strain curve. Its tissue response in the x_1 direction is different than the tissue response in the x_2 direction. It is important to note that the x_2 response of sample 3 is stiffer than the x_2 response of sample 1, and this is because sample 3 has more fibers bearing stress in the x_2 direction. Sample 1 does contain fibers coursing in any direction other than the x_1 and thus, only bears stress in the x_1 direction. However, the x_1 response of sample 1 is stiffer than the x_1 response of sample 3.

This is because all fibers in sample 1 contribute to the stress in the x_1 direction. In sample 3, some of the stress is supported by the fibers in the other directions, reducing the amount of stress in the x_1 direction.

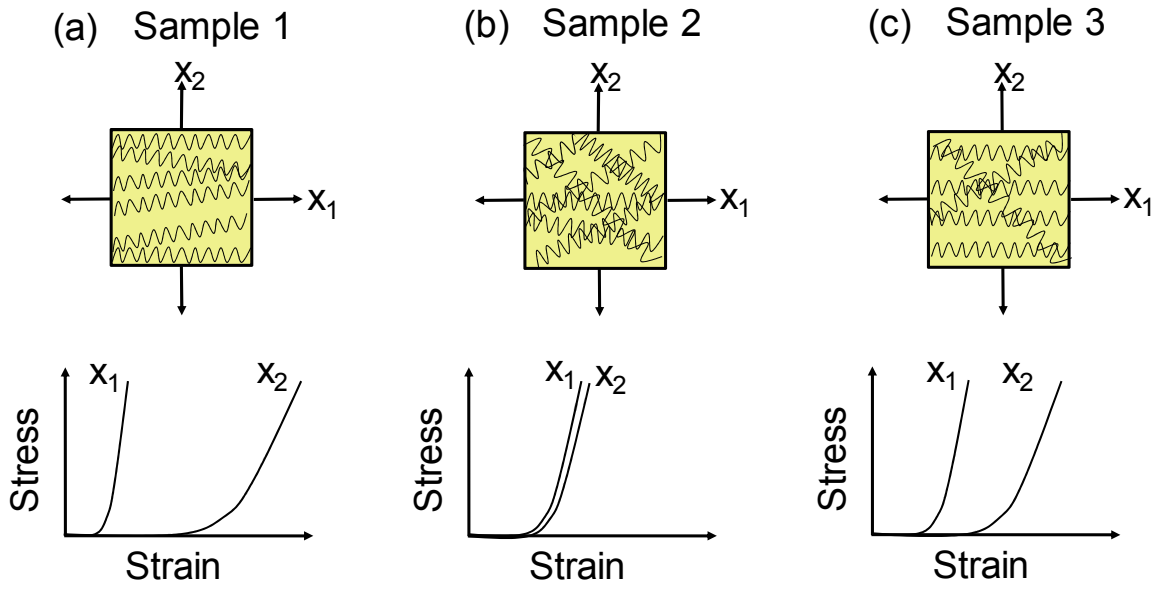

Figure 1-13. Schematic representation of the structure-function relationship between collagen orientation and mechanical behavior of a tissue. (a) Sample 1 contains highly oriented collagen fibers in the x_1 direction resulting in an anisotropic mechanical behavior. (b) Sample 2 contains randomly oriented collagen fibers, which results in an isotropic mechanical behavior. (c) Sample 3 is an intermediate between sample 1 and sample 2. Most of the collagen fibers are coursing in the x_1 direction, but some fibers are oriented in other directions; and thus the mechanical behavior is an intermediate between the completely aligned sample 1 and randomly oriented sample 2. For example, the x_1 mechanical response of sample 1 is stiffer than x_1 mechanical response of sample 3. This mechanical behavior can be explained by the underlying collagen microstructure. In sample 1, all load is born in the x_1 direction. However, while most of the load is born by the fibers in the x1 direction in sample 3, but some fibers do bear load in the x_2 direction, reducing the stress in the x_1 direction. Since some load is born in the x_2 direction of sample 3, its mechanical response is stiffer than the x_2 direction of sample 1, which bear minimal load in the x_2 direction. In contrast to sample 1 and sample 3, sample 2 is capable of bearing load equally in the x_1 and x_2 directions. Thus, the mechanical response in the x_1 direction is not as stiff as in the sample 1 or 3, and the mechanical response in the x_2 direction is stiffer than that of sample 1 and 3.

Fiber direction is indicative of the dominant tensile stresses that a tissue undergoes, because fiber reorientation is the most efficient and selective way to optimize strength without increasing weight and metabolic cost [38]. "The least material is used in the most strategic locations to carry the greatest loads with the least strain [38]."

1.3.5 Non-linearity of soft tissues

Collagenous soft tissues exhibit a characteristic non-linear stress-strain behavior. The nonlinear curve can be divided into four distinct regions, the "toe" region, the linear region, and two yield regions (Figure 1-15). Each region of the curve can be attributed to the behavior of the underlying microstructure of the tissue. First, consider a single undulated collagen fiber that is initially crimped and cannot bear load (Figure 1-14a,b) resulting in a slack region on the stress-strain curve. As increasing stress is applied, the fiber begins to straighten. Once a collagen fiber has become straightened, it will bear load, and the application of increased stress will cause the collagen fiber to elongate in a linear elastic manner, with slope K, also known as the elastic constant (Figure 1-14b).

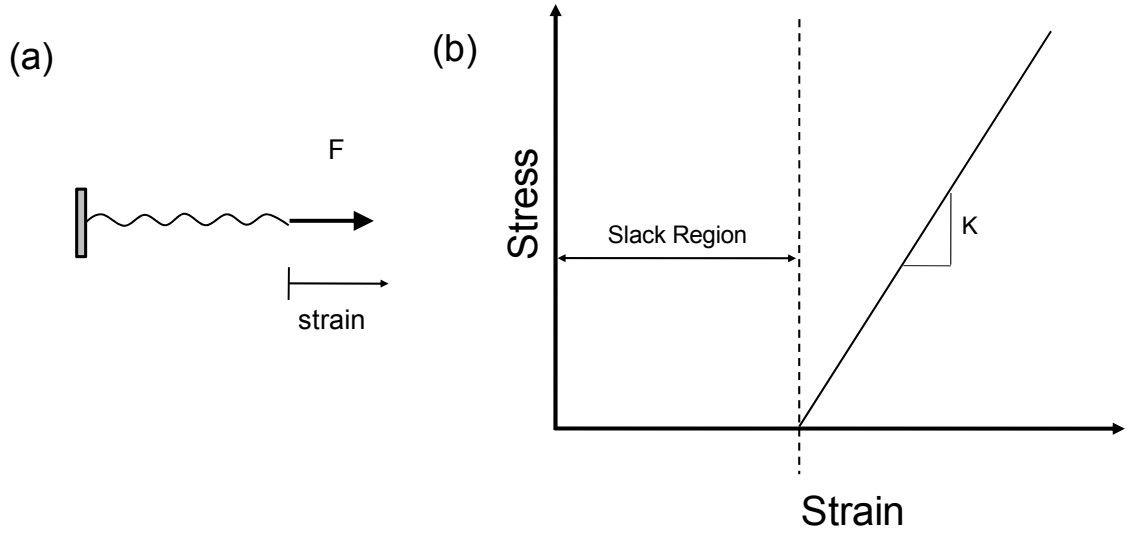

Figure 1-14. (a) Schematic representation of single undulated collagen fiber. (b) Traditional recruitment modeling assumes that a collagen fiber does not bear load until it is fully straightened.

Next consider a group of collagen fibers, with each fiber having a separate degree of undulation (Figure 1-15a). FM collagen fibers are recruited (straightened) with different amounts of stress due to their various original degrees of crimping (Figure 1-15 b, red line). One fiber may be fully recruited while others are still crimped or partially crimped. The sequential straightening of undulated fibrils due to increased stress results in the "toe" region of the stress-strain curve (Figure 1-15b, red line). Once all of the collagen fibers are straightened, the stress-strain curve becomes linear (Figure 1-15b, black line). The linear elastic region is the threshold of reversibility. With increased stress, the stress-strain curve transitions from the linear elastic regions to the yield regions evidence by a decreased modulus (Figure 1-15b, blue and green line). The first yield region can be attributed to permanent fiber elongation (Figure 1-15b, blue line), and the second yield region can be attributed to collagen fiber breakage (Figure 1-15b, green line). If only a small number of fibers were present, the various regions (i.e. "toe" region, highly linear region, yield regions) of the stress-strain curve would be discrete (Figure 1-15b, solid line). However, when a large population of fibers is present, the stress-strain curve is smooth and continuous (Figure 1-15b, dotted line).

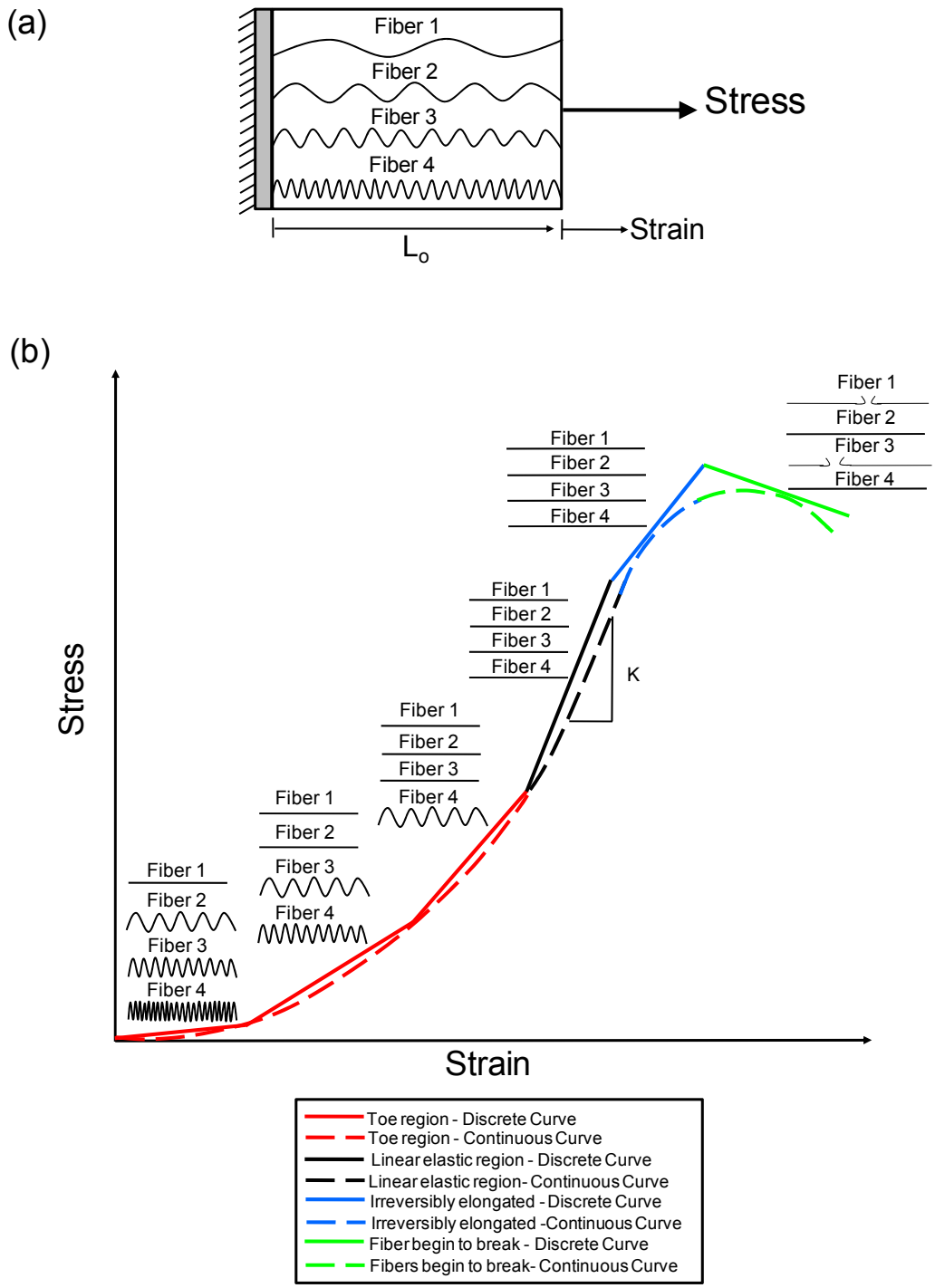

Figure 1-15. (a) Group of collagen fibers with various degrees of undulation. (b) Gradual recruitment of collagen fibers results in a non-linear stress strain relationship, which can be divided into four distinct regions, the toe region, the linear elastic region, and two yield regions. The toe region, represented by the red line, is a result of sequential straightening of the collagen fibers. Once all collagen fibers become straighten the stress-stretch curve transitions into a linear region, represented by the black line. Yield region 1 (blue line) can be attributed to permanent fiber elongation, whereas yield region 2 (green line) is a result of collagen fiber breakage.

1.3.6 MMP break down of collagen structure

Matrix metalloproteinases (MMPs) are a family of zinc metallo-enopeptidases that degrade extracellular matrix components and play important roles in many normal and pathological processes [48, 49]. Normal physiological roles include neutrite growth, cell migration, bone elongation, wound healing, angiogenesis, ovulation, sperm maturation, uterine involution, menstruation, enamel formation, antigenic processing and presentation, mammary gland development, hair follicle development, and embryo implantation [48]. Some pathological process involving MMPs include tumor growth and migration, fibrosis, arthritis, glaucoma, lupus, scleroderma, cirrhosis, multiple sclerosis, aortic aneurysm, and infertility [48]. For most of the MMPs, substrate specificity is not fully characterized. However, known substrates include most of the extracellular matrix components such as fibronectin, vitronectin, laminin, entactin, tenascin, aggrecan, myelin basic protein as well as collagens, types I-X and XIV [48]. MMPS are secreted from the cells and many have optimal enzymatic activity around neutral pH [49]. Endogenous inhibitors of metallo-proteinases (TIMPs), TIMPs 1-4, control MMPs [48]. Thus, the ratio of the MMP/TIMP for particular collagen thus determines whether the collagen is degraded.

MMPs are produced as zymogens, and contain a signal/prodomain, a catalytic domain with Zn^{2+} molecule in the active site, a hinge domain, and a pexin-like domain (Figure 1-16) [50]. The signal sequence and propeptide segment must be removed during activation. The propeptide domain contains a generally conserved sequence PRCGVP around a cysteine that chelates the active zinc site and is called the “cysteine switch.” The catalytic domain contains an active site that forms a long groove that divides the domain resulting in “pacman” appearance [48]. The propeptide domain lies in reverse orientation of this groove, and the cysteine switch is

positioned close to the active site, which allows for different substrate and inhibitor specificities. The catalytic domain of two MMPs, MMP-2 and MMP-9, includes a fibronectin-like domain which is thought to enhance substrate binding. All MMPs, with the exception of MMP-7 and MMP-9, contain a hemopexin domain, which is separated from the catalytic domain by a variable hinge region. The hemopexin domain is thought to provide the substrate specificity to the MMP and is involved in the activation and inhibition of the MMPs. Additionally, the hinge region provides specificity to the MMP either by direct binding or by setting the orientation of the hemopexin domain and the catalytic domain [48]. The three dimensional structure of the hemopexin domain can be thought of as a four-blade propeller and contains a calcium binding site situated in the folds [48]. Some MMP/substrate interactions appear to require calcium. Shedding of the hemopexin domain results in MMP activation, and the isolated hemopexin domain is thought to inhibit intact MMPs [48].

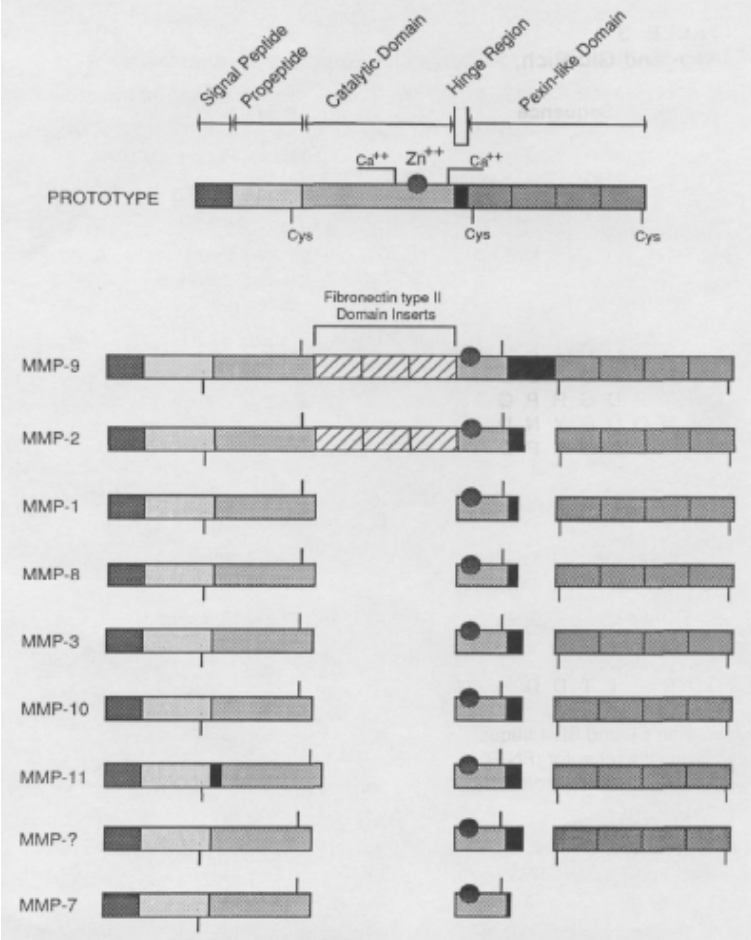

Figure 1-16. Structure Domains of Matrix Metalloprotinases. (Reprinted with permission from [50]. Copyright @ CRC Press, Inc, 1993.)

Cleavage of interstitial collagen by collagenases has been studied more extensively than any other MMP-catalyzed reaction [50]. Collagenases, namely MMP-1 and MMP-8, have the ability to degrade interstitial collagens (i.e. collagen types I, II, and III) [50]. The right handed triple helix structure, which is compose three left handed α-chains, of the interstitial collagens is resistant to cleavage by most proteinases except MMP collagenases. However, the active site of collagenolytic MMPs can only accommodate one α-chain. Thus, the triple helix structure must initially be unwound by a triple helicase mechanism in order to expose the scissile bonds, Gly_{775}-

Ile_{776} and Gly_{775}-Leu_{776} [50, 51]. This step requires the presence of a collagen-binding exosite as well as elements within active site. The hemopexin domain of MMP-1 and MMP-8 supports binding to collagen and is required for native collagen cleavage. After the triple helix has been unwound, cleavage of the three α-chains occurs sequentially at the scissile bonds producing ¾ and ¼ collagen fragments [51].

Another family of MMPs is known as the gelatinases or type IV collagenases, which include MMP-2 and MMP-9. These MMPs have the ability to readily digest gelatins as well as type IV collagen, which is typically found in basement membranes. MMP-2 and MMP-9 cleave various peptide bonds such as Gly-Val, Gly-Leu, Gly-Glu, Gly-Asn, and Gly-Ser in denatured collagen to yield small peptides, while experimentation on synthetic peptide substrates demonstrated that the preferred site of cleavage was the Gly-Ile bond [50]. Gelatinases also cleave types VII collagen, found in anchoring fibrils, cartilage type X collagen, and elastin in addition to gelatin and collagen types IV and V. Pepsin-solubalized type IV collagen was degraded by the gelatinases, but Makay *et al.* stated that full-length type IV collagen was resistant to proteolysis by both gelatinases, which caused speculation as to whether gelatinases actually function as true "type IV collagenases" *in vivo*. Nonetheless, the initial cleavage site of soluble type IV collagen by MMP-2 and MMP-9 is located roughly ¼ of the distance from the NH_2-terminus, and Hostikka and Tryggvason suggest that the Gly_{446}-Ile_{447} bond on the α1(IV) chain and Gly_{464}-Leu_{465} bond on the α2(IV) chain are the scissile bonds and are presumably located in the triple helical domain [50].

Locally produced TIMPS inhibit the activity of secreted fully competent MMPs and appear to block or impede MMP precursor activation. TIMPs appear in a wide variety of tisusess and fluids and to be expressed by different normal and transformed cell types form skin,

mucosal membranes, synovial tissues, cartilage, dental pulp and ovaries [50]. Currently, there are four TIMPs identified, TIMPS1-4, and while TIMPS inhibit all MMPs tested so far, some TIMPs have a greater specificity for some MMPs than others [48, 52]. TIMPs form classic noncovalent bimolecular complexes with the active forms of MMPs as well as with their latent forms under certain circumstancesl [50]. The mechanisms of TIMP inhibition of MMPs has been clarified from the crystal structures of TIMP-MMP complexes [52]. TIMPs appear to have an overall "wedge-like" shape. The four residues Cys1-Thr-Cys-Val4 at the N-terminal and the Glu67-Ser-Val-Cys70 residues, which are found in TIMP-1, are linked by a disulfide and from a contiguous ridge that slots into the active site of the MMPs [52]. The catalytic zinc atom is bidentately chelated by the N-terminal amino group and the carbonyl group of Cys1 causing expulsion of thee water molecule bound to the zinc atom [52]. Complex formation does not appear to involve cleavage of the TIMPs, and the full functional TIMPs can be recovered from the complex [50]). The first 24 N-terminal residues are highly conserved between TIMP-1 and TIMP-2 and across species, including the VIRAK sequence noted by Woessner [50]. Carbamylation of the N-terminal amino group or an addition of an extra Ala at the N-terminus inactivates TIMPS so that they can longer inhibit MMP activity [52], and these alterations weaken the metal ion chelating ability of TIMPs [52].

It has been demonstrated that TIMP-1 forms complexes with MMP-1, but not proMMP-1 [50]. TIMP-1 also forms complexes with the zymogen form of MMP-9 [50]. TIMP-2 forms a complex with zymogen MMP-2 [50], and is a specific inhibitor of MMP-2. TIMP-2 is 2 to 10 fold more effective than TIMP-1 in inhibiting gelatins, but TIMP-1 appears to inhibit MMP-1 more effectively [50].

1.4 PHYSIOLOGICAL FAILURE OF THE FETAL MEMBRANE

Tissue failure, as occurs when the FM ruptures, is a unique event in normal human physiology, whereas other tissue failures (e.g. tendon/ligament failures, bone fracture, skin tears, vascular aneurysms) are all pathological processes. FM rupture is likely a direct consequence of a programmed, biochemically mediated weakening process [1, 14] that may work in coordination with physical forces. However, in order to understand FM failure, the relationship between physical rupture and programmed, biochemically mediated FM weakening must be established. These two mechanisms are discussed in detail in the following.

1.4.1 Biochemically mediated processes lead to programmed weakening of the FM

Traditionally, membrane rupture was thought to be a consequence of physical stress alone, particularly during labor. However, in 10% of term and 40% of preterm deliveries, membrane rupture precedes contractions [14]. It has thus become clear that rupture of the FM, term or preterm, is not solely the result of the stretch and shear forces of uterine contractions, but in significant part the consequence of a programmed, biochemically mediated, weakening process [1, 14]. Animal data clearly documented gestational changes in the FM consistent with weakening [14, 53-55]. A homogeneous remodeling process over the entire FM with degradation of collagen Type I as a major component was seen in the rat amnion at end gestation [56]. Attempts to document similar gestational changes in human FM were initially unsuccessful, however [57]. Using a meticulous approach, the Bell group identified a region of high morphological change at the rupture site in term vaginal deliveries [58]. The same group later identified a similar region overlaying the cervix in patients that delivered by cesarean

section without labor [59]. This area of altered morphology was characterized by increased matrix metalloproteinase (MMP) activity [60]. Apoptosis, particularly in the chorion trophoblast layer, was also reported in this para-cervical region of human FM by them and thereafter by several other groups [59-63].

Three groups have now confirmed that a zone of altered morphology exists in the region overlying the cervix [58, 61, 63]. El Khwad *et al.*, however, was the first to demonstrate that these biochemical and histological changes are associated with physical weakening of the FM [61]. It was demonstrated that a discrete zone of weakness ("weak zone") is present in term, prelabor FM in the region overlying the cervix. In addition to decreased rupture strength (1/3 of that in other areas of the FM), the "weak zone" showed deceased work to rupture, stiffness, and ductility (displacement at the time of rupture) (Table 1-2). Concomitant with these differences in biophysical properties, it was demonstrated that the "weak zone" FM exhibited biochemical characteristics consistent with tissue remodeling and apoptosis [61]. The cervical zone, or "weak zone," exhibited increased MMP-9 protein, which showed an inverse linear relationship with FM strength [61]. Also, a decrease in TIMP-3 was present in this zone but was prominent in the remaining areas of the FM and increase in parallel with FM strength [61]. The cervical zone demonstrated an increase in PARP cleavage, indicative of increased apoptosis, compared to remaining regions. PARP cleavage illustrated an inverse linear relationship with strength [61].

Table 1-2. Physical properties of the FM in the cervical zone and the remaining regions. (a) The mean strength of the cervical zone was less than the mean strength of the remaining areas. Also, work to rupture, stiffness, and ductility were decreased in the cervical zone.

Physical Parameters	Cervical Area	Remaining Area
Strength	4.98 ± 1.38 N	9.07 ± 2.61 N
Work to Rupture	0.012 ± 0.006 J	0.025 ± 0.011 J
Stiffness	9.14 ± 2.51 N/cm	14.47 ± 3.38 N/cm
Ductility	0.56 ± 0.097 cm	0.67 ± 0.101 cm

In addition to MMP-9 other groups have speculated that MMP-2 may be implicated in the mechanisms of membrane rupture. However, the exact changes in MMP-2 expression and activity during labor are not clear. Some believe that MMP-2 is constituantly produced in the FM [64], while others have demonstrated that it is increased in the FM toward end gestation [65]. In addition, Yonemoto *et. al* claimed that MMP-2 was increased in the amnion layer with labor and no changes in the chorion [66]. Furthermore, Goldman *et. al* demonstrated that there is an increase in MMP-2 following uterine contractions in the decuida, with no change in the chorion layer [67].

Finally, it was demonstrated that the "weak zone" contained the same histological changes noted in areas of high morphological change by Malak *et. al* [58, 61]. In another report, El Khwad et. al demonstrated that FMs delivered vaginally also had a "weak zone" with identical biochemical markers as the Cesarean FM [62]. Furthermore, in FMs with spontaneous rupture, the "weak zone" was bisected by the rupture tear line [62].

The above data is consistent with a programmed biochemical process characterized by extracellular matrix (ECM) remodeling and apoptosis acting focally upon the FM region

overlying the cervix to create the "weak zone". Further, the "weak zone" contains the rupture initiation site. In addition, Kumar et. al also demonstrated that *in vitro* incubation of FM with either TNF or IL-1b can transform "non-weak" FM into weak membranes with the same biochemical markers of ECM remodeling and apoptosis seen in the naturally occurring "weak zone" [68].

1.4.2 Biomechanical studies of FM failure behavior

Many investigators performed *in vitro* biomechanical studies in an effort to understand FM failure [1, 12, 15, 61, 69-78]. Three types of testing techniques were utilized (Table 1-3):

(1) Tensile testing, in which the membrane is placed between two grips and is gradually pulled apart while the resulting forces and strains are monitored [15, 69-72].

(2) Burst testing, in which a section of membrane is clamped in a circular ring and increasing pressure is applied, either via air or fluid, to membrane until failure occurs while the height of the membrane is monitored [73-78].

(3) Puncture testing, in which a spherically tipped metal probe displaces the central portion of a membrane, which is clamped in a ring, perpendicular to the plane of its surface [1], while the resultant force is measured [1, 12, 61].

Note that in order to efficiently compare values from each mode of testing, each failure value was converted to a membrane tension. For tensile testing, the reported force was converted to membrane tension by dividing the force by the width of the specimen (T=Force/width). For burst testing, the reported pressures were converted to membrane tension using the Law of LaPlace. Specifically, the Law of LaPlace states the relationship between pressure, surface tension, and curvature of the surface of the FM and can be expressed as:

$$T = \frac{Pa}{2} \tag{1-1}$$

where T is the mean membrane tension, P is internal pressure, and a is the estimated radius of the FM [36]. The radius, a, was estimated from the radius of the fixture diameter. If only force was provided for the burst and puncture test, the force was first converted to pressure by dividing the force by the surface area of a hemisphere (P = Force/Surface Area). After conversion to pressure, equation (1-1) above, was used to determine the membrane tension. It is important to note, that these methods were only used to provide an estimate of the membrane tensions.

Table 1-3. Summary of mechanical tests performed on the intact FM. This table provides the values at which the membrane ruptures along with relevant details about the testing techniques. Note that the fixture diameter is the diameter of the circular opening in the center specimen holder in both the burst and puncture devices. This opening in the specimen holder allows the air/water of the burst device and the probe of the puncture device to impinge on the secured FM specimen. The probe diameter is the diameter of the metal probe/plunger in the puncture tests.

Study	Failure Value	Details
Uniaxial Test		
1 [71, 79]	0.95 N (237.7 N/m)	Specimen Dimensions: 4mmx15mm
Burst (Inflation) Test		
2 [79, 80]	393 mmHg (261.98 N/m)	FD: 20 mm
3 [81]	15 N(152.06 N/m)	FD: 15.7 mm
4 [73]	0.205kg/cm (201.105 N/m)	FD: 54 mm
5 [76]	60 mmHg (152.39 N/m)	FD: 76.2 mm
6 [77]	40 mmHg (101.59 N/m)	FD: 76.2 mm
7 [78]	100 mmHg(253.98 N/m)	FD: 76.2 mm
Puncture Test		
10 [82]	11.34 N (150.40 N/m)	FD: 15.88 mm; PD: 12 mm
11 [61]	9.07±2.61N (144.35 N/m)	FD: 25 mm; PD: 10 mm
12 [12]	4.15±1.27N (206.40 N/m)	FD: 20 mm; PD: 3.2 mm
13 [83]	9.71±2.42N (154.54 N/m)	FD:25 mm; PD: 10 mm

FD = Fixture Diameter
PD = Probe Diameter

In each mode of testing various mechanical parameters (i.e. stiffness and rupture strength of the membranes) were determined [1, 71, 79]. Of these methodologies, tensile testing does not provide a physiological testing state as the stresses applied are uniaxial, whereas the FM is physiologically loaded under a complex biaxial state. Tensile testing is used because standard stress-strain calculations are simple to apply. Burst testing better mimics the physiologic loading state. However, it is logistically difficult and requires relatively large pieces of membrane. In puncture tests, the plunger impinges on the FM resulting in an approximately planar state of tension applied to the FM and can be carried out quickly on relatively small pieces of membrane**.** The resultant force measurement is dependent on the size of the metal probe and tissue holder. However, Schober *et al*. demonstrated that data obtained by puncture testing can be directly related to that which would be obtained using the more physiological burst testing methodology [1, 53, 81, 82]. They reported membrane strength properties in terms of the ratio of surface areas of the test sample and the probe, using a fixed specimen diameter and probes of various sizes [1, 53, 81, 82]. Schober *et al.* concluded that mechanical properties derived from the puncture testing method were equivalent to those obtained with burst testing if the ratio of tissue fragment to probe surface area was extrapolated to one [1, 53, 81, 82]. As a result, several recent biomechanical investigations of the FM were conducted using this method [61, 62] [1, 12, 61].

There are major differences in conclusions based on aforementioned mechanical testing methodologies by different investigators due to various reasons. First, different investigators were lead to different conclusions because of the use of different testing methodologies (Table 1-3). Also, the heterogeneity of the tissue biomechanical properties of the FM surface resulted in different conclusions. Investigators were not aware of the existence of a "weak zone" prior to reports by El Khwad *et al*. [61]. In addition, there was confusion as to which layer of the FM

was stronger (amnion or choriodecidua) and which component ruptures first. Recent studies by Arikat *et al*. included video-recording of the rupture process and demonstrated that the choriodecidua component of the intact FM did rupture first [83].

1.4.3 Failure mechanics: a new territory in normal physiology

Tissue failure is not a normal, physiological event. Bone breakage, skin tears, bowel ruptures are all pathological events which occur as the result of huge force or massive tissue breakdown. The ovarian follicle and some embryological structures do demonstrate tissue failure in the course of normal events, but these are relatively thin and lack the mutilaminar structure of FM. Because tissue failure typically occurs as a result of a pathological process and not normal function, the biomechanics of soft tissue failure is generally poorly understood.

Tissue failure mechanics modeling is a relatively new area without much development. Constitutive models are used to establish a relationship between physical quantities specific to a material, and the constitutive model can be used to approximate the response of the material to external forces. There are two types of constitutive models, phenomenological models and structural constitutive models. Phenomenological models are used to describe the macroscopic nature of materials. Mathematical equations are fit to experimental data in the phenomenological approach, and this approach is successful in capturing the nonlinear behavior of soft tissues. However, phenomenological modeling does not describe the microstructural basis for the constitutive behavior of a material. Structural constitutive models, however, can elucidate the correlation between the underlying microstructure of a material and the mechanical behavior. Although many constitutive models have been proposed for the description of the mechanics of

various collagenous tissues, only a few models have been formulated to illustrate failure processes.

Liao and Belkoff developed a structural constitutive model for ligament failure [84]. Their model assumed sequential uncrimping and stretching of collagen fibers is responsible for the mechanical response of the ligament and fiber failure occurred sequentially in a brittle, strain-limited manner. In order to incorporate a failure mechanism into the model, the authors assumed that when any straightened fiber was deformed beyond a limit strain, brittle failure of the fiber occurred. Additionally, they assumed that all fibers have the same elastic fiber modulus and limit strain (a), which constrained the fibers to fail in the same sequence in which they were recruited.

Natali *et al.* developed an anisotropic elasto-damage constitutive model for tendons [85]. Their model assumes that damage phenomena are microstructural alterations which result in decreased mechanical strength of a material when external loads are applied. They further assume that damage occurs when stress or strain state exceed the elastic limit of a tissue. Their constitutive model incorporates a damage function. Natali *et al*. also developed a visco-hyperelastic model used to analyze the time-dependent mechanical response because their elasto-damage model only accounted for a decrease in stiffness and strength that can develop under significant loading and degenerative conditions [86]. A specific damage criterion was formulated to evaluate the influence of strain rate on damage in periodontal ligament.

De Vita and Slaughter developed a constitutive law for failure behavior in collateral ligaments [87]. Their model assumed that collagen fibers are initially crimped and are unable to sustain load in this slack configuration. However, after the fiber become straightened and before failure, each collagen fiber exhibits a linear elastic behavior. Additionally, the authors assume

that after the fiber lose their waviness, the fiber fail at different stretches. While their assumptions appear reasonable, when the model was fit to data, the model predicted that fiber failure began in the toe region while some fibers were still in their crimped state. Ligaments' physiological operating ranges are in the "toe" region of the stress-strain curves [88]. Thus, failure should not occur during physiological loading, and their model predicted non-physiological ligament behavior [88].

Layton and Sastry developed a constitutive model for peripheral nerve of diabetic and non-diabetic rats that incorporated fibril load sharing [89]. They investigate two extrema in load sharing: (1) equal load sharing, where unbroken fibers in a bundle share load equally, and (2) immediate neighbor local load sharing, where only the unbroken fibers adjacent to broken fibers in a bundle are subjected to overload.

Ionescu *et al.* presented an anisotropic constitutive model for an isotropic matrix reinforced by a single fiber family that incorporated strain-based failure criteria [90]. They then implemented their model into existing computational solid mechanics software based on the material point method, which is a quasi-meshless particle method for simulations in computation mechanics.

Every model presented above is only applicable to parallel-fibered collagenous tissues. These models would not be applicable to the FM because the FM contains a complex heterogeneous fiber network.

Volokh developed a bi-layer fiber-matrix model with softening to predict arterial failure [91]. Volokh used a softening hyperelasticity approach towards failure modeling as opposed to local failure criteria and damage mechanics, which were previously presented. While this novel approach captures the mechanical behavior of the intact arterial wall, this model is over

simplified for the fetal membrane. The arterial wall only contains two families of collagen, which is aligned concentrically in the media and longitudinally in the advantia, whereas the fetal membrane has randomly oriented collagen fibers.

Additionally, Slaughter and Sacks developed a constitutive model for fatigue damage in chemically treated soft tissue [92]. However, the FM does not fail as a result of fatigue, and this type of model is not applicable. Few others have attempted failure modeling for soft tissues [93-96].

In addition to inappropriate or inaccurate failure models, most of the previous FM biomechanical studies on failure, while providing important insight, remain limited in that they utilize non-physiologic uniaxial loading techniques. Other approaches have utilized simple interpretations of puncture-mode failure tests, which while under biaxial loading provide only limited understanding of the FM ECM failure process [1, 12, 61, 83, 97]. These focused entirely upon the force required to acutely break the FM (rupture force). However, it remains unclear how failure occurs in the FM, which is dictated by the underlying collagen architecture as well as the biochemical factors that modulate its failure. Arikat *et al*. recently reported video-documentation of the sequence of events which occur during *in vitro* FM rupture [83]. Using a puncture testing apparatus in which a FM fragment was held in a ring while a plunger applied distending force perpendicular to the plane of the FM fragment, the following rupture sequence was reported: (1) the amnion and the choriodecidua stretched together under load; (2) the amnion separated from choriodecidua; (3) the choriodecidua ruptured; (4) the amnion plastically distended further, and (5) the amnion ruptured[83]. These events can be clarified by the underlying microstructural responses. During puncture studies, the amnion and the choriodecidua are initially adherent and relaxed with collagen fibers in the FM presumably

crimped (Figure 1-17). With increasing stretch forces in the testing equipment, the amnion and the choriodecidua both distend, and the collagen fibers reorient along the direction of applied stretch. The individual fibers begin to uncrimp (Figure 1-17). As the plunger continues to stretch the tissue, the fibers of the amnion layer continue to straighten and eventually become taught (Figure 1-17). During this phase, the choriodecidua and amnion separate from each other, and a linear fracture appears in the choriodecidua, while the amnion layer initially remains intact[83]. The strongest FM component, the amnion, finally ruptures after undergoing further non-elastic deformation [12, 15]. There are two possible scenarios leading up to this failure of the amnion (Figure 1-17). In scenario 1, all collagen fibers are recruited and straightened rapidly, resulting in a very small "toe" region. All collagen fibers will then fail soon after. In scenario 2, the collagen fibers are recruited more gradually contributing to a larger "toe" region. Then, with increased stretch, the collagen fibers begin to fail at different amounts of stretch, resulting in a gradual failure of the collagen fibers. The mode of failure is thus likely dependent upon the behavior of the tissue under tensions well below that required to rupture the FM.

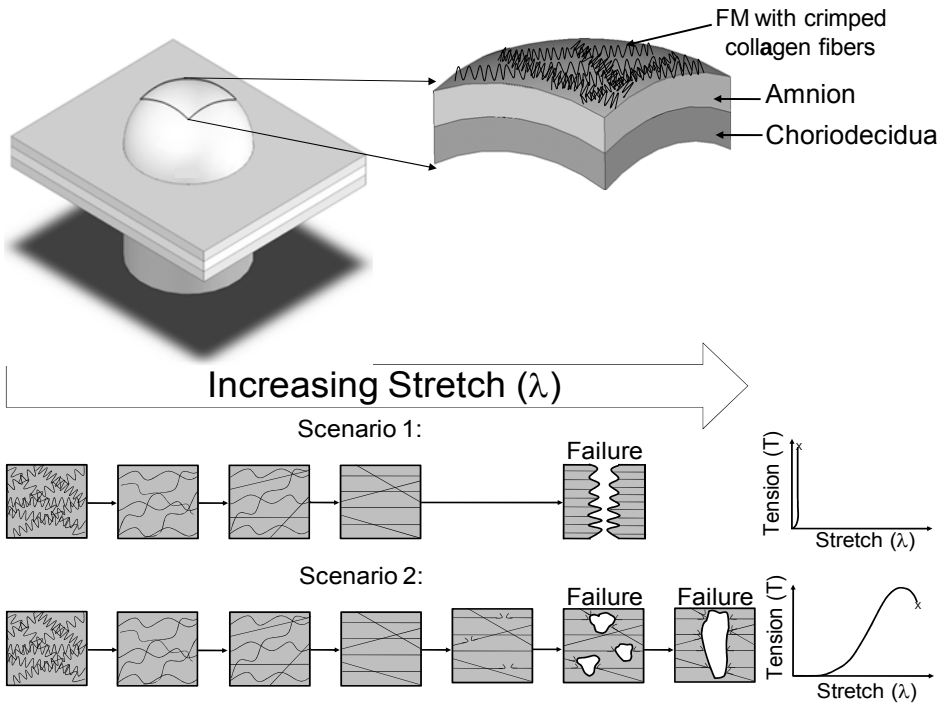

Figure 1-17. Idealization of collagen fiber behavior during puncture studies and its associated tension vs. stretch curves. The amnion layer and the choriodecidua layer are firmly attached and stretched with the plunger during puncture studies. The collagen behavior of the FM up to failure can be idealized by two possible scenarios. In scenario 1, collagen fibers are straightened rapidly resulting in a minimal "toe" region and all fibers fail at approximately the same stretch after becoming fully straightened. In scenario 2, due to the various degrees of collagen crimp, there is a larger toe region. After all the collagen fibers become straight, some collagen fibers begin to fail, while others remain intact. As stretch continues to increase, small point defects begin to occur and eventually lead to complete failure. Thus, failure is more gradual as compared to scenario 1.

The importance of biomechanics in FM failure is also reflected in the relation between biomechanical and biochemical processes. It has been demonstrated that proteolytic enzymes play a role in membrane rupture [1], and perhaps work synergistically with mechanical forces to induce tissue failure. This speculation is supported by the known interplay between mechanical deformation and collagen degradation in soft collagenous tissues [98] [99, 100]. For example, Lee *et al.* demonstrated that tensile loading accelerates the proteolysis of bovine pericardium subjected to collagenase [98]. Also, another study demonstrated that the degradation rate of collagen increased with stretch [100].

These observations could be caused by two possible mechanisms [100]. Collagen fibers are composed of three polypeptide chains (tropocollagens) intertwined to form a triple helix or collagen molecule. The stretching of the collagen molecule may result in the opening of new sites making it more susceptible to enzymatic degradation [100]. If only certain sites were exposed during stretch, then only these collagen fibers would be more susceptible to failure and thus, not all the collagen fibers will fail at once. Scenario 1 may be explained by this phenomenon (Figure 1-17). Another possible mechanism for the increased degradation rate could be that the enzymatic breakdown of a given collagen molecule caused the remaining stress in the tissue to be transferred to a neighboring molecule, which may then rupture. If this is a widespread event, rapid break down of the collagen fibers could ultimately result in a catastrophic failure of the tissue [100]. Scenario 2 may be explained by this mechanism (Figure 1-17). While the exact mechanism is unknown, it may be that mechanical stress may facilitate weakening of the collagen fibers by attacking the molecules that organize collagen Type 1, such as decorin, biglycan, the fibulin family. Irrespective of the exact mechanisms, we speculate that enzymatic degradation of the FM collagen may be accentuated by mechanical stress.

1.4.4 Understanding sub-failure mechanical behavior is a necessary prerequisite for understanding FM failure

To date, most *in vitro* mechanical studies have focused on the failure behavior of the FM, whereas minimal data exists for the sub-failure mechanical properties. In order to fully understand FM failure, it is first necessary to characterize the sub-failure response of the FM. After establishing the sub-failure response of the FM, one can extrapolate this response to failure conditions. In particular, by taking this approach, the complete stress-strain response of the FM

from the unloaded, stress-free state until failure will be established. With this information, a sub-failure structural model for "non-weak" FM (tissue from regions distal to the paracervical weak zone [61, 62]) can be developed. This model can then be extrapolated to rupture conditions and used to investigate the physical basis of the FM "weak zone" [101]. One approach to modeling tissue mechanics are structure (i.e. stress-strain) models that can elucidate the correlation between the strength enhancing biological components of the FM, such as collagen, and mechanical behavior. Thus, by investigating the structure-strength relationship of "non-weak" FM, one can then begin to understand how the structure-strength relationship of the FM is altered in the "weak zone" resulting in FM rupture. In addition to modeling, the direct effects of stretch on FM failure need to be investigated and can only be done under sub-failure conditions [101].

Our understanding of FM failure biomechanics would be greatly enhanced by utilizing physiologic biaxial testing approaches to characterize the sub-failure state and delineate the effects of ECM degradation due to a programmed, biochemically mediated, weakening process. In contrast, simple interpretations of puncture-mode failure tests have been implemented to investigate FM failure, but this type of approach can only provide limited information about FM failure (Figure 1-18). While apparently simple, this test actually induces a complex stress state. A stress "amplification" is induced at the tip of the plunger [102]. Specifically, the stress in the FM is greatest at the tip of the plunger (Figure 1-18b), and with increasing values of ϕ, which is the angle between the tip of the plunger and an arbitrary point along the membrane, the stress is reduced, until the stress field becomes homogenous. The angle in which the FM loses contact with the plunger is designated by ϕ_c. Calculations using an average stress would cause an underestimation of the failure stresses.

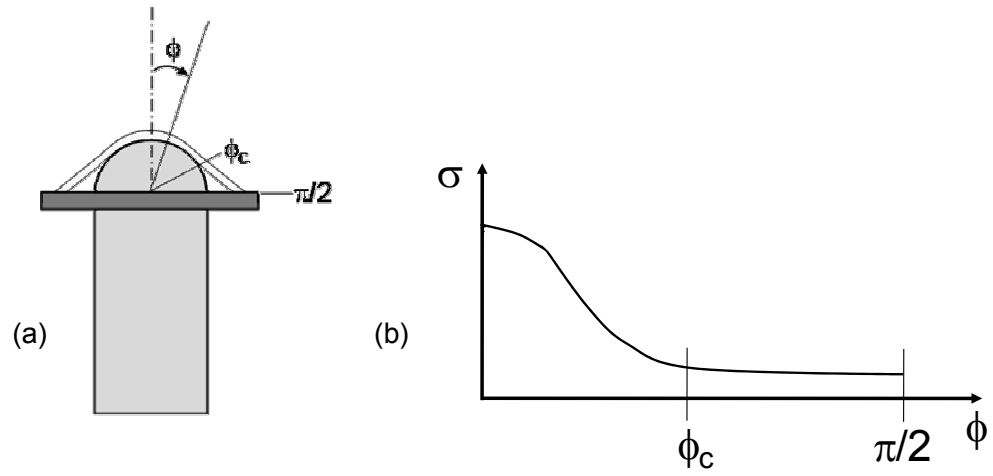

Figure 1-18. (a) Schematic of puncture device and the FM being deformed. ϕ is the angle between the tip of the plunger and an arbitrary point along the membrane and is defined from 0 to $\pi/2$. At the tip of the plunger, ϕ is 0. ϕ_c is the angle in which the FM loses contact with the plunger. (b) Due to the geometry of the plunger, the stress field over the surface of the FM during puncture studies is heterogeneous, resulting in a complex data analysis. At 0, which is the tip of the plunger, the stress is the greatest. With increasing ϕ, the stress decreases over the surface of the FM and eventually becomes homogenous.

Thus, current failure testing techniques provide limited information on FM tissue mechanics. To better our understanding of the physiologic behavior of the FM, mechanical testing techniques need to be more amenable to the determination of FM sub-failure structural mechanical properties. Planar biaxial mechanical testing is one approach for studying sub-failure mechanical properties. In particular, the central target region of the test specimen for planar biaxial mechanical testing contains uniform stress and strain fields permitting data analysis to be simply performed [103]. Also, the target test region is small and located away from the outer edges of the test specimen to avoid the effects of specimen grips or tethers [103].

1.5 MOTIVATION AND SPECIFIC AIMS OF PRESENT STUDY

Premature birth is a major public problem accounting for over 13,000 deaths and 30,000 surviving infants with life-long morbidity yearly [17-19]. Preterm prolonged rupture of the fetal membranes (FM) occurs prior to the onset of the contractions of labor and is the initiating event leading to preterm birth in about 40% of premature infants [23]. Although significant progress has been made recently [1], the physiological mechanisms which cause membranes to rupture, term or preterm, are not completely understood. In the past, weakening and rupture of the FM were attributed to the mechanical stresses of the contractions of labor [14]. This is not consistent with the 10% of term and 40% of preterm births in which rupture precedes contractions. It is now established that animal and human FM undergo extracellular matrix (ECM) remodeling and apoptosis in late gestation [56, 62, 104], and these biochemical changes are largely limited to the region overlying the cervix in human FM [58, 61, 63]. Moore et. al demonstrated that region overlaying the cervix is physically weaker than the remaining FM [61]. Further, the "weak zone" is present prior to labor [61] in patients who underwent repeat Cesarean section, and the FM rupture tear line passes through the "weak zone" in patients with spontaneous FM rupture [62]. Taken as a whole, the FM "weak zone" is likely where FM rupture initiates.

Tissue failure, as occurs when the FM ruptures, is a unique event in normal human physiology, whereas other tissue failures (e.g. bone fracture, skin tears, vascular aneurysms) are all pathological processes. Clearly, a full understanding of the FM failure process requires a complete characterization of the structural and mechanical behavior of the FM at near/full term under sub-failure (forces well below that which cause rupture) and failure conditions. Most of the previous FM biomechanical studies, while providing important insight, remain limited in that they utilize non-physiologic uniaxial loading techniques. Other approaches have utilized simple

interpretations of puncture-mode failure tests, while under biaxial loading provides only a limited understanding of the FM ECM failure process [1, 12, 61, 83, 97]. Our understanding of FM failure biomechanics would be greatly enhanced by utilizing physiologic biaxial testing approaches to characterize the sub-failure state of non-weak FM, which will be used to lay the basis for understanding how the FM transitions to failure. Additionally, the failure process of the non-weak FM must also be investigated in order to establish how the normal, non-weak structure-function relationship of the FM is altered in the "weak zone," which has unique mechanical properties that facilitates tissue failure. Taking this integrated approach will help determine how the FM undergoes mechanical failure as well as elucidating the underlying micro-mechanical mechanisms that modulates its failure. It is hypothesized that the structure-function relationship of the FM is highly optimized for its unique function to fail at a prescribed time; a rare event in normal human physiology. The results obtained will further our understanding of this unique physiological event and thereby provide insight into how we may anticipate, and, when appropriate, intervene to prevent preterm FM rupture. Based on the aforementioned rational, the aims of the present study were as follows with a depiction of the aims in a flow chart in Figure 1-19:

Specific Aim 1: Characterize the sub-failure structure-strength behavior of the FM under physiological loading conditions. As a necessary first step, the baseline structure-strength relation of "non-weak zone" FM tissue will be established. This will improve the understanding of FM tissue biomechanics via the following sub-aims:

Aim 1.1: Characterize the mechanical properties of "non-weak" FM under biaxial loading. Planar biaxial testing techniques allow for physiological loading of the FM and provide all relevant deformation necessary for constitutive modeling [103]. The endpoint of this aim was

to quantify the sub-failure FM mechanical properties, which will lay the basis for the understanding of how the FM transitions to failure.

Aim 1.2: Assess collagen fiber architecture of both the intact and separated FM layers (amnion and choriodecidua) in the "non-weak" FM. Understanding the gross collagen fiber architecture of the FM ECM can contribute to a better understanding and predictability of the mechanical properties of the FM. Small angle light scattering (SALS) was used to nondestructively quantify collagen fiber architecture alignment of the intact and separated FM layers [105]. The endpoints of this aim will be to quantify the collagen fiber structure, such as the preferred fiber directions(s) and the degree of fiber alignment.

Aim 1.3: Determine the *in vivo* stretch of the FM. In order to fully characterize the mechanical properties of the FM, the baseline, intrauterine stretch of the FM prior to labor must be determined. The scientific endpoint of this aim was to establish the ratio of the surface area of the FM *in vivo*, which will be determined from MRI images, to the surface area after delivery, allowing one to determine the *in vivo* stretch of the FM.

Specific Aim 2: Implement a structural constitutive model to investigate the sub-failure responses of FM. Utilization of a structural constitutive model will allow for the establishment of the baseline structure-strength mechanical behavior of the "non-weak" FM by elucidating the correlation between the structural components and the resulting mechanical behavior of the FM. The model will be based on fiber-level sub-failure events using a stochastic approach and includes a statistical distribution of the fiber recruitment. The scientific endpoint of this aim was to build on the results of specific aim 1, to characterize the response of the FM under physiological loading, and to optimize key parameters of the structural constitutive model that can be related to the underlying microstructure of the FM.

Specific Aim 3: Characterize structural/strength sequelae during failure of the FM in the "non-weak" regions. Building on the results of the first and second aims, the micro-structural events that occur during loading and failure of the "non-weak" FM will be investigated. This will be achieved through the use of a novel device that will be integrated into our SALS system that can perform burst failure tests while simultaneously quantifying the collagen fiber architecture, which will help elucidate how the FM transitions to failure. The scientific endpoint of this aim was to quantify collagen fiber structure, such as the preferred fiber directions(s) and the degree of fiber alignment at various loading levels as well as investigating the development of failure in the FM.

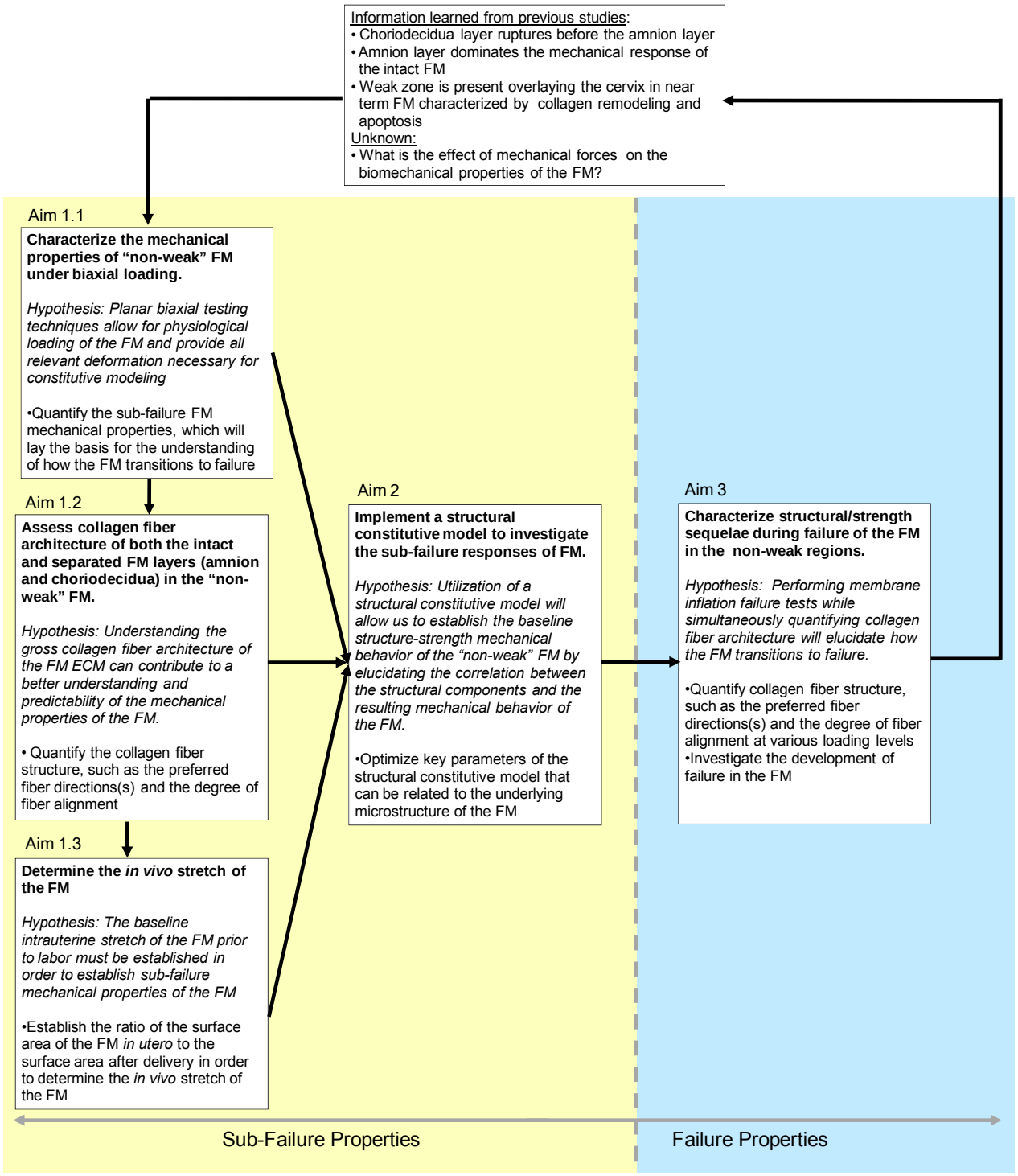

Figure 1-19. Flowchart of specific aims based. These aims of this study sought to test the overall hypothesis that establishment of the sub-failure mechanical properties of the non-weak FM will be lay the basis for understanding how the FM transitions to failure and taking this approach will help elucidate how the FM undergoes mechanical failure and what factors modulate the underlying micro-mechanical mechanisms.

2.0 CHARACTERIZE THE SUB-FAILURE STRUCTURE-STRENGTH BEHAVIOR OF THE FM UNDER PHYSIOLOGICAL LOADING CONDITIONS

2.1 INTRODUCTION

Normal pregnancy requires that the physical integrity of the fetal membranes (FM) be maintained until term delivery. Timely rupture of the FM is thus a vital part of term labor[1]. In the past, weakening and rupture of the FM were attributed to the mechanical stresses of the contractions of labor[14]. This is clearly inconsistent with the 10% of term and 40% of preterm births in which FM rupture precedes contractions. It is now established that animal and human FM undergo extracellular matrix remodeling and apoptosis in late gestation [56, 62, 104]. In the human FM, it has been demonstrated that these biochemical changes are focused on the zone of the FM overlying the cervix and that this zone overlying the cervix is physically weaker than the remaining FM [58, 61-63]. It is presumed that FM rupture initiates within this "weak zone," but it is not at all clear how this occurs.

Tissue failure, as occurs when the FM ruptures, is a unique event in normal human physiology. Other tissue failures (e.g. bone fracture, skin tears, vascular aneurysms) are all pathological processes. Because tissue failure typically occurs as a result of a pathological process and not normal function, the biomechanics of soft tissue failure is generally poorly understood. Moreover, the biomechanics of FM failure must be extrapolated from the behavior

of the FM under sub-failure conditions. Therefore, in order to understand the FM failure (rupture), the sub-failure behavior of the FM must first be characterized. In particular, the complete stress-strain response of the FM from the unloaded state until failure needs to be established so that a sub-failure stress-strain model for "non-weak" FM (tissue from regions distal to the paracervical weak zone [61, 62]) can be developed. This model can then be extrapolated to rupture conditions and used to investigate the physical basis of the FM "weak zone" [101]. In particular, structural stress-strain models can elucidate the correlation between the strength enhancing biological components of the FM, such as collagen, and mechanical behavior. Thus, by investigating the structure-strength relationship of "non-weak" FM, one can then begin to understand how the structure-strength relationship of the FM is altered in the "weak zone" resulting in FM rupture. In addition to modeling, the direct effects of stretch on FM failure need to be investigated and can only be done under sub-failure conditions [101].

The objective of the present study was to accomplish the endpoints of Specific Aim 1.1 and 1.2: Characterize the mechanical properties of the "non-weak" FM under biaxial loading and assess collagen fiber architecture of both the intact and separated FM layers (amnion and choriodecidua) in the "non-weak" FM, respectively. Planar biaxial testing techniques allow for physiological loading of the FM and provide all relevant deformation necessary for constitutive modeling [103]. Additionally, Soft connective tissues, such as the FM, can efficiently bear tensile forces due to their collagen fibers, and the tissue can endure the greatest tensile stresses in the direction in which the collagen fibers are oriented. Thus, understanding the gross collagen fiber architecture can contribute to a better understanding and predictability of the mechanical properties of soft tissues.

2.2 PROTOCOLS

2.2.1 Tissue procurement and preparation

FM specimens were collected from women undergoing Cesarean section or Vaginal deliveries at MetroHealth Medical Center, Cleveland Ohio after normal term (37-42 weeks) pregnancies. A CWRU/MetroHealth Medical Center institutional review board (IRB) approved protocol was utilized. FM of patients with clinical chorioamnionitis, meconium, maternal diabetes, or multiple gestations were specifically excluded. For these initial studies, FM fragments from regions distant from the "weak zone" as determined by methods previously described were selected [61, 62]. Fresh FM fragments were stored in 1X Minimum Essential Medium and shipped to Pittsburgh, PA overnight on ice. FM specimens were tested on the day of receipt. In order to prepare specimens for planar biaxial mechanical testing, a 20 mm x 20 mm square was dissected from the intact FM specimens sent to our laboratory. Four fiducial markers were placed in the center of the tissue in a 2x2 array (Figure 2-1a). Two loops of 5-0 polyester suture of equal length were attached to each side of the specimens via stainless steel hooks.

2.2.2 Estimation of physiological loading

A physiologic membrane tension (**T**) of 35 N/m was used to estimate the sub-failure stress, which was determined through the Law of LaPlace using a thin shell approximation [101]. This law states a relationship between pressure, surface tension, and curvature of the surface of the FM and can be expressed as follows:

$$T = \tfrac{1}{2}(P \bullet R) \tag{2-1}$$

where T is the mean membrane tension (force/unit length), P is the internal pressure, and R is the estimated local radius of the FM [101]. P was assumed to be 10 mmHg [106], and R is based upon the volume of the FM at term [106, 107].

Note that in the present study membrane tension was used as opposed to a stress (force/unit area) [108]. Utilization of membrane tension eliminated the need for accurate thickness measurements, which can vary over the surface of the FM, in stress calculations [108]. Additionally, both layers of the FM did not bear equal amounts of load. The choriodecidua layer is mostly cellular, while the amnion layer dominates the mechanical response of the FM [12]. Thus, including the thickness of the choriodecidua layer does not accurately represent the load-bearing cross-sectional area and may contribute inaccurate stress calculations [108].

2.2.3 Planar biaxial mechanical testing

Specimens were prepared as described above and were then mounted into the planar biaxial testing device and aligned with the x_1 and the x_2 axes of the device (Figure 2-1). During testing, specimens were not aligned to any anatomic orientation.

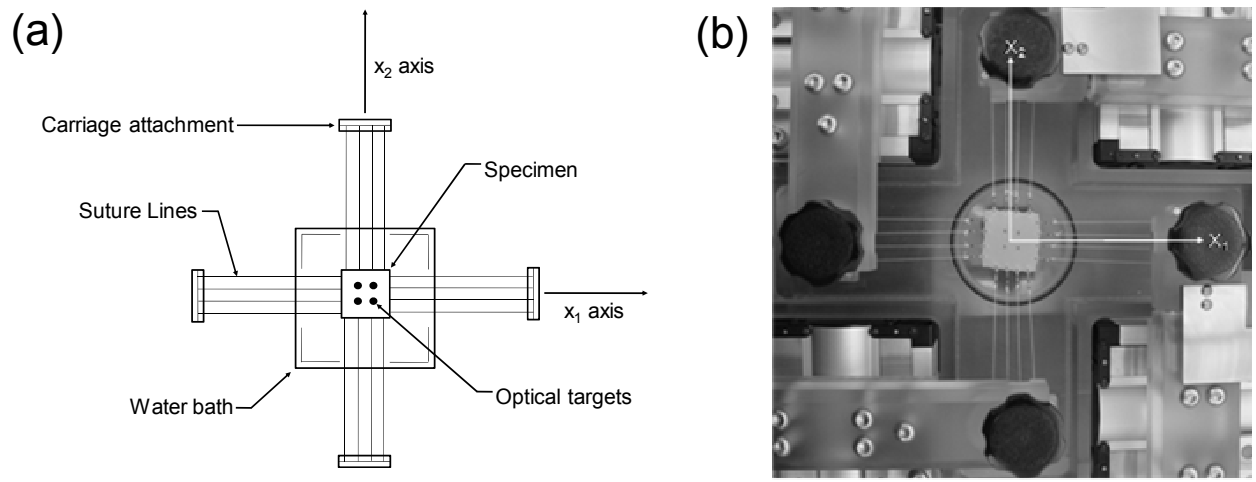

Figure 2-1. (a) Biaxial mechanical experimental setup and (b) photo of biaxial testing device, showing the device's x_1 and x_2 axes.

All testing was performed with the specimen completely immersed in an aqueous phosphate buffered solution (PBS) (pH 7.4) at room temperature. A detailed description of the biaxial testing device has been previously reported [109, 110]. Four fiducial markers attached to the specimen were used to optically measure its deformation during the test.

During mechanical testing, a membrane tension (**T**) was applied along each axis and was ramped at ~0.1%/sec to a peak value depending upon the protocol using a triangular waveform. A membrane tension of 35 N/m was used to estimate the sub-failure stress (See section 2.2.2). Specimens were first be preconditioned for 10 contiguous cycles, following five loading protocols: T_{11}:T_{22} = 0.5:1, 0.75:1, 1:1, 1:0.75, and 1:0.5, where T_{11} and T_{22} are the applied tensions in the x_1 and x_2 directions, respectively [108]. This was done for 8 specimens.

2.2.4 Data Analysis

Due to effects of mechanical preconditioning on the FM, a natural, unloaded reference state as well as a post-preconditioned, unloaded reference state can be defined. From the measured marker positions of each reference state, the deformation gradient tensor **F** associated with the deformation caused by preconditioning was determined using standard methods [103]. For this study, the natural, unloaded reference state (stress free state prior to preconditioning) was used to analyze the mechanical data.

As discussed in section 2.2.1, four fiducial markers attached to the specimen were used to optically measure its deformation during the test, and from these measurements, one can define Areal Strain as:

$$Areal\ Strain = (\lambda_1 \cdot \lambda_2) - 1 \tag{2-2}$$

where λ_1 and λ_2 are the axial stretch ratios in the x_1 and x_2 directions, respectively. Note that stretch (λ) is defined as the current length (L) divided by the original length of the collagen fiber ($L_\circ$) [$\lambda = L/ L_\circ$].

In order to investigate the overall mechanical behavior and eliminate directionality dependencies of the intact FM, average tension and Areal Strain values were computed:

$$Average\ Tension = \left(\frac{T_{11} + T_{22}}{2} \right) \tag{2-3}$$

The tangent modulus of each point on the Average Tension-Areal Strain curve was calculated and plotted against Areal Strain (Figure 2-2). The maximum tangent modulus (MTM) was the treated tangent modulus obtained and was the point at which there was no further increase in the tangent modulus (Figure 2-2). The upper bound areal strain (Areal $Strain_{ub}$) was the strain at which all collagen fibers were fully straightened and corresponded with the upper

bound tension (T_{ub}). The maximum tension (T_{max}) and the maximum areal strain (Areal $Strain_{max}$) was obtained under the physiologic loading level, 35 N/m.

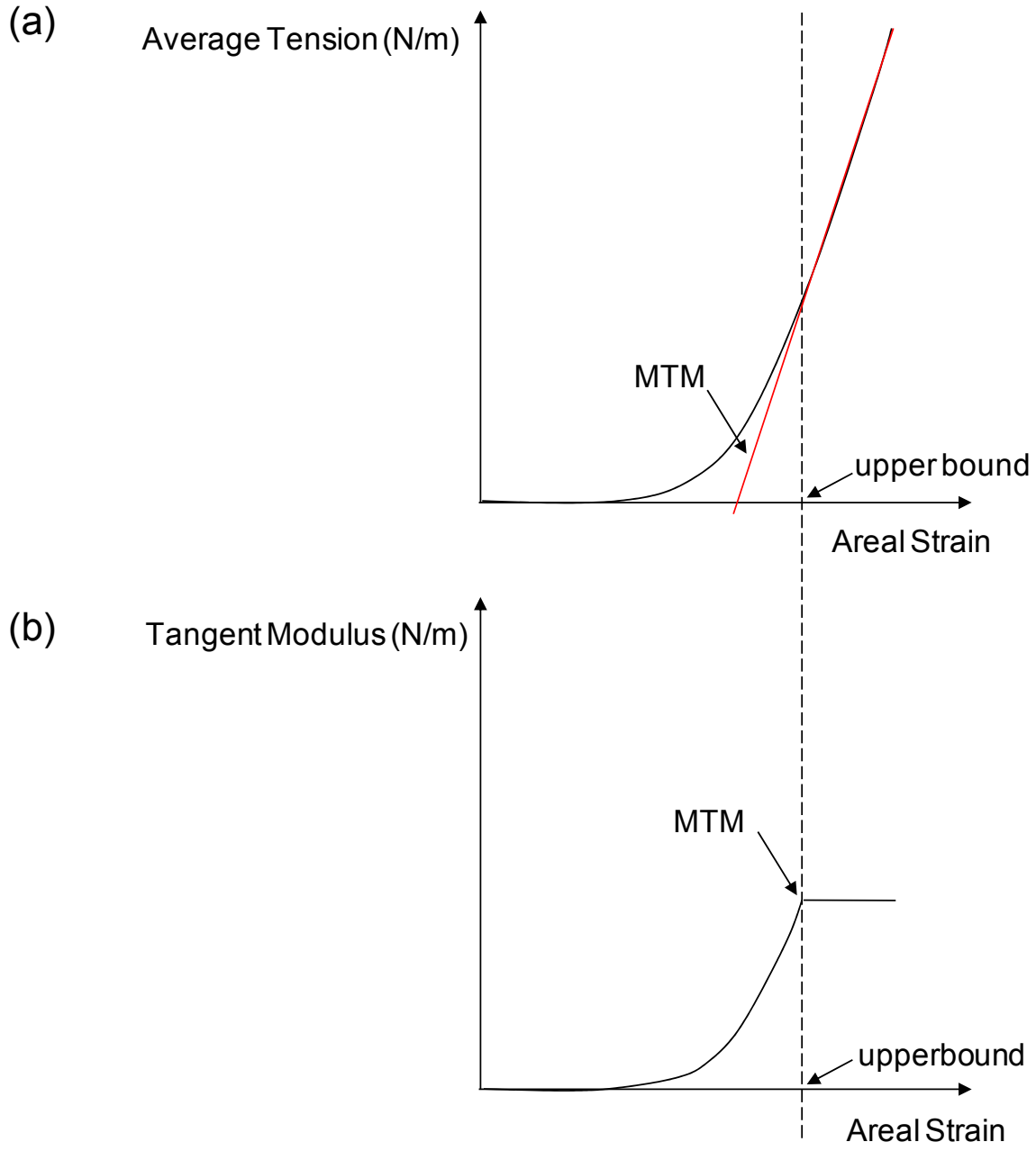

Figure 2-2. (a) A representative Average Tension-Areal Strain curve, where the tangent modulus is calculated as the slope at each point of the Average Tension-strain curve, as shown in (b). Once the tangent modulus reaches a plateau, the maximum tangent modulus (MTM) will be reached, and all collagen fibers will be recruited. The Areal Strain where this occurs is defined as the upper bound Areal Strain (Areal $strain_{ub}$). The Areal $Strain_{ub}$ is also evident on the Average Tension-Areal strain curve as the point where the Average Tension-Areal strain curve becomes linear.

2.2.5 Histological analysis

The following histological analysis was performed to assess the collagen crimp structure in the unloaded and loaded states. First, a section of intact FM was fixed with 0.5% glutaraldehyde in an unloaded state. Next, a 20 mm x 20 mm square section of intact FM was prepared as described above for mechanical testing. The specimen was then mounted into the planar biaxial testing device and aligned with the x_1 and the x_2 axes of the device (note, specimens were not aligned to any anatomic orientation) (Figure 2-1) [111].

An Areal Strain of ~0.38 was applied to the specimen, which was considered sufficient to fully straighten the collagen fibers as it produced a membrane tension of ~35 N/m. While the specimen was under strain, 0.5% glutaraldehyde was added to the bath of the testing device. The strained specimen was left in 0.5% glutaraldehyde under strain for 24 hours. Finally, transverse sections were taken from the unloaded, fixed FM and from the center region of the loaded, fixed intact FM. A Picro Sirius Red stain was used to investigate the collagen crimp structure of the FM. Under polarized light microscopy, collagen fibers of the FM displayed periodic light-distinguishing bands that correspond to collagen crimp periods. In addition, a Movat's Pentachrome stain was used to investigate the bilayer structure of the intact FM, which stained cell nuclei black, stained collagen yellow to greenish yellow, and stained ground substance blue to bluish-green. All sections were imaged with a bright field microscope under 20 x magnification.

2.2.6 Small angle light scattering measurements

SALS was used to nondestructively quantify collagen fiber architecture of both the intact and separated FM layers. A detailed description of the SALS technique has been previously presented[105]. Briefly, a 4 mW HeNe continuous unpolarized laser (λ = 632.8 nm) was passed through the tissue specimen. The spatial intensity distribution of the resulting scattered light represented the sum of all structural information within the light beam envelope. The angular distribution of scattered light pattern, I(Φ), which represents distribution of fiber angles within light beam envelope, was obtained. Quantifiable information based on I(Φ) includes orientation index (OI) and preferred fiber direction (Φ_c). The orientation index (OI) was defined as the angle that contains one half of the total area under the I(Φ) distribution. Normalized orientation index (NOI) was calculated using:

$$NOI = \frac{90^o - OI}{90^o} \tag{2-4}$$

where NOI ranged from 0% for a complete random network to 100% for a perfectly aligned network [105]. To prepare specimens for SALS, the intact FM and the separated layers were first fixed with glutaraldehyde in order to prevent tissue degradation during tissue preparation [112]. The glutaraldehyde-fixed intact FM was dehydrated in graded solutions of glycerol/saline of 50, 75, 87, and 100% for an hour each [112]. This process cleared the specimens, which was necessary for accurate SALS measurements. SALS measurements were then conducted over the entire specimen surface in order to quantify the gross fiber structure of intact FM (n = 8).

2.2.7 Statistical analysis

When a mean value was presented, the standard error of the mean (SEM) was also presented. A t-test was used to evaluate the differences between the maximum stretch at T_{11} and the maximum stretch at T_{22} as well as mean NOI values. Differences were considered statistically significant when $p < 0.05$.

2.3 RESULTS

2.3.1 Mechanical behavior

The FM exhibited differences in mechanical properties relative to direction of applied tension (mechanical anisotropy) (Figure 2-3). This was demonstrated in Figure 2-3 where T_{11} vs. stretch and T_{22} vs. stretch curves are different. However, the statistical analysis used to compare the maximum stretch value at T_{11} and the maximum stretch at T_{22} resulted in a p-value of 0.300, which was not considered significant. Thus, the degree of anisotropy presented was not significant and was within the variability of the data.

The tension vs. stretch and the tension vs. areal strain curves displayed typical "toe" regions at lower values of stretch and areal strain, respectively, followed by a transition into highly linear, stiff regions (Figure 2-3 and Figure 2-4a). With increasing Areal Strain, collagen fibers continued to straighten, and the tangent modulus continued to increase (Figure 2-4b). Once the Areal $Strain_{ub}$ was obtained, all collagen fibers were fully loaded and straightened, and the MTM was achieved (Figure 2-4a, b) (Table 2-1). At this point, the tangent modulus vs. areal

stretch curve plateaued, resulting from the fact that the collagen fibers were fully straightened. The estimated physiological loading (35 N/m) was above the point where all collagen fibers became uncrimped implying that under normal intrauterine conditions the FM has little structural reserve (Figure 2-4a).

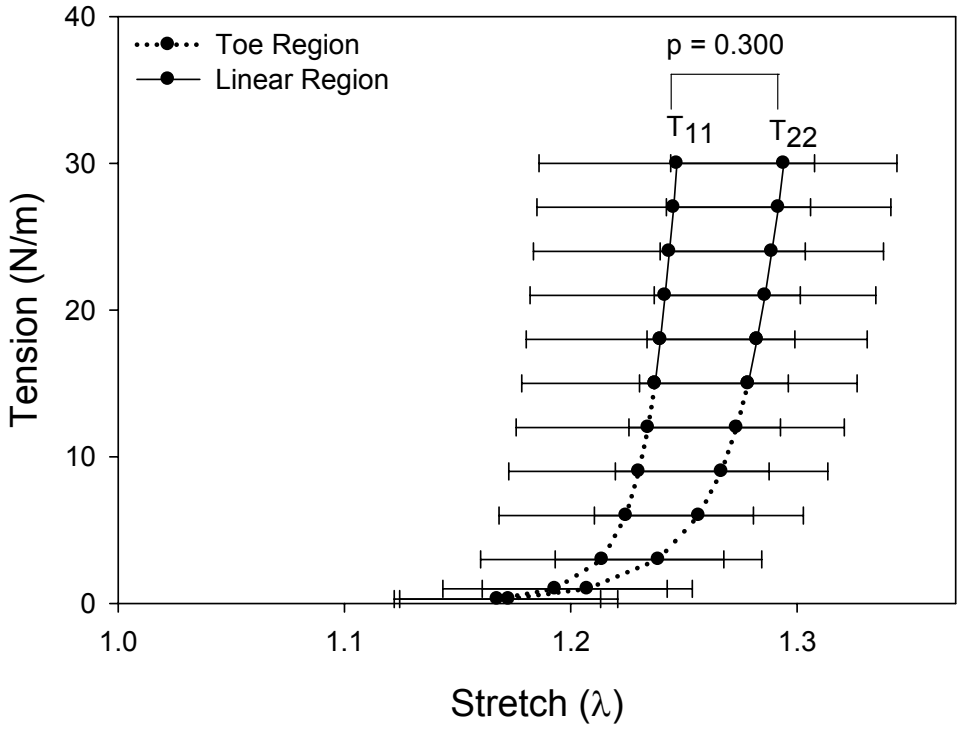

Figure 2-3. Equi-biaxial tension responses of the intact FM. The data presented is the mean and standard error of the means (SEM) of experiments with FM from 6 patients. The dotted portion of the curve is designated as the "toe" region, where the collagen fibers are crimped. The last portion of the curve, represented by the solid black line, is the linear region where all collagen fibers bear load and are straightened.

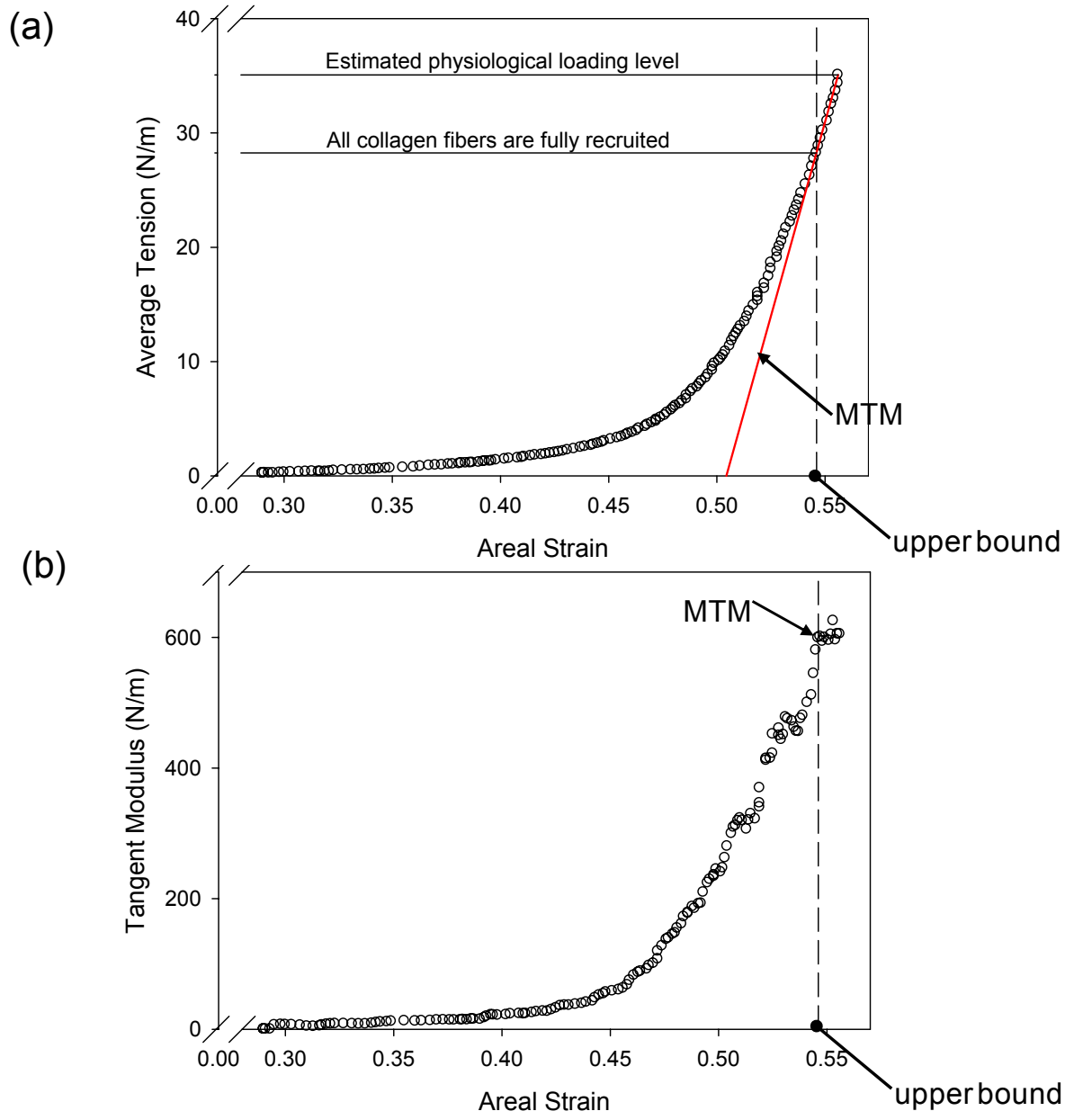

Figure 2-4. (a) Tension vs. areal strain for the intact FM. The overall tissue behavior of the intact FM was examined by calculating tension and areal strain, allowing one to neglect directionality dependencies. The tension vs. areal strain curve contained a "toe" region, which transitioned into a highly linear region. The point at which the curve transitioned into the highly linear region was designated as the upper bound and was the point at which all the collagen fibers bore load and were straightened (b) A tangent modulus was calculated for each point on the tension vs. areal strain curve. Once the tension vs. areal strain curve transitioned from the "toe" region, where collagen fibers were crimped, into the highly linear region, where collagen fibers were straight, the tangent modulus ceased to increase. This indicated that all collagen fibers were recruited and bear load.

Table 2-1. Summary of mechanical tests performed on the intact FM. This table provides the values at which the membrane ruptures.

Areal Strain$_{ub}$	T_{ub} (N/m)	MTM (N/m)	Areal Strain $_{max}$	T_{max} (N/m)
0.59 ± 0.03	25.62 ± 1.69	657.49 ± 91.78	0.60 ± 0.03	35.56 ± 0.94

2.3.2 Micro-structural characteristics

Histological results indicated that the Type I collagen of the compact sub-layer of the amnion was crimped in the unloaded state (Figure 2-5a). However, once the intact FM was strained, the collagen fibers became straightened in order to bear load, and the collagen crimp became extinguished (Figure 2-5b). The Movat's Pentachrome stain demonstrated that the amnion layer was predominantly composed of collagen (Figure 2-5c, d). Collagen in the choriodecidua was limited to the reticular layer as it was mostly cellular (Figure 2-5c ,d).

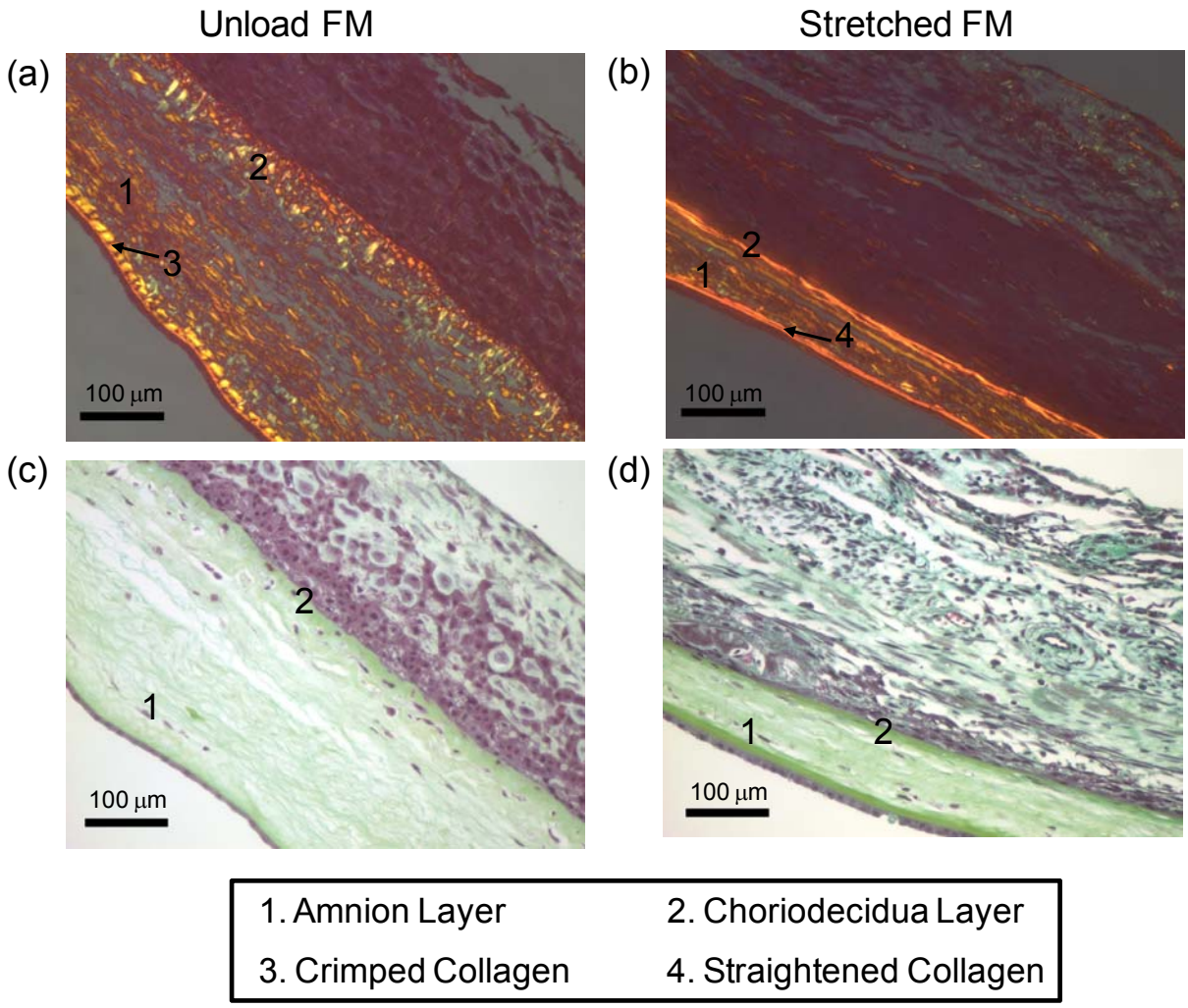

Figure 2-5. Histological results using (a,b) Picro Sirius Red and (c,d) Movat's Pentachrome stains, where numbers 1-4 refer to the amnion layer, the choriodecidua layer, the crimped collagen, and the straightened collagen, respectively. (a) In the unloaded state, Type I collagen of the amnion layer (1) was crimped (3). (b) However, once strain was applied, the collagen fibers of the amnion layer (1) bore load and straightened (4). In the FM's physiological loading state, the collagen fibers were fully straightened. (c,d) It was demonstrated that the amnion layer (1) is predominantly composed of collagen, with the exception of the epithelial cell layer, and the choriodecidua layer (2) is mainly composed of cells with less collagen than the amnion layer.

In the stress free state, we observed that the gross collagen fiber architecture of the FM and the separated layers were not homogenously aligned but did exhibit small regions of fiber alignment (Figure 2-6). The intact FM and the choriodecidua exhibited low fiber alignment (low NOI value) and were not statistically different, suggesting that both the intact FM and the choriodecidua are effectively isotropic (i.e. contain no preferred collagen direction) (Figure 2-6). However, the amnion layer did exhibit regions of high fiber alignment (higher NOI value) and was significantly more aligned than the intact ($p<0.001$) and the choriodecidua ($p=0.002$) (Figure 2-6). The modest alignment of the amnion layer probably contributed to the modest anisotropic mechanical behavior of the intact FM.

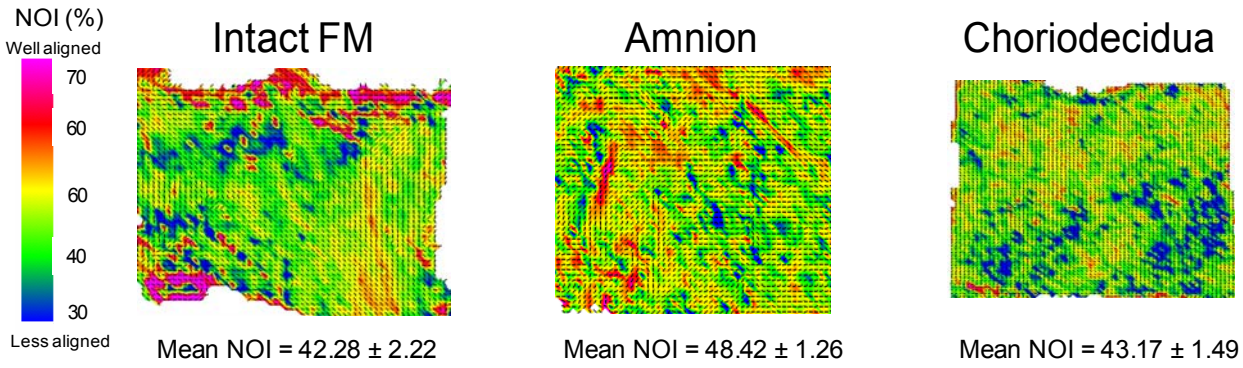

Figure 2-6. Gross fiber architecture of the intact and separated tissues in a stress free state. The gross collagen fiber architecture of the intact FM and the separated layers exhibited small regions of alignment, but the overall fiber architecture was not homogenously aligned. The amnion layer contains the greatest degree of collagen fiber alignment.

2.4 DISCUSSION

2.4.1 Effects of preconditioning on the FM

In order to fully understand FM failure, it is first necessary to characterize the sub-failure response of the FM, which will be used to lay the basis for understanding how the FM transitions to failure. By taking this approach, the complete stress-strain response of the FM from the unloaded, stress-free state until failure will be established. With this information, a sub-failure structural model for "non-weak" FM (tissue from regions distal to the paracervical weak zone [61, 62]) can be developed. This model can then be extrapolated to rupture conditions and used to investigate the physical basis of the FM "weak zone" [101].

Current failure testing techniques provide limited information on FM tissue mechanics (section 1.4.4). However, planar biaxial mechanical testing is one approach for studying sub-failure structural mechanical properties. In particular, the central target region of the test specimen for planar biaxial mechanical testing contains uniform stress and strain fields permitting data analysis to be simply performed [103]. Also, the target test region is small and located away from the outer edges of the test specimen to avoid the effects of specimen grips or tethers [103]. Planar biaxial mechanical testing can provide these necessary boundary conditions. However, planar biaxial mechanical testing requires that the FM is mechanically preconditioned. When the FM was preconditioned during planar biaxial testing, which involved cyclically loading the FM to the same stress-strain, the stress-strain response eventually became stable (i.e. the stress-strain response of last preconditioning cycles were nearly identical). As a result, preconditioning allowed for repeatable test results. However, mechanical preconditioning

caused the FM specimens to attain a different equilibrium state, referred to as the post-preconditioned, unloaded reference state (Figure 2-7).

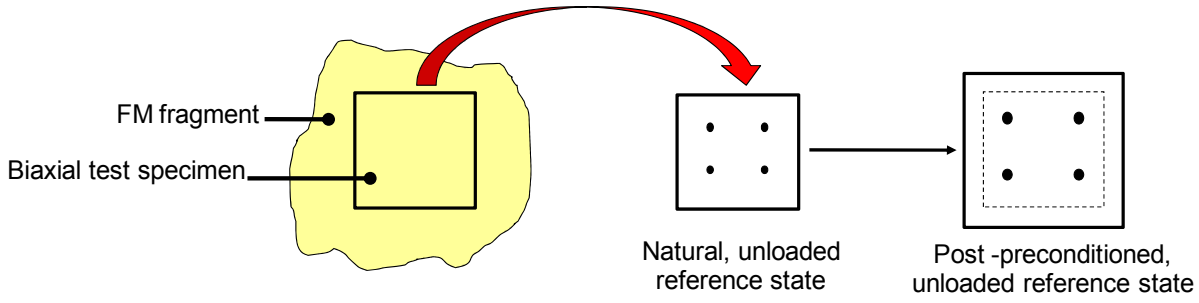

Figure 2-7. The natural unloaded, reference state refers to the stress-free reference state after the FM biaxial specimen was dissected from the FM. After mechanical preconditioning, the FM attained a different equilibrium state referred to as the post-preconditioned, unloaded reference state (i.e. dotted line was the original reference state). The natural, unloaded reference state was used for data analysis.

Thus, in order to accommodate for the effects of mechanical preconditioning on the FM, a natural, unloaded reference state (i.e. stress free state prior to preconditioning) was used because it is the only common reference state among FM specimens. Additionally, the natural, unloaded reference state is the common reference state used throughout the literature.

2.4.2 Structure-function relationships of the FM

Compelling evidence has been previously presented that suggests rupture of the FM is a result of both mechanical and biochemical processes [14, 58, 61-63]. Although the biochemical processes affecting the FM have been somewhat clarified, the effects of physical processes are less clear. In this study, we presented a more complete description of the sub-failure mechanical properties of the FM in the area distal to the defined "weak zone" overlaying the cervix, which is a required

prerequisite for extrapolation to rupture conditions. With this information, sub-failure structural models of the FM response can be developed and extrapolated to rupture conditions, allowing one to investigate how the "non-weak" FM transitions to failure.

Data presented here demonstrated that under planar biaxial mechanical testing human FM exhibited anisotropy and classical tension vs. stretch curves with characteristic "toe" regions, followed by transition into highly linear, stiff regions. Furthermore, it was found that once the collagen fibers become fully straighten, they have limited stretching capabilities thereafter. It is highly likely that the collagen fibers of the FM are loaded close to their failure stretch.

On a per specimen basis, the FM exhibited a modest degree of mechanical anisotropy (Figure 2-3), meaning that the FM's response to stretch was different along the x_1 and x_2 axes. However, this difference was not statistically significant ($p = 0.300$). In consequence, while on a specimen by specimen basis the FM exhibited a modest anisotropic response, taken as a whole, the FM is an isotropic material. In addition, it has demonstrated that the collagen structure of the intact FM was not consistently aligned (Figure 2-6), meaning that the collagen fibers were not strongly aligned in a preferred direction. Thus, FM collagen fibers are not aligned globally in relation to any anatomic structures in the uterus or placenta. In conclusion, both the biomechanical response and the structural measurements indicate that while the FM exhibited local anisotropy, the FM is an effectively isotropic material. We believe this to be important finding regarding the normal physiological function of the intact FM. This feature is essential for the accommodation of fetal movement throughout gestation. If the fibers were strongly aligned in a preferred direction, the collagen fibers would only support the fetal movement in one direction (i.e. the preferred fiber direction). Thus, the FM would likely more often rupture aberrantly with minimal force.

The average Areal $Strain_{ub}$, occurred at 99% of the average Areal $Strain_{max,}$ (Table 2-1). This indicated that once the collagen fibers began to bear load, they were recruited very rapidly. Also, the average T_{ub}, occurred at 72% of average T_{max} (Table 2-1), indicating that the collagen fibers were straightened well below physiological loading levels (Figure 2-4a). These results suggest that there is little or no structural reserve in the FM, that is, they had no ability to stretch further without breaking, which may be an important aspect of its failure properties. This biomechanical data was further supported by the histological studies demonstrating that under physiological loading of the FM, the collagen fibers were no longer undulated. They were completely straightened (Figure 2-5). The FM's physiological operating range thus appeared to be close to its failure stress.

Unlike the FM, other soft collagenous tissues (e.g. as pericardium, heart valves, and ligaments) have a large structural reserve so that their physiological loading ranges are well below their failure strengths [88, 113-117]. For example, native bovine pericardium has a physiological loading range of 0.6-1 MPa [113-115] compared with an ultimate tensile strength of 5 to 26 MPa[116]. Native porcine aortic valve leaflet tissue normally functions at 140 kPa and has an ultimate tensile strength of 600-1200 kPa. Ligaments are thought to function in the "toe" region and the early portion of the linear region of the stress-strain curve at approximately 1-6.25 MPa and have an ultimate tensile strength between 4-45 MPa depending on the age and type of ligament [88, 117]. The structural reserves in these tissues prevent them from being deformed past their failure strength. The FM did not function in the "toe" region or early portions of the linear regions. The FM collagen fibers were fully loaded under physiologic loading conditions (sub-failure). Thus, the FM has much less structural reserve than other soft tissue, which probably facilitates failure during labor.

2.4.3 Limitations

A limitation of this study is the unclear relevance of preconditioning of the FM to its *in vivo* state. Oyen *et al*. demonstrated that the FM has viscoelastic like behavior, and cyclic loading results in a drastic reduction of energy dissipation in the first cycle followed by less hysteresis on subsequent cycles [15]. Thus, when the FM was preconditioned during planar biaxial testing, which involved cyclically loading the FM to the same stress-strain, the stress-strain response eventually became stable (i.e. the stress-strain response of last preconditioning cycles were nearly identical). As a result, preconditioning allowed for repeatable test results. However, the mechanism of preconditioning and the relation between a preconditioned tissue's response and its actual *in vivo* properties is not clear. Preconditioning is an essential *in vivo* response feature in multiple tissues, such as the heart valves, ligaments, tendons, the left ventricle and the small intestine, to name a few. However, the *in vivo* state of the FM and its relationship to preconditioning is unknown. The FM is not cyclically loaded *in vivo* like the aforementioned tissues but rather constantly loaded. Thus, while preconditioning is necessary to produce repeatable results during planar biaxial testing, its relevance to its *in vivo* state is not clear. Thus, it was concluded that the most appropriate reference state was the natural, unloaded reference state.

2.4.4 Summary and Conclusions

This study provided the first data on sub-failure mechanical properties of the full thickness FM using planar biaxial experiments. This study focused specifically on areas of the FM distal to the "weak zone," where failure likely occurs [1]. Nonetheless, results indicated that the FM is an

effectively isotropic material and that that FM collagen fibers in regions distal from the "weak zone" became fully loaded and were straightened at the upper bound stretch with little stretching capabilities thereafter, suggesting that *little or no structural reserve exists in the FM.* This may therefore prove to be an important aspect of the FM's design for failure. Future studies will focus upon the FM "weak zone," which should lay the basis for the understanding how the FM transitions to failure.

3.0 DETERMINATION OF *IN VIVO* PHYSIOLOGICAL LOADING OF THE FM

3.1 INTRODUCTION

FM rupture is a normal physiological event, which occurs in the context of labor and delivery of an infant. Although it was previously thought that the membranes rupture as a result of shear forces resulting from contractions, it is now established that the FM undergoes remodeling and weakening metamorphosis during the latter part of gestation. They are programmed to degrade, evidence by the fact that at least 10% of term deliveries and at least 40% of preterm deliveries, membranes rupture prior to the onset of any uterine contractions. In addition, studies of FM in rat and mouse models have shown remodeling of the membranes is initiated with changes in tissue collagen and followed by apoptosis of the various cell layers of the membrane. Human studies demonstrated that a region overlying the cervix shows similar biochemical changes (rather than the whole membrane).

The importance of biomechanics in FM failure is also reflected in the relation between biomechanical and biochemical processes. It has been demonstrated that proteolytic enzymes play a role in membrane rupture [1], and perhaps work synergistically with mechanical forces to induce tissue failure. This speculation is supported by the known interplay between mechanical deformation and collagen degradation in soft collagenous tissues [98] [99, 100]. For example, Lee et. al demonstrated that tensile loading accelerates the prteolysis of bovine pericardium

subjected to collagenase [98]. Also, another study demonstrated that the degradation rate of collagen increased with stretch [100].

Alger and Pupkin stated that minimal growth of the FM does occurs during the final weeks of pregnancy as demonstrated by decreased mitosis [118]. Millar *et al.* suggest that disturbance to the FM ECM by means of distention stimulates remodeling of the ECM, resulting in an increase in membrane surface, where as excessive distension or inadequate remodeling could result in preterm premature rupture of the FM and preterm birth [118]. As previously discussed in section 1.4.3, this type of speculated behavior is supported by the known interplay between mechanical deformation and collagen degradation in soft collagenous tissues [98] [99, 100]. Lee *et al.* demonstrated that tensile loading accelerates the proteolysis of bovine pericardium subjected to collagenase [98], while another study demonstrated that the degradation rate of collagen increased with stretch [100]. Collagen synthesis and degradation due to proteolytic enzymes, such as MMPs, may play a role in membrane rupture [1] and perhaps work synergistically with mechanical forces (i.e. distension) to induce tissue failure. Thus, accurate measurements of membrane distension are critical in order to determine the effect of stretch on the FM.

Additionally, as a necessary prerequisite for the characterization of the mechanical properties of the FM, the baseline, intrauterine stretch of the FM prior to labor must be determined. In particular, the complete stress-strain response of the FM from the unloaded, stress-free state until failure must be established in order to develop a sub-failure structural model for "non-weak" FM. After establishing the sub-failure response of the FM, one can extrapolate this response to failure conditions and can be used to investigate the physical basis of the FM "weak zone" [101].

The objective of the present study was to accomplish the endpoints of Specific Aim 1.3: determine the *in vivo* stretch of the FM. As a necessary prerequisite for the characterization of the mechanical properties of the FM, the baseline, intrauterine stretch of the FM prior to labor must be determined, and the direct effects of stretch on FM failure must be investigated. It is hypothesized the FM is significantly stretched *in vivo*. Because FM distension cannot be directly measured *in vivo*, we must determine it indirectly from MRI images. Thus, the ratio of the surface area of the FM *in vivo* to the surface area after delivery will be established, allowing one to determine the *in vivo* stretch of the FM.

3.2 PROTOCOLS

3.2.1 Tissue procurement

Five placentas (with FM) were obtained from pregnant women delivering in the MetroHealth Medical Center. The patients were term and underwent scheduled Cesarean Section deliveries with no labor and intact membranes. Patients were scheduled for MRI within several days of the scheduled delivery. The MRI data from these patients were used for the *in vitro* surface area measurements. Upon delivery, the Moore Laboratory from Case Western Reserve University obtained the placentas with FM in order to perform surface area measurements on the tissue.

3.2.2 *In vitro* surface area measurements

Upon receipt of the placenta and FM, the umbilical cord was clamped as soon as possible. Previous studies have observed extensive differences in placental weight (due to blood loss) between placentas obtained with versus without the cord clamped. The placenta was weighed and washed in room temp PBS. The membranes were carefully dissected from the placenta as close to the placental rim as possible. The FM was also washed in room temperature PBS and carefully cut into three or four fragments. The fragments were maintained in room temperature PBS for a few minutes while the disc was traced. Tracing involved placing the placenta in a dish fetal side up. The pan was covered with a plexiglas plate (plate does not touch the disc) and a marker was used to carefully trace the disc area onto the plexiglass. This tracing was then transferred to tracing paper.

Each FM fragment was gently placed on a shallow flat tray which is then filled with room temperature PBS. The tray was about 2 cm deep. Once filled, the FM was suspended in the PBS in slight contact with the bottom of the tray. The FM fragment (if contorted) was carefully unfolded into a single layer, amnion side facing down (toward the bottom of the tray). The tray was gently agitated for 30-40 seconds resulting in spreading and suspension of the FM. The PBS was removed from the tray by vacuum aspiration leaving the wet FM fragment lying on the bottom of the tray in the same conformation as when suspended. The plexiglas sheet was then placed over the tray and the area of the fragment was traced onto the plexiglas, then transferred to tracing paper as outlined above for the disc.

To calculate the post delivery surface area from the tracings, four 10 cm x 10 cm pieces of filter paper were carefully measured and cut out. The four fragments of filter paper were weighed, and the average weight for a $100cm^2$ area was determined. Then, the placental disc

tracing and the FM fragment tracings were cut out. The tracings were then weighed, and the surface areas of each tracing were determined by comparing their weights against the "standard" calculated above. Note that for these studies, the surface area of the entire placental disc was not included in the surface area measurements. However, the disc was traced because the surface area of the placental amnion over the disc needed to measured, and separating this tissue from the placenta would have severely stretched the amnion.

3.2.3 *In vivo* surface area measurements

MRI results were first segmented using free software, Medical Image Processing, Analysis, and Visualization (MIPAV), from the NIH website (http://mipav.cit.nih.gov/). Image segmentation was done by the Moore laboratory. After segmentation was complete, the segmented images were then sent the Engineered Tissue and Mechanics and Mechanobiology Laboratory for further analysis. The result of segmenting the raw images (MRI) was a three-dimensional cloud of points, commonly referred to as a point cloud (Figure 3-1a). The point cloud data derived from segmentation served as a link between MRI and a three-dimensional geometric model. The commercial software Geomagic/Studio (Research Triangle Park, NC) was used in the three-dimensional reconstruction process. First, the point cloud data was imported into Geomagic/Studio (Figure 3-1a), and a surface wrap was performed to produce a stereolithography (STL) formatted surface (Figure 3-1b). A STL surface is a simple surface definition made by triangulating the point cloud data, which produces a set of triangular elements that only contains information of connectivity and surface normals (Figure 3-1c). The STL surface was then smoothed. The STL surface must be conservatively smoothed because raw data can lead to imperfections in the geometric quality. Next, four sided patches were defined which

capture significant topological and curvature surface characteristics. Non Uniform Rational B-spline (NURBs) based model was then constructed from the patch definition by establishing a grid of control points within the field of patches (Figure 3-1d). The NURBs format is compatible with CAD modeling tools such as SolidWorks (Dassault Systemes SolidWorks Corp. Concord, MA). After the NURBs-based geometry was constructed, SolidWorks was used to calculate the *in vivo* surface area.

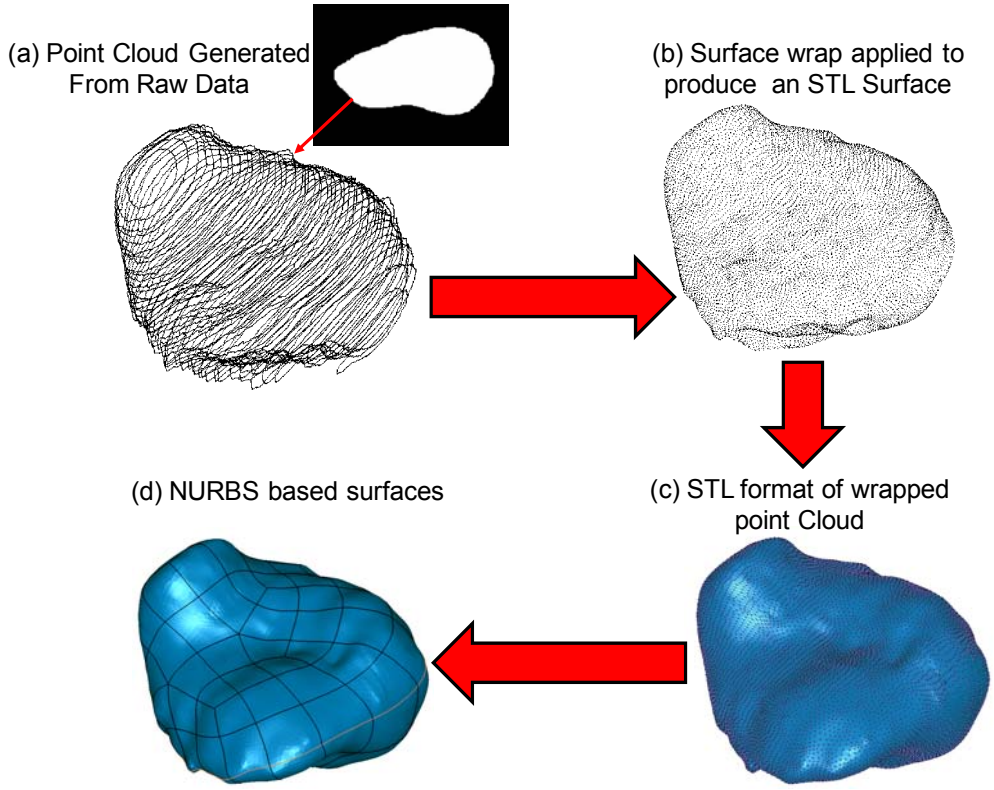

Figure 3-1. Key steps in the three dimensional reconstruction process. (a) Raw MRI data is imported into Geomagic/Studio. (b) Next, a surface wrap is applied in order to generate an STL surface. (c) The STL surface is a simple surface definition made by triangulating the point cloud from data, which produces a set of triangular elements that only contains information of connectivity and surface normals. (d) Finally, a NURBs based surface is constructed, which is compatible with commercial CAD modeling tools, such as SolidWorks**.**

3.2.4 Physiological membrane deformation analysis

In order to estimate the deformed surface area of the FM, the surface area determined from the in *vivo* measurements (section 3.2.3) was divided by the *in vitro* surface area measurements (section 3.2.2).

3.3 RESULTS

Data generated from the Moore Laboratory was implemented into Geomagic/Studio, a commercial software package, resulting in a complete three dimensional reconstruction of the FM (Figure 3-2). The surface area was then calculated based these three dimensional reconstructions.

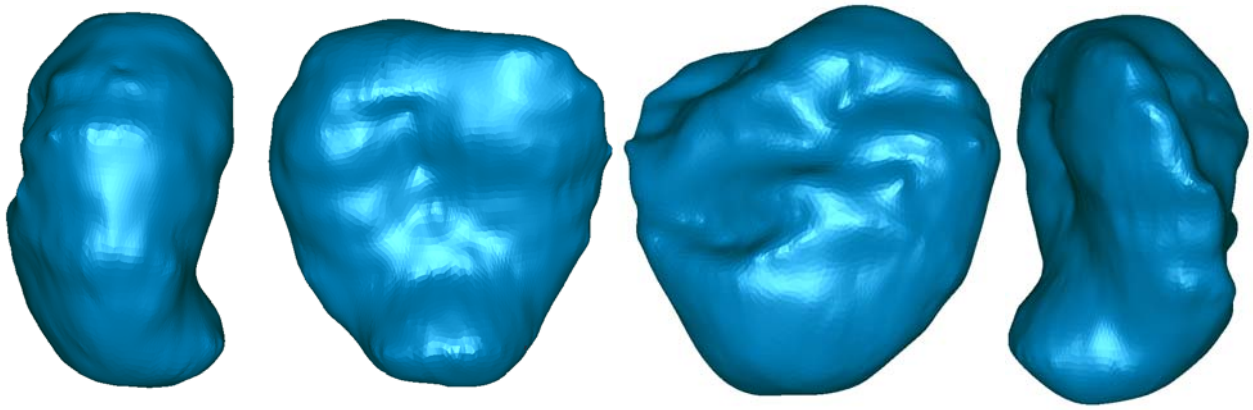

Figure 3-2. A representative image of three dimensional reconstruction of the FM from MRI. This is a 360^{o} view for one membrane**.**

The surface area of the expelled FM (i.e. *in vitro* surface area), which included the FM and the placental amnion, was 842.1 ± 59.4 cm^2 (Table 3-1). The surface area of the deformed FM (calculated with SolildWorks from the NURBS based geometry generated with Geomagic), or the *in vivo* surface area measurement, was 2151.4 ± 160.3 cm^2 (Table 3-1). The ratio of the *in vivo* surface area to the *in vitro* surface area was calculated to be 2.56 ± 0.08, which is assumed to correspond to an *in vivo* pressure prior to labor of 10 mmHg [106].

Table 3-1. Summary of *in vitro* surface area measurements, *in vivo* surface area measurements, and the calculated areal stretch of the FM.

Sample	Unloaded Surface Area (cm^2)	MRI surface Area (cm^2)	Areal Stretch
1	770.6	1917.3	2.49
2	816.7	1891.7	2.32
3	878.0	2277.0	2.59
4	1048.0	2728.0	2.60
5	697.0	1943.0	2.79
mean ± SEM	**842.1 ± 59.4**	**2151.4 ± 160.3**	**2.56 ± 0.08**

3.4 DISCUSSION

Membrane rupture has been largely pursued from a biochemical and histological perspective, but the biomechanical aspect of membrane rupture has been grossly understudied. Membrane failure at term gestation is likely to be a result of proteolytic enzyme degradation of the FM in conjunction with mechanical forces. It was hypothesized that the FM is significantly deformed

in vivo. Furthermore, it has been speculated that FM growth is minimized by the sixth month of gestation and grows approximately 0.1% thereafter [118]. At this time, the FM is significantly deformed with the increasing size of the fetus. Thus, accurate measurements of membrane distension are critical in order to determine the effect of stretch on the FM. Furthermore, the baseline, intrauterine stretch of the FM prior to labor must be determined in order to accurately interpret biomechanical data and to determine the intrauterine pressure and tension. Limited information on the surface area of the FM in vivo can be found in the literature. The few measurements that exist were based on direct physical of the maternal abdomen between the syphysis and the fundus of the uterus [119] or ultrasonography [118]. However, even with modern ultrasound equipment, the sequential cuts would not be complete and/or adequate to provide data from which to accurately compute the FM surface area. MRI, however, has been utilized to compute organ volumes and surface areas on both a clinical and research basis.

Through this study, it was determined that *in vivo* stretch of the FM was 2.56 ± 0.08. One important observation is that while there was variability in the *in vitro* surface area measurements (842.1 ± 59.4 cm^2) as well as in the *in vivo* surface area measurements (2151.4 ± 160.3 cm^2), the FM was consistently deformed to 2.56 ± 0.08. While this goal of this work was to simply determine the *in vivo* deformation, these values have immediate and future implications. First, the stretch values determined in this study will be used in Chapter 5 to estimate the physiological loading level of the FM *in vivo* and corroborate the claim that the *in vivo* pressure prior to labor is 10 mmHg [106]. Additionally, these values will be useful in future work investigating the effects of stretch on the FM ECM remodeling and resulting membrane failure.

3.4.1 Limitations

It is important to note that these membranes were obtained from patients undergoing repeat Cesarean Section deliveries, and thus, the fetuses were delivered ~2 weeks earlier. In consequence, if the fetus was left in the uterus for an additional two weeks, it is likely that these membranes would have stretched further.

4.0 IMPLEMENTATION OF A STRUCTURAL CONSTITUTIVE MODEL TO INVESTIGATE THE SUB-FAILURE RESPONSE OF THE FM

4.1 INTRODUCTION

Equations that characterize a material as well as its response to applied loads are referred to as constitutive relations because they describe the aggregate tissue behavior resulting from the internal constitution of the material [120]. As previously mentioned section 1.4.3, there are two types of constitutive models, phenomenological models and structural models.

Phenomenological constitutive models are used to describe the macroscopic nature of materials, but are independent of structural considerations. Typically, phenomenological models are "Fung-type" models, which use an exponential function to describe the tissue strain energy [36]. The "Fung-type" model has been implemented by Tong and Fung and Lanir to describe skin, Fung *et al*. and Chuong and Fung to model arteries, Chew *et al*. for pericardium, Humphrey *et al.* for pleura, and Yin *et al.* for myocardium [120]. However, while phenomenological models are efficient at capturing the nonlinear behavior of soft tissues, they are not capable of elucidating the underlying mechanisms of soft tissue behavior.

Conversely, structural constitutive model can elucidate the correlation between the underlying microstructure of a material and the resulting mechanical behavior. Structural constitutive models integrate information on tissue composition and structural information in

order to provide insight into the function, structure, and mechanics of tissue and tissue components. Structural constitutive models have been developed for various soft tissues such as lung, cartilage, myocardium, heart valves, and skin to name a few [121]. The most complete approach towards structural constitutive modeling for soft tissues has been developed by Lanir *et al*. [121]. In Lanir's modeling approach, a tissue's total strain energy is assumed to be the sum of the individual fiber strain energies, which can be linked to the tissue strain energy through tensor transformations from the fiber coordinates to the global tissue coordinates [121]. Additionally, structural information, such as fiber angular distributions, are modeled using assumed statistical distributions, with the distribution parameters numerically estimated from fits to experimental mechanical data [121]. Following Lanir's work, Sacks demonstrated the importance of including the angular distribution of collagen fibers to model soft tissues [121].

Since most *in vitro* mechanical studies have focused on the failure behavior of the FM, limited data exists for the sub-failure mechanical properties of the FM. In order to fully understand FM failure, it is first necessary to characterize the sub-failure response of the FM. After establishing the sub-failure response of the FM, one can extrapolate this response to failure conditions. In particular, the complete stress-strain response of the FM from the unloaded, stress-free state until failure must be established. With this information, a sub-failure structural model for "non-weak" FM (tissue from regions distal to the paracervical weak zone [61, 62]) can be implemented to further characterize the sub-failure properties of the FM, and this model can then be extrapolated to rupture conditions and used to investigate the physical basis of the FM "weak zone" [101]. Thus, by investigating the structure-strength relationship of "non-weak" FM, one can then begin to understand how the structure-strength relationship of the FM is altered in the "weak zone" resulting in FM rupture.

The objective of the present study was to accomplish the endpoints of Specific Aim 2: Implementation of a structural constitutive model to investigate the sub-failure responses of FM. Utilization of a structural constitutive model allows for the establishment of the baseline structure-strength mechanical behavior of the "non-weak" FM by elucidating the correlation between the structural components and the resulting mechanical behavior of the FM. The model is based on fiber-level sub-failure events using a stochastic approach and includes a statistical distribution of the fiber recruitment. Additionally, a tissue level model was implemented to quantify the fiber angular distribution within the FM. The scientific endpoint of this aim was to build on the results of specific aim 1 and characterize the response of the FM under physiological loading as well as to optimize parameters of the structural constitutive model that can be related to the underlying microstructure of the FM.

4.2 PROTOCOLS

4.2.1 Tissue procurement and preparation

FM specimens were collected from women undergoing Cesarean section or Vaginal deliveries at MetroHealth Medical Center, Cleveland Ohio after normal term (37-42 weeks) pregnancies. A CWRU/MetroHealth Medical Center institutional review board (IRB) approved protocol was utilized. FM of patients with clinical chorioamnionitis, meconium, maternal diabetes, or multiple gestations were specifically excluded. For these Studies, FM fragments from regions distant from the "weak zone" as determined by methods previously described were selected [61, 62]. Fresh FM fragments were stored in 1X Minimum Essential Medium and shipped to

Pittsburgh, PA overnight on ice. FM specimens were tested on the day of receipt. In order to prepare specimens for planar biaxial mechanical testing, a 20 mm x 20 mm square was dissected from the intact FM specimens sent to our laboratory. Four fiducial markers were placed in the center of the tissue in a 2x2 array (Fig. 3). Two loops of 5-0 polyester suture of equal length were attached to each side of the specimens via stainless steel hooks.

4.2.2 Planar biaxial mechanical testing

Specimens were prepared as described above (section 4.2.1) and were then mounted into the planar biaxial testing device and aligned with the x_1 and the x_2 axes of the device as described in section 2.2.3. During testing, specimens were not aligned to any anatomic orientation. All testing was performed with the specimen completely immersed in an aqueous phosphate buffered solution (PBS) (pH 7.4) at room temperature, and the tissue samples were not aligned to a specific anatomical direction. A detailed description of the biaxial testing device has been previously reported [109, 110, 122]. The four fiducial markers attached to the specimen were used to optically measure its deformation during the test.

The multi-protocol biaxial data generated in section 2.2.3 was used for this study. In addition to the multi-protocol testing described above, an equi-strain test, wherein an equal amount of strain was applied along the x_1 and x_2 axes of a specimen, was aperformed for constitutive modeling purposes. During equi-strain testing, specimens were first preconditioned for 10 contiguous cycles under equi-tension. After preconditioning the sample, an equi-strain test was then performed. In order to determine the appropriate strain level, an equal amount of strain was applied along the x_1 and x_2 axes of a specimen. Once one axis attained a tension level of ~35 N/m, the corresponding strain was used to perform the equi-strain test for that particular

sample. A natural, unloaded reference state was used to analyze the mechanical data (see section 2.2.4 and section 2.4.1). This was done on 8 specimens.

4.2.3 Theoretical formulation of model - assumptions

The following generalized model for planar collagenous tissue is based on previous work presented by Sacks [121]. First, one must assume that a representative volume element (RVE) can be identified that is large enough to represent the processes associated with the microstructure of the material in some average sense, yet small compared to the characteristic length scale of the microstructure (Figure 4-1). The RVE was treated as a three-dimensional continuum and was assumed the material can be modeled as a hyperelastic solid. Thus,

$$\bar{\bar{S}} = \frac{\partial W}{\partial \bar{\bar{E}}} \tag{4-1}$$

where $\bar{\bar{S}}$ and $\bar{\bar{E}}$ are the 2nd Piola-Kirchhoff stress and the Green-Lagrange strain tensors, respectively. W is the tissue strain energy density per unit volume. Within the RVE, the following assumptions were made, which were previously presented by Sacks [121]:

1. For mechanical modeling purposes, the FM was idealized as a planar network of collagen fibers embedded in a ground substance or matrix (Figure 4-1), and the hydrostatic forces generated by the matrix were ignored due to its negligible production of forces relative to forces generated by the fibers.
2. Collagen fibers are intrinsically undulated and gradually straighten with increased stretch. The load required to straighten the collagen fiber is negligible compared to the load transmitted by the stretched fiber. Also, once a fiber has been stretched to a "straightened" state, it will transmit load and will be considered linear elastic.

3. The degree of fiber undulation can vary considerably. At the tissue level, the gradual straightening of the linear elastic collagen fibers with variable undulations produces the classic non-linear stress-strain relationship.
4. A fiber ensemble is defined as a group of collagen fibers with an orientation defined by a unit normal **N** (Figure 4-1, black lines). Under the affine deformation assumption, the fiber ensemble strain, E_{ens}, will be determined from the tissue level Green's strain tensor **E** using $E_{ens} = \mathbf{N}^T\mathbf{E}\mathbf{N}$.
5. When straight, the individual collagen fibers are linear elastic with modulus K.
6. The total strain energy of the tissue is the sum of the fiber ensemble strain energies.

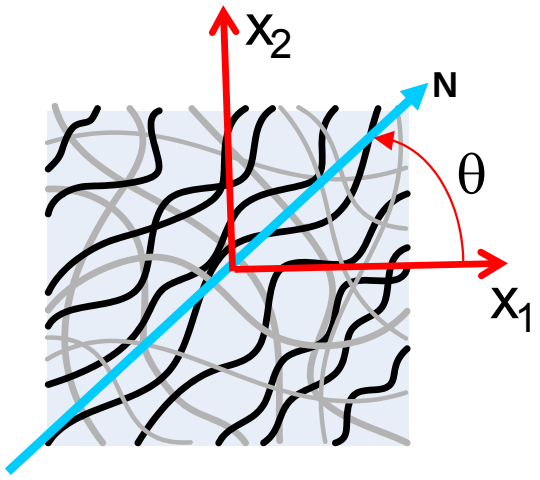

Figure 4-1. A schematic of the representative volume element idealized for the FM. The constituent collagen fibers have a distribution of undulations (crimp) and directions. For modeling purposes, an ensemble of fibers (shown here as black fibers) was defined by the unit normal N. The total tissue's mechanical response is the sum of all ensembles.

4.2.4 Fiber ensemble stress-strain relationship

Two models can be used to simulate the **effective collagen fiber stress-strain law**, or the fiber ensemble response, a phenomenological model and a structural constitutive model. The phenomenological model is given by the following equation:

$$S_{ens}(E_{ens}) = \begin{cases} d_1[\exp(d_2 E_{ens}) - 1] \text{ for } E_{ens} < E_{ub} \\ \left.\frac{\partial S_{ens}}{\partial E_{ens}}\right|_{E_{ens}=E_{ub}} \cdot (E_{ens} - E_{ub}) + d_1[\exp(d_2 E_{ub}) - 1] \text{ for } E_{ens} \geq E_{ub} \end{cases} \quad (4\text{-}2)$$

This model states that the effective collagen fiber stress, or $S_{ens}(E_{ens})$, follows an exponential form for ensemble strains, E_{ens}, less than the upper bound strain, E_{ub}, which is the strain at which all collagen fibers become straight. However, once the E_{ub} is attained, the collagen fibers were assumed to behave linear elastically, and the $S_{ens}(E_{ens})$ response is linear. In this model d_1 and d_2 are positive constants.

The structural constitutive model, which incorporates fiber recruitment and linear elastic collagen properties of the collagen fibers, was used in this study to model the fiber ensemble response of the FM. This model was derived from the force-displacement of a single collagen fiber, where it is assumed that a collagen fiber is linear in force displacement (F-δ) ([123-125]. First consider the analogous situation, force-displacement of a simple bar (Figure 4-2):

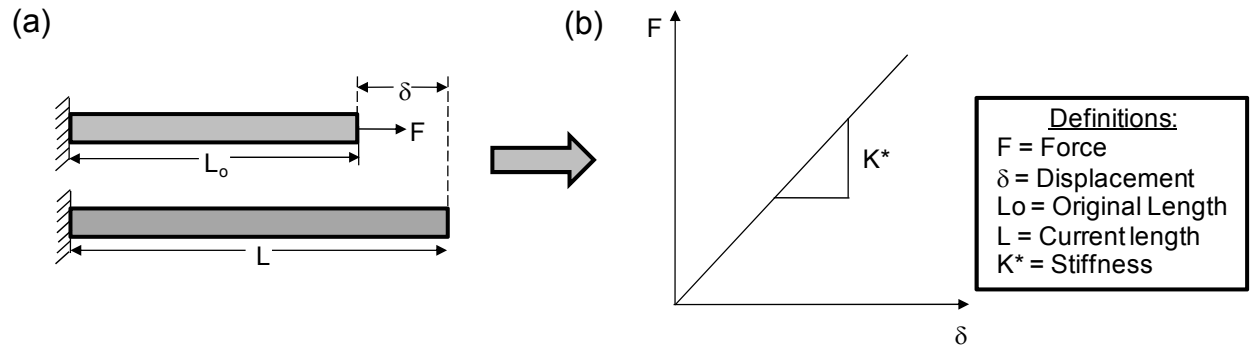

Figure 4-2. Schematic of (a) the displacement of a simple bar and (b) the resultingForce (F)-Displacement (δ) relationship. When F is applied to a bar, it undergoes a change in length, where L_o is the original length and L is the deformed length, and behaves linear elastically, with an associated stiffness, K*.

When force, F, is applied and the bar displaces (Figure 4-2a), δ, the bar behaves linear elastically (Figure 4-2b) according to:

$$F(\delta) = K^* \cdot \delta \tag{4-3}$$

where K* is the stiffness, δ is the displacement, L_o is the original length, and L is the deformed length. Next, the F-δ curve is normalized by the original cross-sectional area, A_o, and L_o, respectively (Figure 4-3).

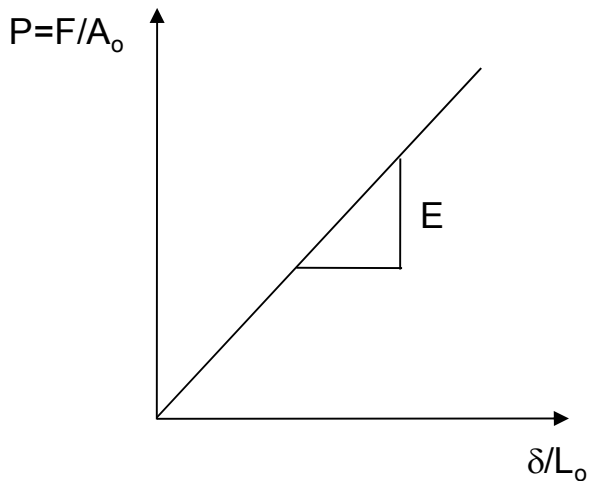

Figure 4-3. Schematic representation of the normalized F-δ curve, where E is defined as the modulus of elasticity.

Equation (4-3) now becomes:

$$P(\delta) = \frac{F}{A_o} = E\frac{\delta}{L_o} \tag{4-4}.$$

P is known as the first Piola-Kirchhoff stress (i.e. force/original cross-sectional area), and E is the modulus of elasticity.

Now, consider a single crimped collagen fiber. When force, F, is applied, the collagen fiber uncrimps and straightens (Figure 4-4a). In this state, the slack displacement, δ_s, is the displacement associated with the uncrimping of the collagen fiber, and note that the fiber does not bear load during the uncrimping, which is depicted in the F-δ curve (Figure 4-4b). Once the collagen fiber has become fully straightened, it does bear load with increased force, and the actual displacement, δ_t, is the displacement associated with the fiber as it bears load and behaves linear elastically. δ is the total displacement from the crimped state to the final displacement, and μ is the stiffness of the collagen fiber.

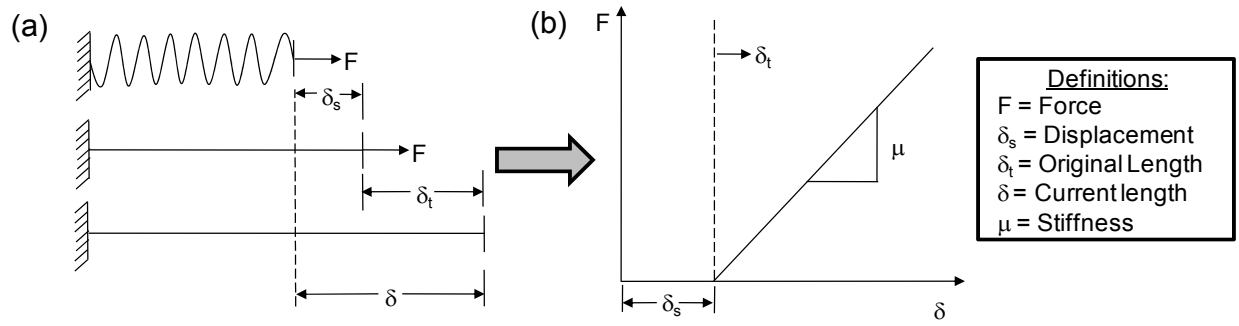

Figure 4-4. Schematic representation of (a) the displacement of a collagen fiber and (b) the associated Force (F) – Displacement (δ) relationship of a collagen fiber. (a)A collagen fiber is undulated in the unloaded state. However, when force, F, is applied, the collagen fiber uncrimps to a straightened state. This displacement is referred to as the slack displacement δ_s. Once the collagen fiber is displaced beyond its straightened state (i.e. δ_t), it bears load. (b) This behavior can also be represented graphically, where μ is the stiffness of a collagen fiber. Force the fiber does not bear load until the fiber is displaced beyond δs, and the fiber then behave linear elastically thereafter.

As in the case of equation (4-3),

$$F(\delta) = \delta_t \cdot \mu \tag{4-5}$$

and

$$\delta_t = \delta - \delta_s \tag{4-6}$$

Now, as in the case of the simple bar, the F-δ curve is normalized by A_o and L_o (Figure 4-5).

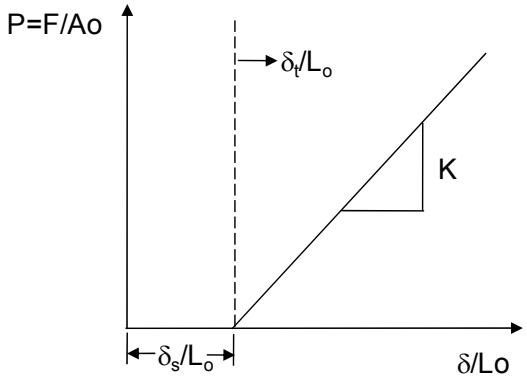

Figure 4-5. Schematic representation of the normalized F-δ curve, where K is defined as the modulus of elasticity.

Equation (4-5) now becomes:

$$P(\delta) = \frac{F}{A_o} = K \cdot \frac{\delta_t}{L_o} \tag{4-7}$$

where K is referred to as the modulus of elasticity. Substituting equation (4-6) into equation (4-7) results in the follow equation:

$$P(\delta) = K \frac{(\delta - \delta_s)}{L_o} \tag{4-8}$$

Substituting the equation for stretch (λ), $\lambda = \delta / L_o$, into equation (4-8) results in:

$$P(\lambda) = K\,(\lambda - \lambda_s) \tag{4-9}.$$

Now, in order to convert P into the second Piola-Kirchhoff stress (S), one must divide P by λ, which yeilding in the following equation:

$$S(\lambda) = K\left(1 - \frac{\lambda_s}{\lambda}\right) \tag{4-10}.$$

Next, λ is converted to a Green-Lagrange, E, strain using $E = \frac{1}{2}(\lambda^2 - 1)$:

$$S(E) = K\left(1 - \frac{\sqrt{1 + 2E_s}}{\sqrt{1 + 2E}}\right) \tag{4-11},$$

where E_s is the slack strain. Finally, a stochastic approach was used to represent the distribution of fiber slack length as a function of fiber strain. The gradual recruitment of fibers within a fiber ensemble was simulated by a statistical distribution of $D(E_s)$, which represents the probability density of fiber slack strains E_s, which describes the fraction of fibers realizing a fully straightened state at a given strain level. Thus, the final equation for the fiber ensemble stress-strain relationship is:

$$S_{ens}(E_{ens}) = K \cdot \int_0^{E_{ens}} D(x)\left(1 - \frac{\sqrt{1+2x}}{\sqrt{1+2E_{ens}}}\right) dx \tag{4-12}$$

where K incorporates the collagen fiber volume fraction for convenience. A modified Beta statistical distribution was used for D(x):

$$D(x) = \frac{x^{\gamma-1}\,(1-x)^{\delta-1}}{B(\gamma,\delta)} \tag{4-13},$$

where $B(\gamma,\delta) = \frac{\Gamma(\gamma)\,\Gamma(\delta)}{\Gamma(\gamma+\delta)}$, $x = \frac{E_{ens} - E_{ub}}{E_{ub}}$ so that $x \in [0,1]$ with the constrain that $\int_0^{Eub} D(x)\,dx = 1$.

The mean, μ, and standard deviation, σ, are given by:

$$\mu = \frac{\gamma}{\gamma+\delta} \text{ and } \sigma = \sqrt{\frac{\gamma\,\delta}{(\gamma+\delta)^2\,(\gamma+\delta+1)}} \tag{4-14}$$

Thus, the ensemble model contains the following for parameters: K, Eub, μ, and σ.

4.2.5 Tissue stress-strain relationship

Based on assumption 5, the total tissue strain energy, W, can be expressed by integrating over all values of θ:

$$W(E) = \int_{-\pi/2}^{\pi/2} R(\theta)\, w(E_{ens}(\theta))\, d\theta \tag{4-15},$$

where R(θ) is the angular distribution of the collagen fibers. Additionally, one integrates over all values of θ to determine the **tissue level stress-strain relationship:**

$$\bar{S}(\bar{E}) = \int_{-\pi/2}^{\pi/2} R(\theta) S_{ens}[E_{ens}(\theta)][N \otimes N] d\theta \tag{4-16}$$

where $\otimes$ indicates external multiplication so that $[\mathbf{N}\otimes\mathbf{N}]_{ij}=N_iN_j$ and $\mathbf{S}$ is the tissue 2nd Piola-Kirchhoff stress tensor. $R(\theta)$ was also modeled with a modified beta statistical distribution, with the mean, μ, and standard deviation, σ, described in equation (4-14), and $\theta\in[0,1]$. In component form, equation (4-16) becomes:

$$\begin{aligned} S_{11} &= \int_{-\pi/2}^{\pi/2} R(\theta)\, S_{ens}(E_{ens}) \cos^2\theta \, d\theta \\ S_{12} &= \int_{-\pi/2}^{\pi/2} R(\theta)\, S_{ens}(E_{ens}) \cos\theta \sin\theta \, d\theta \\ S_{22} &= \int_{-\pi/2}^{\pi/2} R(\theta)\, S_{ens}(E_{ens}) \sin^2\theta \, d\theta \end{aligned} \qquad (4\text{-}17).$$

4.2.6 Parameter estimation

Model parameters were obtained from the sub-failure biaxial data for both the fiber ensemble structural model and the tissue level structural model. For the fiber ensemble stress-strain constitutive relationship, the parameter, E_{ub}, must be estimated from the P_{ens}-λ_{ens} biaxial data because as mentioned previously, collagen fibers are only linear in P-λ space, which is equivalent to Force-Displacement [123-125]. Under equi-biaxial strain conditions (i.e. $\lambda_1=\lambda_2=\lambda$, $P_{12}=P_{21}=k_1=k_2=0$), the fiber ensemble stress-strain law was obtained directly from the biaxial mechanical data [121] using:

$$P_{ens} = P_{11} + P_{22} \qquad (4\text{-}18).$$

In order to determine E_{ub} and estimate K, P_{ens} vs. λ_{ens}, which was obtained from equi-strain experiments, was plotted as shown in Figure 4-6 for an intact FM tissue specimen. The tangent modulus (i.e. slope) of each point of the P_{ens}-λ_{ens} curve was calculated and plotted against λ_{ens}

(Figure 4-6), where it can be observed that the tangent modulus will eventually cease to increase with increased stretch. At this point all FM collagen fibers within the fiber ensemble have been recruited and the maximum tangent modulus (MTM) was achieved, and the corresponding stretch at this level is the upper bound stretch, λ_{ub}. K is then estimated using K = MTM. E_{ub} can be calculated from λ_{ub} by $E_{ub} = \frac{1}{2}(\lambda_{ub}{}^2 - 1)$. Thus, E_{ub} is determined and K is estimated. The remaining model parameters, K, μ, and σ can be optmized by fitting experimental equi-strain data, $S_{ens}(E_{ens})$, with equation (4-12). After μ and σ have been determined, the cumulative distribution function can be determined:

$$CD(E_{ens}) = \int_0^{E_{ens}} D(x)\,dx \text{, with } CD(E_{ub}) = \int_0^{E_{ub}} D(x)\,dx = 1 \qquad (4\text{-}19),$$

which is defined the fraction of fibers recruited at a given strain level.

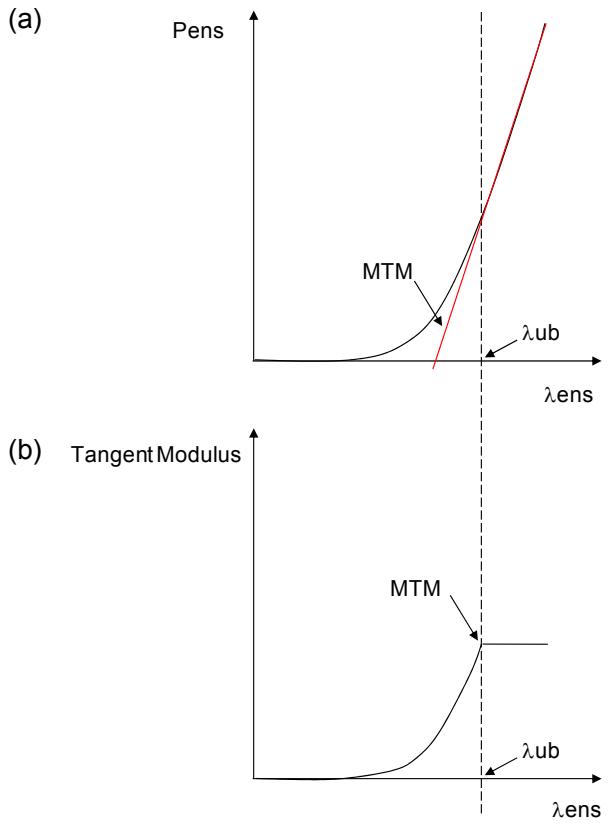

Figure 4-6. (a) A representative equi-biaxial strain test of the FM, showing the effective ensemble P_{ens}-λ_{ens} relation, where the tangent modulus is calculated as the slope at each point of the stress-strain curve, as shown in (b). Once the tangent modulus reaches a plateau, the maximum tangent modulus (MTM) will be reached, and all collagen fibers will be recruited. The stretch where this occurs is defined as the upper bound stretch (λ_{ub}). The λ_{ub} is also evident on the stress-strain curve as the point where the stress-strain curve becomes linear.

For the tissue stress-strain constitutive relationship, d_1, d_2, E_{ub}, μ, σ, were optimized by fitting the multi-protocol experimental biaxial data with equation (4-16). Note that equation (4-2) was used for $S_{ens}(E_{ens})$ in the tissue level model (equation (4-16)) in order to reduce computational time. Pilot studies verified that $R(\theta)$ parameters are independent of the form of $S_{ens}(E_{ens})$ such that the model can sufficiently fit the experimental data.

4.2.7 Statistical analysis

When a mean value was presented, the standard error of the mean (SEM) was also presented. A t-test was used to evaluate the differences between various strain levels for the $S_{ens}(E_{ens})$ fit predicted from the ensemble level model and the predicted $S_{ens}(E_{ens})$ response from the tissue level model. Differences were considered statistically significant when $p < 0.05$.

4.3 RESULTS

4.3.1 Fiber ensemble structural model results

The fiber ensemble structural model was able to fully capture the ensemble level response as evidenced by high R^2 values, with a minimum R^2 of 0.9989 (Table 4-1). A summary of all fiber ensemble modeling results are presented in Table 4-1.

Table 4-1. Summary of estimated model parameter from the fiber ensemble constitutive model (n=8). Note that since μ and σ are non-linear parameters, the mean value presented in this table do not represent the mean response value. Also, μ and σ are normalized by E_{ub} in this table.

Sample	K (MPa)	μ	σ	E_{ub}	R^2
1	4.04	0.93	0.07	0.25	0.9989
2	3.99	0.87	0.10	0.14	0.9991
3	4.14	0.93	0.07	0.29	0.9991
4	3.04	0.92	0.07	0.38	0.9992
5	4.97	0.89	0.10	0.17	0.9994
6	4.32	0.92	0.06	0.33	0.9997
7	7.38	0.92	0.08	0.19	0.9996
8	8.64	0.91	0.08	0.17	0.9995
mean ± SEM	**5.06 ± 0.68**	**0.91 ± 0.01**	**0.08 ± 0.01**	**0.24 ± 0.03**	**0.9993 ± 0.0001**

The P_{ens}-λ_{ens} curve displayed typical "toe" regions at lower values of stretch followed by a transition into highly linear, stiff regions (Figure 4-7a). With increasing stretch, collagen fibers within the ensemble continued to straighten, and the tangent modulus continued to increase (Figure 4-7b). Once the λ_{ub} was obtained, all collagen fibers were fully loaded and straightened, and the MTM was achieved (Figure 4-7b). At this point, the Tangent Modulus-λ_{ens} curve plateaued, resulting from the fact that the collagen fibers were fully straightened. The estimated physiological loading was above the point where all collagen fibers became uncrimped implying that under normal intrauterine conditions the FM has little structural reserve (Figure 4-7a). Note, failure did not occur during loading.

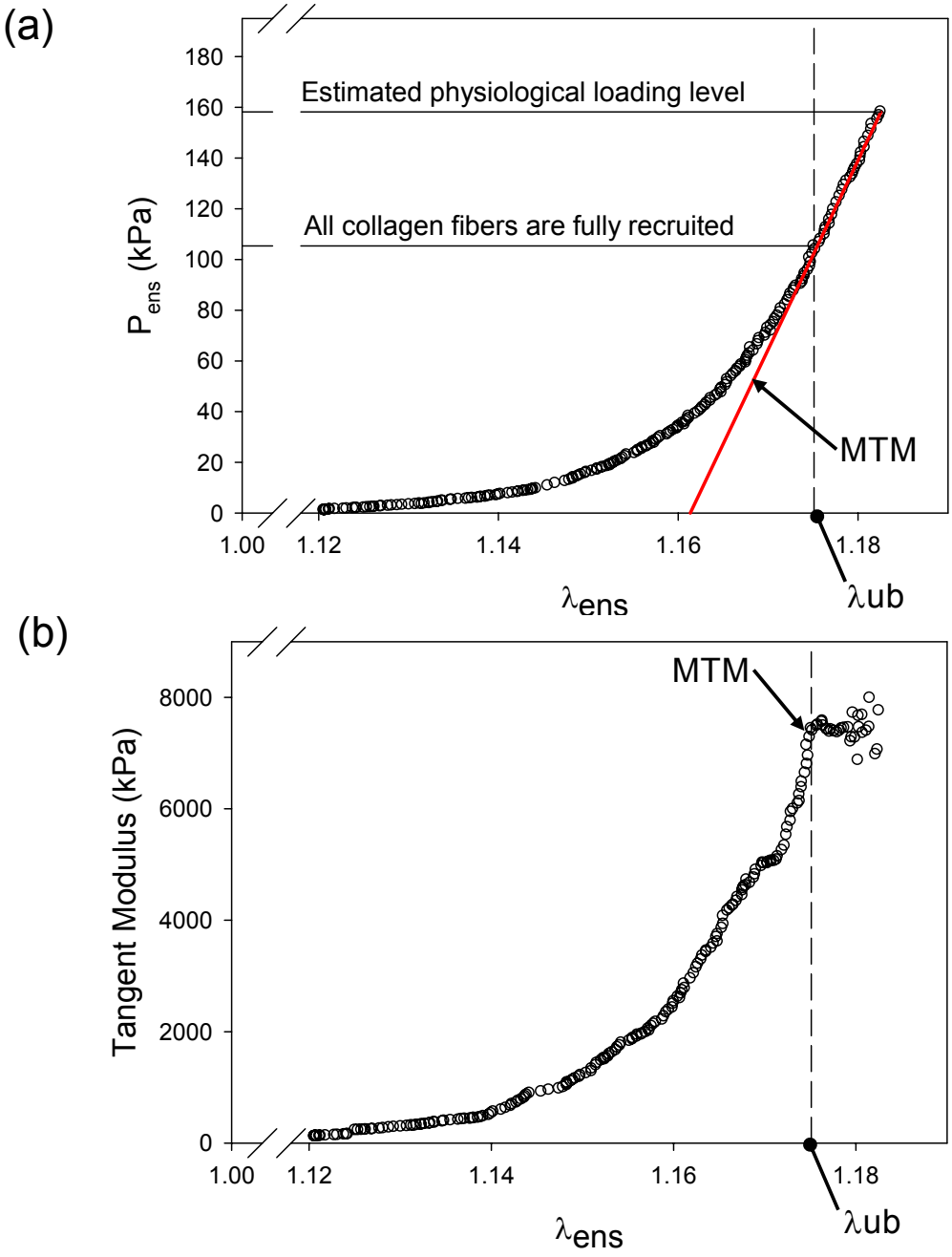

Figure 4-7. (a) A representative image of P_{ens}-λ_{ens} curve produced from an equi-strain test. (b) The tangent modulus is calculated as the slope at each point along the P_{ens}-λ_{ens} curve. A plateau region is achieved once, the tangent modulus no longer increases (i.e. the slope is no longer increasing and has become constant). At this point, the maximum tangent modulus (MTM) is attained and it demarcates the point where all collagen fibers are recruited. The stretch associated with this point is termed the upper bound stretch, λ_{ub}. The λ_{ub} is also evident on the stress-strain curve as the point where the stress-strain curve becomes linear.

As mentioned above, the structural model was able to sufficiently capture the effective fiber response as evidenced by high R^2 values (Table 4-1) and is graphically demonstrated in the representative S_{ens}-E_{ens} curve (Figure 4-8a). The modulus of elasticity, K, of the representative sample was determined to be 7.38 MPa. The E_{ub} for the representative sample was concluded to be 0.19, whereas the maximum strain attained was 0.20. The parameters μ and σ of the modified beta distribution were 0.17 ($0.92*E_{ub}$) and 0.02 ($0.08*E_{ub}$), respectively, which indicated that the FM collagen fibers rapidly recruited and were straightened well below physiological stress levels (Figure 4-8a). This phenomenon is further reinforced with the cumulative fiber distribution results (Figure 4-8b). Only a small fraction of collagen fibers were recruited at low strain values (Figure 4-8b). However, at a strain value of 0.128, 50% of the collagen fibers were recruited, and at a strain value of 0.186, 75% of the collagen fibers were recruited. Thus, most recruitment occurred close to the E_{ub} (0.19) (Figure 4-8b).

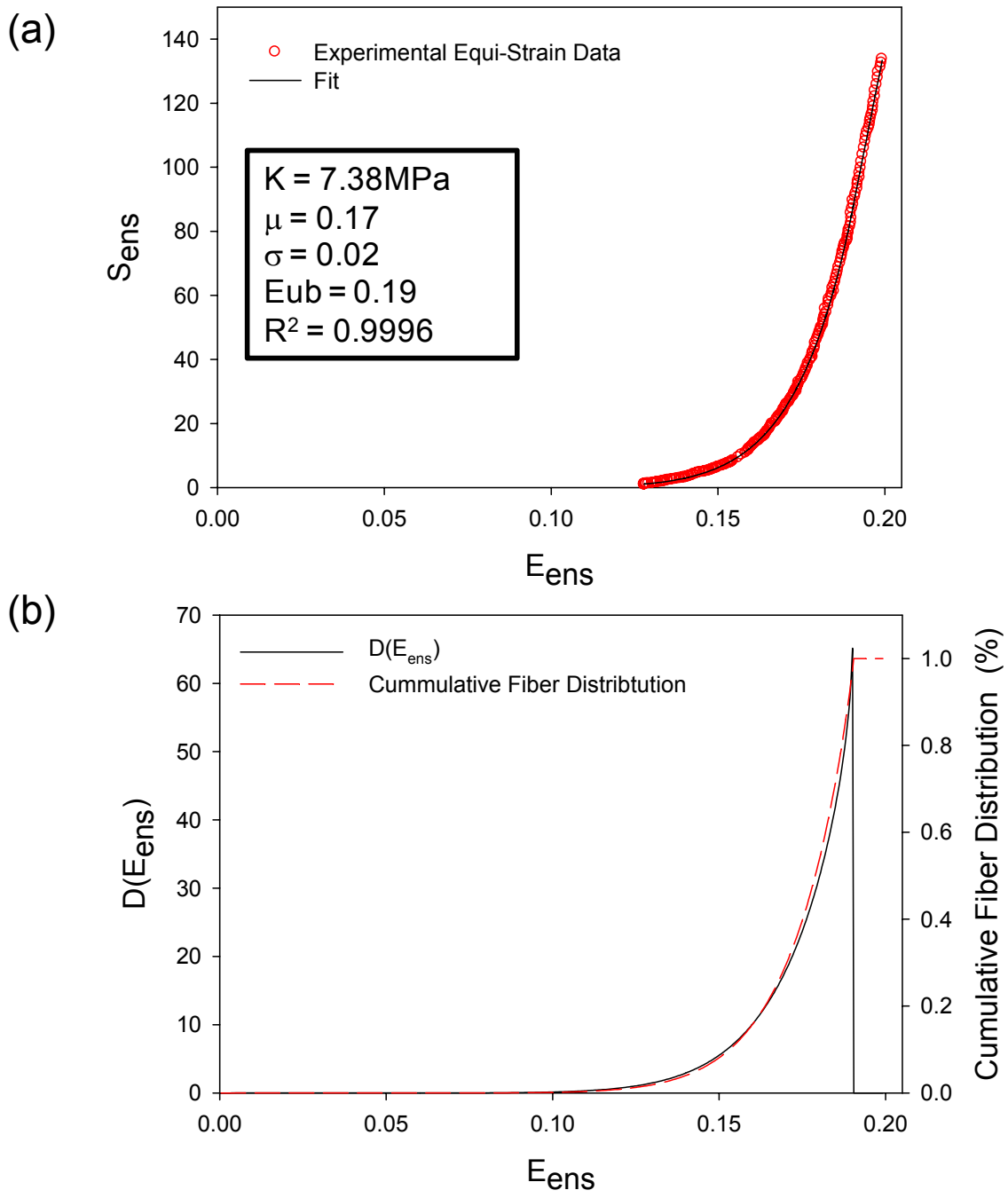

Figure 4-8. (a) The fiber ensemble constitutive model was able to effectively fit the equi-strain derived S_{ens}-E_{ens} data. The predicted model parameters suggest that the collagen fibers of the FM are recruited at high strain values, but once recruitment began, it occurred rapidly. (b) This behavior is further reinforced upon inspection of the $D(E_{ens})$-E_{ens} plot and the Cumulative Fiber distribution-E_{ens} plot. The mean of the $D(E_{ens})$-E_{ens} is skewed close to 1 and the standard deviation of the distribution is tight, indicative of late, but rapid collagen fiber recruitment.

The average modulus of elasticity, K, was concluded to be 5.06 ± 0.68 MPa and the average upper bound strain, E_{ub}, was determined to be 0.24 ± 0.03. The parameters μ and σ are nonlinear parameters and cannot be averaged. Thus, each $D(E_{ens})$-E_{ens} curve for each sample was plotted together (Figure 4-9), and $D(E_{ens})$ was averaged at each individual strain level, which produced a mean $D(E_{ens})$-E_{ens} curve. This mean curve was then fit with a modified beta distribution to produce a "mean" μ of 0.91 and a "mean" σ of 0.08. It can be seen from Table 4-1 and Figure 4-9 that there was little variation in μ and σ between samples.

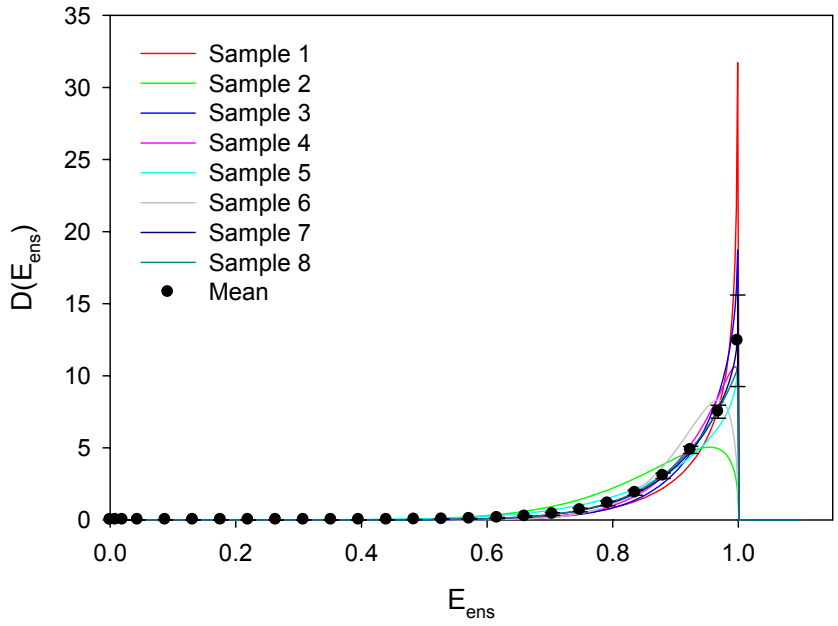

Figure 4-9. The "mean" recruitment distribution, $D(E_{ens})$, for 8 samples, with a "mean" μ of 0.8831 and an "mean" σ of 0.1092. Note, there was minimal variability in the μ and σ of the between the 8 samples, evidence by similar curves.

4.3.2 Tissue level structural model results

The tissue level structural constitutive model was able to capture the tissue response to loading reasonably well, with an average R^2 value of 0.9061 ± 0.0292 for the S_{11} vs. E_{11} data and an average R^2 value of 0.8946 ± 0.0439 for the S_{22} vs. E_{11} data. While these fits were not as good as those of the fiber ensemble model, the results are reasonable for such a wide range of stresses associated with multi-protocol testing and the delicate nature of the FM. A summary of all tissue level modeling results are presented in Table 4-2.

Table 4-2. Summary of estimated model parameter from the tissue level constitutive model (n=8). Note that since d_1, d_2, μ, and σ are non-linear parameter, the mean value presented in this table do not represent the means response value.

Sample	d_1	d_2	E_{ub}	μ	σ	$R11^2$	$R22^2$
1	8.61×10^{-3}	29.38	0.56	-24.33	20.48	0.8478	0.9024
2	4.73×10^{-3}	39.56	0.32	-57.66	10.24	0.9840	0.9812
3	6.33×10^{-5}	54.62	0.24	-67.39	16.43	0.7379	0.6054
4	1.48×10^{-3}	51.80	0.35	-88.94	11.83	0.9644	0.9673
5	1.84×10^{0}	61.00	0.20	-4.45	9.18	0.8712	0.9580
6	1.03×10^{-4}	37.97	0.34	44.39	13.36	0.9574	0.9723
7	6.05×10^{-4}	33.98	0.53	-23.84	19.38	0.9481	0.9072
8	3.67×10^{-6}	88.37	0.23	15.90	14.84	0.9381	0.8631
mean ± SEM	**0.23 ± 0.23**	**49.58 ± 6.75**	**0.35 ± 0.05**	**-25.79 ± 15.73**	**14.47 ± 1.45**	**0.9061 ± 0.0292**	**0.8946 ± 0.0439**

A representative plot of the multi-protocol data with the model fits, the predicted $S_{ens}(E_{ens})$ response, and the fiber angular distribution, $R(\theta)$ are presented below (Figure 4-10a-d). For the representative sample, the predicted E_{ub} was 0.34, and μ and σ were 44.39 and 13.36,

respectively. On first inspection of the R(θ) results (Figure 4-10d), it would appear that the FM has a strong degree of alignment evidence by the small σ value of the R(θ) curve. Note that if σ was large, this would indicate that there are more fibers present at different angles. This result was not consistent with results and conclusions presented in section 2.3.2 and section 2.4.2, respectively. However, as previously noted, the specimens were not aligned to a specific anatomical direction, and based on inspection of Table 4-2, there is a wide variability among the predicted R(θ) parameters (i.e. μ and σ). Since μ and σ are nonlinear parameters, they cannot be readily averaged. Thus, in an effort to present an mean R(θ) curve, each R(θ) value at each angle from -90 to 90 was averaged to produce an mean R(θ) (Figure 4-11). The R(θ) curve had a large standard deviation with no peaks. Based on this analysis, fiber directions within the FM are random (Figure 4-11).

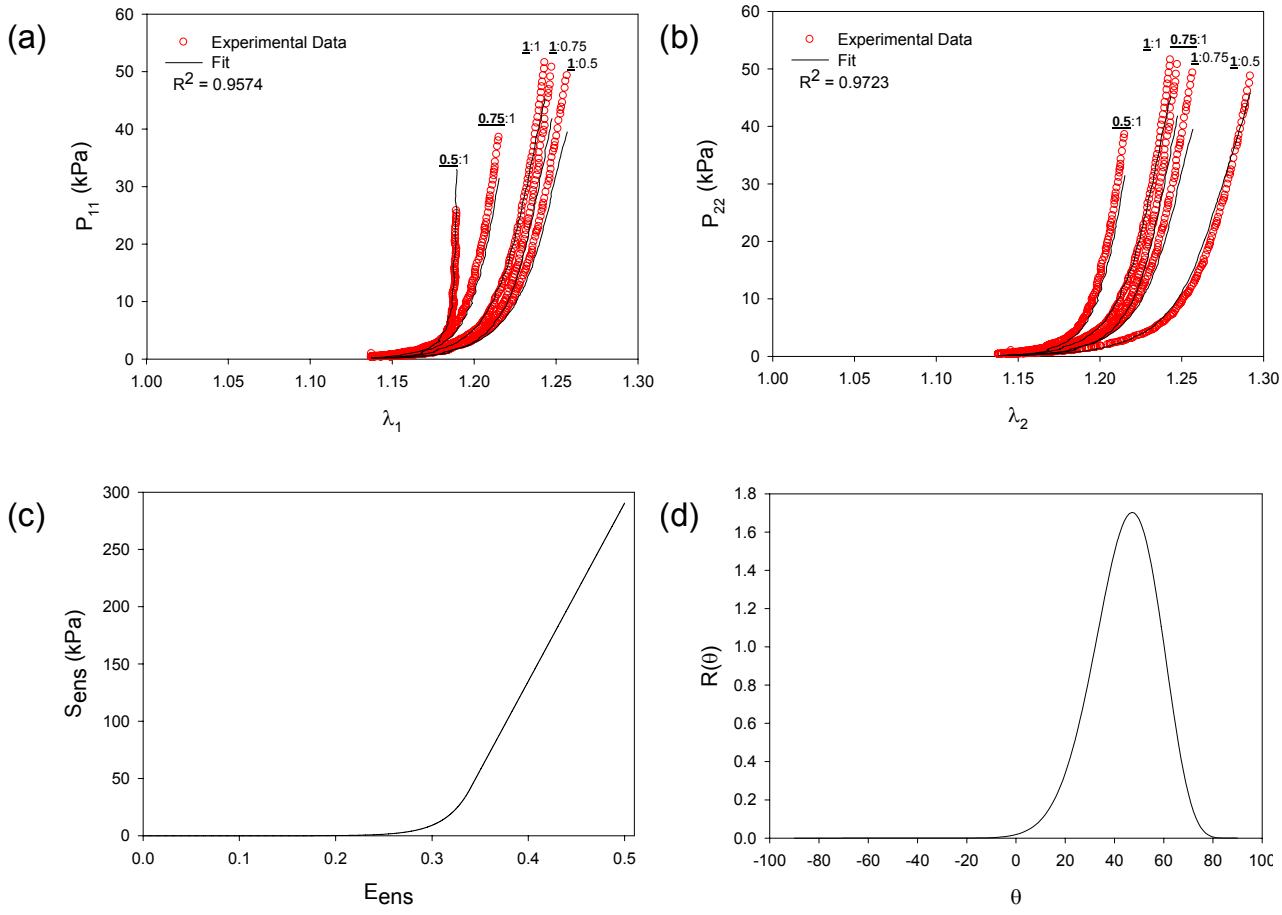

Figure 4-10. Representative image of tissue level modeling results. (a,b) The tissue level structural model was able to fit the multiprotocol biaxial data reasonable well. (c) The tissue level structural model was also able to predict the S_{ens}-E_{ens} response from tissue level, biaxial multiprotocol data as well as (d) the fiber angular distribution.

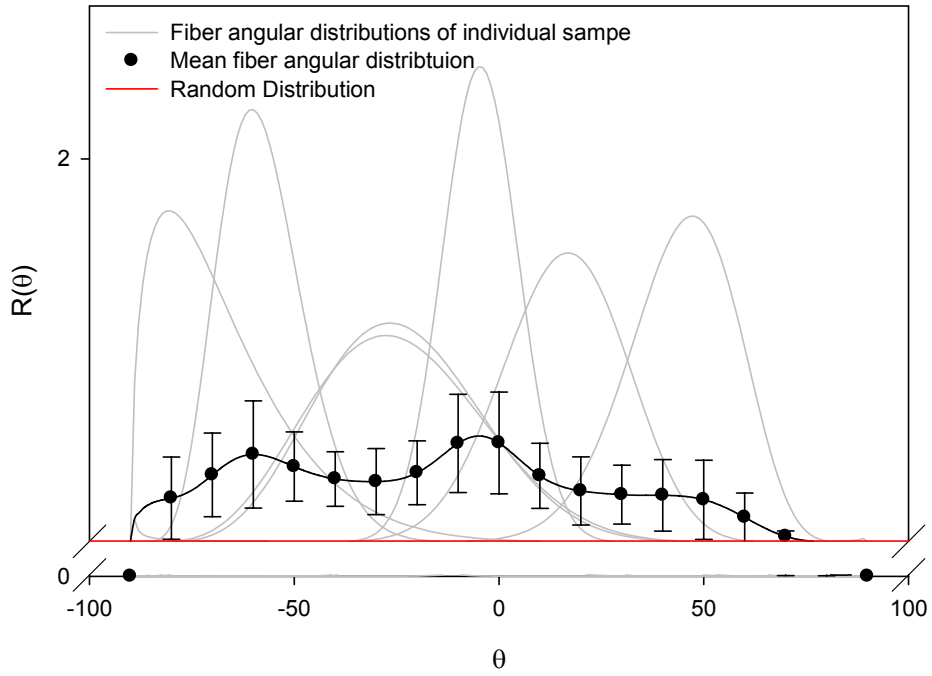

Figure 4-11. Fiber angular distributions from 8 different samples and the mean fiber angular distribution. While on a per specimen basis the FM appears to have fiber alignment, there is a wide variability among the predicted R(θ) parameters (i.e. μ and σ). Thus, when taken as a whole, fiber directions within the FM are random, as evidenced by the "mean" curve. Note, the red line represents a completely random distribution.

To further validate these results, a deeper analysis of the SALS results presented in section 2.3.2 was performed (Figure 4-12). Since R(θ) is calculated from the intensity distribution, I(θ), of a sample through the following equation:

$$R(\theta) = \frac{\bar{I}(\theta)}{\sum_{\theta=-\pi/2}^{\theta=\pi/2} I(\theta)\,\Delta\theta} \qquad (4\text{-}20),$$

I(θ) from various regions within a sample (n=7) were investigated. Additionally, the average I(θ) from the intact FM specimens (n=7) was extracted. From the representative SALS image presented in Figure 4-12a, it can be seen that there is a wide range of degrees of alignment within

the FM. For example, the highly aligned region (1), evidenced by the pink color, contained an I(θ) distribution with tight peaks and possessed a consistent pattern (Figure 4-12). The moderately aligned region (2), identified by the green-yellow region, contained an I(θ) with a consistent pattern, but the peaks are less tight as compared to the aligned region (1) (Figure 4-12a), which means that there more fibers at different angle present. Region (3), or the blue region, was completely random with no consistent pattern in the I(θ) (Figure 4-12a). However, while there appeared to regions of fiber alignment within an FM sample, the average I(θ) from each sample appeared to have a random distribution (Figure 4-12b; grey lines). In order to represent the overall FM alignment, each I(θ) curve for each sample was plotted together and was averaged at each angle, θ, producing a mean I(θ) curve (Figure 4-12b; black dots). This analysis revealed that the overall fiber distribution of the FM is indeed random.

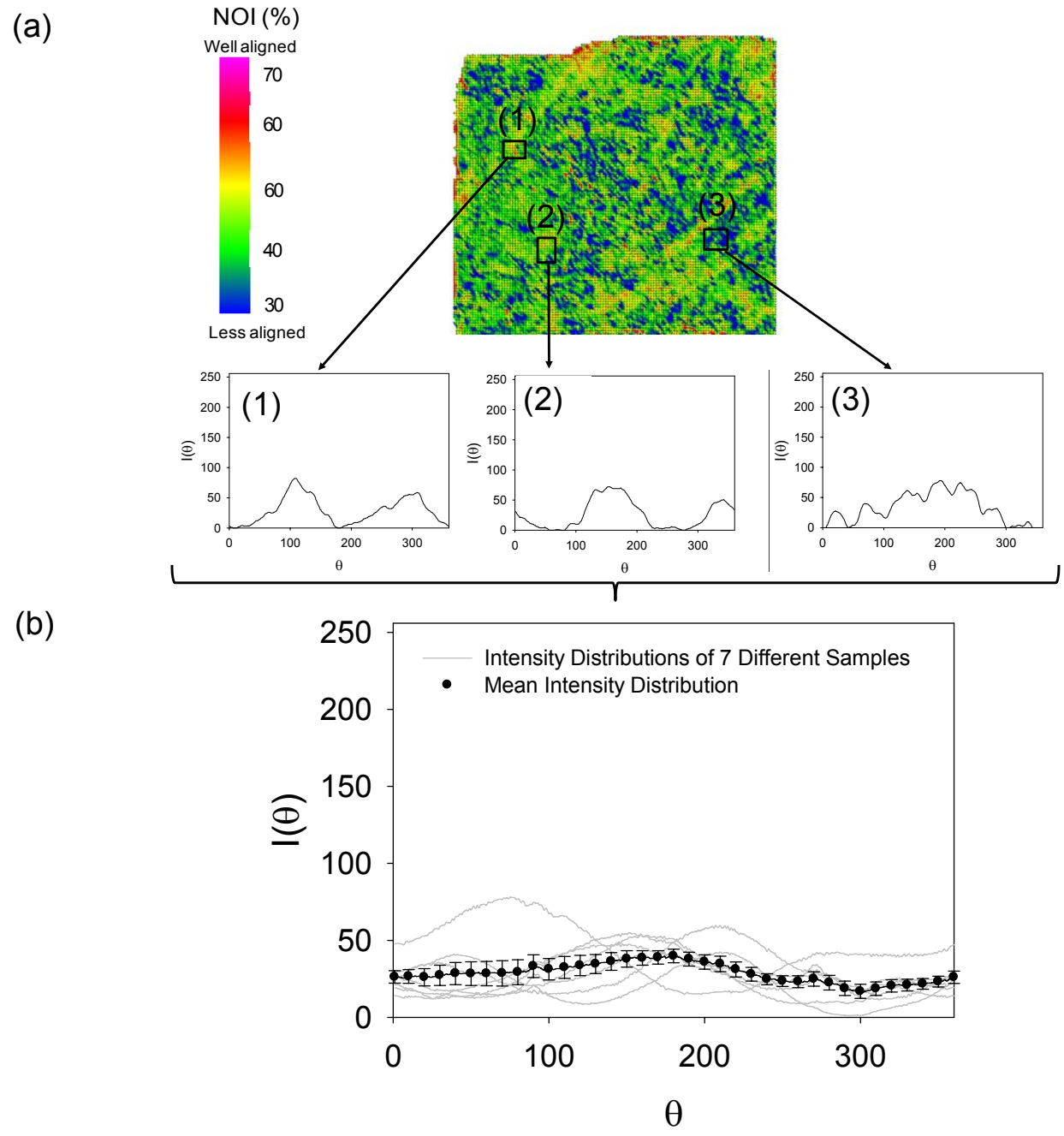

Figure 4-12. (a) In the stress free state, it has been observed that the gross collagen fiber architecture of the FM was not homogenously aligned but did exhibit small regions of fiber alignment. The intensity distribution, I(θ) is an indicator of fiber alignment. For example, the highly aligned region (1) or the pink region, contained an I(θ) with tight peaks and possessed a consistent pattern. The moderately aligned region (2), identified by the green-yellow region, contained an I(θ) with a consistent pattern, but the peaks are less tight as compared to the aligned region (1), which means that there more fibers are present at different angles. Region (3), or the blue region, was completely random with no consistent pattern in the I(θ) curve. Thus, due to the wide variability of I(θ) throughout a single FM sample, the average I(θ) from a single sample demonstrated random alignment. Additionally, the average I(θ) from seven different samples had contained no peaks and no consistent patterns, indicating random fiber alignment.

4.3.3 Model comparisons

The effects of preconditioning became apparent when comparing the fitted ensemble response from the ensemble model and the fitted ensemble response from the tissue level model.

The fitted ensemble response from the fiber ensemble constitutive model was statistically different ($p <= 0.001$) from the fitted ensemble response from the tissue level constitutive model (Figure 4-13), when the post-preconditioned, unloaded reference state was used. The ensemble response generated from the tissue level constitutive model occurs at larger strain values (Figure 4-13a; open circles) as compared to that of the fiber ensemble constitutive model (Figure 4-13a; filled black circles). However, the fitted ensemble response from the fiber ensemble constitutive model was not statistically different ($p = 0.939$) from the fitted ensemble response from the tissue level constitutive model (Figure 4-13b), when the natural, unloaded reference state was used. It was concluded that the most appropriate reference state was the natural, unloaded reference state (section 2.2.4 and section 2.4.1), and when this reference state was used both the fiber ensemble model and the tissue level model predict the same mechanical behavior.

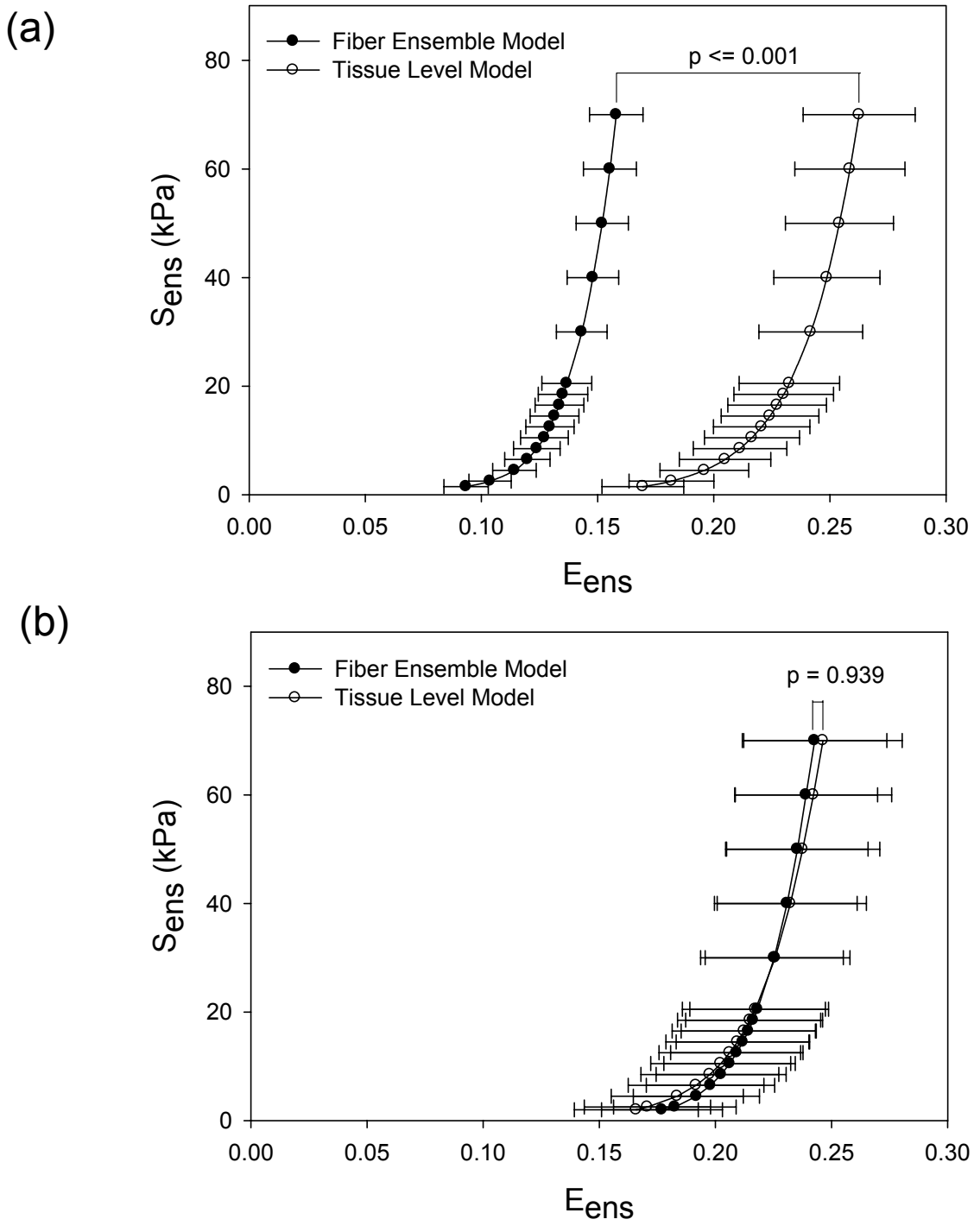

Figure 4-13. Predicted S_{ens}-E_{ens} responses from the fiber ensemble model (filled black circles) and the tissue level model (open circles) when (a) a post-preconditioned reference state was used (p <= 0.001) and (b) when a natural, unloaded reference state was used (p = 0.939).

4.4 DISCUSSION

Recent studies of membrane rupture have been largely pursued from a biochemical and histological perspective, which has provided relevant insights into membrane failure [1]**.** However, an understanding of the biomechanical responses and underlying microstructure of the FM in conjunction with biochemical responses is essential for the development of a rational basis for treatment and prevention of premature failure**.** Once the biomechanical properties are established, we can then better formulate how the biochemical processes modulate failure at full term. Thus, the goal of this study was to build on the results of specific aim 1 by relating the biomechanical response of the intact FM at near/full term under sub-failure loading to the underlying fiber architecture of the intact FM. Establishment of this structure-function relationship is a necessary step towards providing a foundation for future investigation of membrane failure.

4.4.1 Fiber ensemble stress-strain relationship

The fiber ensemble modeling results indicated that FM collagen fibers are rapidly recruited and were straightened well below failure stress levels (Figure 4-7, Figure 4-8, Figure 4-10). The "mean" μ and "mean" σ parameters from the modified beta distributions were 0.91 (i.e. the mean was 0.91*Eub) and 0.08 (i.e. the standard deviation was 0.08*Eub), respectively (Figure 4-9). Since the beta distribution is only defined from 0 to 1, a μ value of 0.91 is relatively high. Thus, a large μ value and a small σ indicate that the collagen fibers were recruited at high strain values, yet once recruitment began, the FM collagen fibers were recruited very rapidly.

These conclusions are further validated by the results presented in Figure 4-8 (i.e. a representative sample). The cumulative fiber distribution illustrated the running total fraction of fibers recruited at any given E_{ens} and demonstrated that gradual recruitment of collagen fibers was followed by a drastic increase in fiber recruitment (Figure 4-8). All collagen fibers were recruited by 0.19 Green's strain. A μ value of 0.92 (0.92*Eub = 0.17) and a small σ value of 0.08 ($0.08*E_{ub} = 0.02$) indicated that collagen recruitment occurred rapidly at large strain values. For example, at 75% of the E_{ub}, only ~5% of the collagen fibers were recruited. Thus, the greatest amount of collagen recruitment occurred in the final 0.1 Green's strain.

4.4.2 Tissue level stress-strain relationship

On a per specimen basis, the tissue level model predicted that the FM contains an aligned fiber architecture evidenced by small σ values for the fiber angular distribution, which is consistent with the reported modest mechanical anisotropy in section 2.3.1 and section 2.4.2. However, upon inspection of Table 4-1, which showed a large variability between the μ parameter, and Figure 4-11, which depicts the mean $R(\theta)$ distribution for all samples tested, the fiber angular distribution of the FM is random, which was also concluded in section 2.4.2. Thus, FM collagen fibers are not aligned globally in relation to any anatomic structures in the uterus or placenta, and the FM is an effectively isotropic material. This finding results in a significant implication on the structure-function relationship of the FM. The isotropic nature of the FM is essential for the accommodation of the bulk loads of the fetus and amniotic fluid as well as toleration of local deformations associated with fetal movement. If the collagen fiber architecture of the FM was

not random and contained a highly oriented collagen network, the FM would only be support load in the direction of the aligned collagen fibers causing the FM to rupture with minimal force.

4.4.3 Limitations

For the planar biaxial experiments, different samples were used for the equi-strain experiments and the multi-protocol experiments. While ideally, one should be able to perform the equi-strain and multiprotocol experiments on the same specimen, the delicate nature of the FM was not amenable to this.

An additional limitation of this study was the unclear physiological relevance of mechanical preconditioning of the FM as previously discussed in section 2.4.3. While preconditioning was necessary to produce repeatable results during planar biaxial testing, its relevance to its *in vivo* state is not clear. It was concluded that the most appropriate reference state was the natural, unloaded reference state because it is the only reference state common among all specimens, and when this is done the results presented herein are comparable with results presented throughout the literature.

4.4.4 Summary and conclusions

This study provided the first data on the effective collagen fiber stiffness of the intact FM from planar biaxial experiments, which was related to the fiber angular distribution of the FM. The results presented clearly demonstrate that the FM collagen fibers are recruited at high strain values, yet once recruitment begins, the FM collagen fibers were recruited rapidly. After the fibers have been fully straightened, they have limited stretching capability thereafter. Also, since

failure did not occur during sub-failure loading, it is apparent that collagen fibers do not begin to fail until all collagen fibers are fully recruited. These results suggest *little or no structural reserve exists in the FM,* which may be an important aspect of it failure properties. Additionally, while on a per specimen basis there appeared to be fiber alignment in the FM, the collagen fibers are not aligned globally in relation to any anatomic structure in the uterus or placenta, and the FM is an effectively isotropic material, which is an essential aspect of the structure-function relationship of the FM. These finding will serve to guide future studies on FM failure properties.

5.0 CHARACTERIZATION OF THE STRUCTURE-STRENGTH SEQUELAE DURING FAILURE IN "NON-WEAK" FM

5.1 INTRODUCTION

Tissue failure is not a normal, physiological event. Bone breakage, skin tears, bowel ruptures are all pathological events which occur as the result of a large force or massive tissue breakdown. The ovarian follicle and some embryological structures do demonstrate tissue failure in the course of normal events, but these are relatively thin and lack the mutilaminar structure of FM. El Khwad *et al.* has shown that the "weak zone" of the FM has an average rupture force of approximately one third that of the rest of the FM [61, 62]. Even weakened in this manner, however, the FM should not precipitously fail, especially prior to the onset of contractions as occurs in all cases of premature rupture of membranes (PROM). One possible explanation for FM failure is the presence of point defects. When individual rupture test points within the "weak zone" are examined, it is clear that rupture strength, even within the "weak zone", is highly variable [61]. This suggests that point-defects may be present in this area of the FM which could serve as rupture initiation sites.

Many investigators have performed *in vitro* biomechanical studies in an effort to understand FM failure [1, 12, 15, 61, 70-78, 126]. Three types of testing apparatuses have been used: (1) tensile testing, in which the membrane is placed between two grips, which are pulled

apart; (2) burst testing, in which a piece of membrane is clamped in a ring and pressure is applied, either via air or fluid, perpendicular to the plane of the membrane; and, (3) puncture testing, in which a spherical metal probe is used to displace the central portion of a membrane, which is clamped in a ring, perpendicular to the plane of its surface [1]. In each mode of testing, the applied force and resulting displacement are measured allowing rupture strength, stiffness, work to rupture, displacement at rupture, displacement at maximum force, and viscoelastic properties of the membranes to be determined. Of these methodologies, tensile testing does not provide a physiological testing environment as the stresses applied are uniaxial. It has been used because standard stress-strain calculations are easy [70, 71]. Burst testing best mimics physiologic loading as it is biaxial and the load is distributed over the entire tissue. However, it is logistically difficult and requires relatively large pieces of membrane. Puncture studies are biaxial with stress applied perpendicular to the membrane as in normal physiology. Puncture tests can also be carried out quickly with small pieces of test membrane. However, puncture test induce a complex stress state in the FM, and a stress "amplification" is induced at the tip of the plunger [102]. Specifically, the stress in the FM is greatest at the tip of the plunger. Calculations using an average stress would cause an underestimation of the failure stresses.

However, a major question remains: What is the effect of mechanical forces – intrauterine stretch and the contractions of labor – on the biomechanical properties of the FM? The majority of investigators failed to study the effect of stretch upon FM biomechanical properties. They focused entirely upon the force required to acutely break the FM (rupture force). Additionally, our understanding of membrane failure is limited because our knowledge is based on tissues either before or after failure. It remains unclear how the amnion layer, which dominates the mechanical response of the FM [12], of the "weak" and "non-weak" FM deforms

with the plunger or pressure head until rupture occurs, limiting our ability to investigate the actual failure process. Thus, the objective of the present study was to accomplish the endpoints of Specific Aim 3: Characterize structural/strength sequelae during failure of the FM in the "non-weak" regions. The micro-structural events that occur during loading and failure of the "non-weak" FM, specifically the amnion layer, will be investigated through the use of a novel device that will be integrated into the SALS system that can perform burst failure tests while simultaneously quantifying the collagen fiber architecture, elucidating how the FM transitions to failure. More specifically, by taking this approach, one can gain insight into how failure initiates in the amnion layer of the FM and how collagen fibers of the amnion layer orient in order to support loading in the "non-weak" amnion layer of the FM. The scientific endpoint of this aim was to quantify collagen fiber structure, such as the preferred fiber directions(s) and the degree of fiber alignment at various loading levels as well as investigating the development of failure in the FM.

5.2 PROTOCOLS

5.2.1 Tissue procurement and preparation

FM specimens were collected from women undergoing Vaginal deliveries at MetroHealth Medical Center, Cleveland Ohio after normal term (37-42 weeks) pregnancies. A CWRU/MetroHealth Medical Center institutional review board (IRB) approved protocol was utilized. FM of patients with clinical chorioamnionitis, meconium, maternal diabetes, or multiple gestations were specifically excluded. For these initial studies, large FM fragments

from regions distant from the "weak zone" as determined by methods previously described were selected [61, 62]. The amnion layer of the FM was then peeled from the choriodecidua layer. The amnion fragments were stored in 1X Minimum Essential Medium and shipped to Pittsburgh, PA overnight on ice. The amnion specimens were tested on the day of receipt.

5.2.2 Small angle light scattering measurements

SALS was used to nondestructively quantify collagen fiber architecture of amnion layer of the FM. A detailed description of the SALS technique has been previously presented[105]. Briefly, a 4 mW HeNe continuous unpolarized laser (λ = 632.8 nm) was passed through the tissue specimen. The spatial intensity distribution of the resulting scattered light represented the sum of all structural information within the light beam envelope. The angular distribution of scattered light pattern, I(Φ), which represents distribution of fiber angles within light beam envelope, was obtained. Quantifiable information based on I(Φ) includes orientation index (OI) and preferred fiber direction. The orientation index (OI) was defined as the angle that contains one half of the total area under the I(Φ) distribution. Normalized orientation index (NOI) was calculated using:

$$NOI = \frac{90^o - OI}{90^o} \quad (5\text{-}1),$$

where NOI ranged from 0% for a complete random network to 100% for a perfectly aligned network [105].

5.2.3 Membrane inflation device design

The membrane inflation test was designed with SolidWorks (Dassault Systemes SolidWorks Corp., Concord MA). The burst device consisted of a two cast acrylic hollow cylinders, which contained a 1.27cm wall thickness, (Figure 5-1; parts a and c). Cylinder 1 and 2 were attached to clamping plate 1 (Figure 5-1; part b) and 2 (Figure 5-1; part d), respectively. Each clamping plate was 1.1 cm thick. Each cylinder contained a cast acrylic clear window (Figure 5-1; part e) at each end in order to permit the laser beam of the SALS device (Figure 5-1; part f) to pass through cylinders 1 and 2. Cylinder 1 acted as a pressurization chamber (Figure 5-1; part a), and cylinder 2 (Figure 5-1; part c) was exposed to atmospheric pressure via a groove in the top of the cylinder, which permitted natural membrane deformation. Additionally, the groove in cylinder 2 (Figure 5-1; part a) allowed for direct measurement of membrane displacement. Cylinder 1 (Figure 5-1; part b) contained two access ports. One port was connected to a three-way stop-cock. One opening of the stop-cock was connected the cylinder; a syringe was connected to second opening of the stop-cock, which was used to pressurize the membrane; and a blood pressure transducer (BLPR2) with an operating range between -50 to +300 mmHg (Sarasota, FL) was connected to the third opening of the stop-cock to monitor the pressure within cylinder 1 during testing. The second port acted as a bleed valve to release all air from within cylinder 1.

Each clamping plate (Figure 5-1; parts b and d) contained a hole directly in the center of the plate, 3 cm in diameter. Clamping plate 1 (Figure 5-1; part b) contained a series of 2 grooves, and clamping plate 2 (Figure 5-1; part f) contained a series of 2 protruding ridges. Thus, the 2 protruding ridges of clamping plate 2 (Figure 5-1; part f) mated with the 2 grooves of clamping plate 1 (Figure 5-1; part b), which served to align the clamping plates as well as hold the amnion layer in place. In addition to the groove and ridges, clamping plate 1 (Figure 5-1;

part b) and clamping plate 2 (Figure 5-1, part d) contained o-ring grooves, with an inner diameter of 4.13 cm and an outer diameter of 4.76 cm, which were machined outside of the ridges and grooves. O-rings were placed in each groove in order to grip the membrane as wells as serving as a seal to the atmosphere. Finally, clamping plate 2 (Figure 5-1; part d) contained an additional o-ring groove, with an inner diameter of 13.02 cm and an outer diameter of 13.65 cm, machined outside of the grooves and ridges and the first o-ring grooves. An o-ring placed in the outer groove of clamping plate 2 (Figure 5-1; part d) and mated with a smoothed machined surface on clamping plate 1 (Figure 5-1; part b). This additional o-ring simply served as a seal to prevent fluid from leaking of the burst device and did not grip tissue. The device was then placed in a cradle, which could be secured inside the SALS device during testing (Figure 5-1; part h). The clamping plates also contained 14 screw holes, 0.62 cm (i.e. a 10-32 screw was used) in diameter, which served to screw the two clamping plates together. See Appendix A for complete technical drawings. Also, room temperature PBS (pH 7.4) was used to pressurize the membrane. Thus, in order to verify that PBS and the cast acrylic windows (Figure 5-1; part e) did not cause laser (Figure 5-1; part f) distortion leading to inaccurate structural measurements, a validation study was completed, and it was concluded that the device filled with PBS did not distort the laser beam of the SALS device (Appendix A).

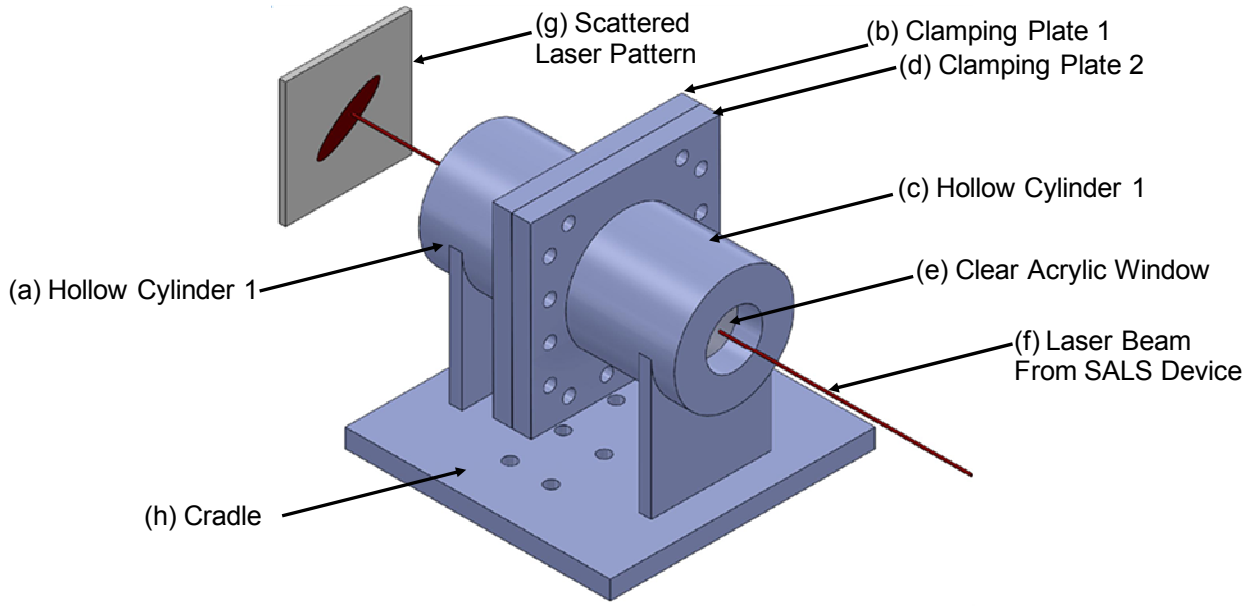

Figure 5-1. Solid model of membrane inflation device. The device consisted of (a,c) two hollow cylinders, (b,d) two clamping plates, (e) two clear acrylic window so that the (f) laser beam of the SALS can pass through the membrane inflation device to the (g) screen of the SALS device, and (h) a cradle that is mounted in the SALS device and supports the membrane inflation device.

5.2.4 Membrane inflation study testing protocols

Upon receipt of the amnion layer of the FM, the amnion was first cut into a circular shape approximately 10-13 cm in diameter. This ensured that the sample was large enough to be griped between the first set of o-ring groove discussed in section 5.2.3, yet small enough to not interfere with the additional outer o-ring also discussed in section 5.2.3. Next, cylinder 2 attached to clamping plate 2 was filled with PBS (pH 7.4) at room temperature (Figure 5-2). Then, cylinder 1 attached to clamping plate 1 was fastened to clamping plate 2 (Figure 5-2). Finally, cylinder 1 was filled with PBS, and the devices was placed in its cradle and secured in the SALS device (Figure 5-3). Next, a 1 cm x 1 cm square section was scanned with the SALS

device at the following pressures: 0 mmHg, 5 mmHg, 20 mmHg, 50 mmHg, 80 mmHg, 100 mmHg, after which the pressure was incrementally increased 10mmHg until membrane rupture. A 1cm x 1cm area was chosen in order to reduce test time and pilot studies verified that SALS results within the 1 cm x 1 cm area in the center of the pressurized membrane would not be affected by the curvature of the membrane under pressure. PBS was used to pressurize the membrane via a syringe. At each pressure level, the displacement of the center the inflated amnion was measured and recorded.

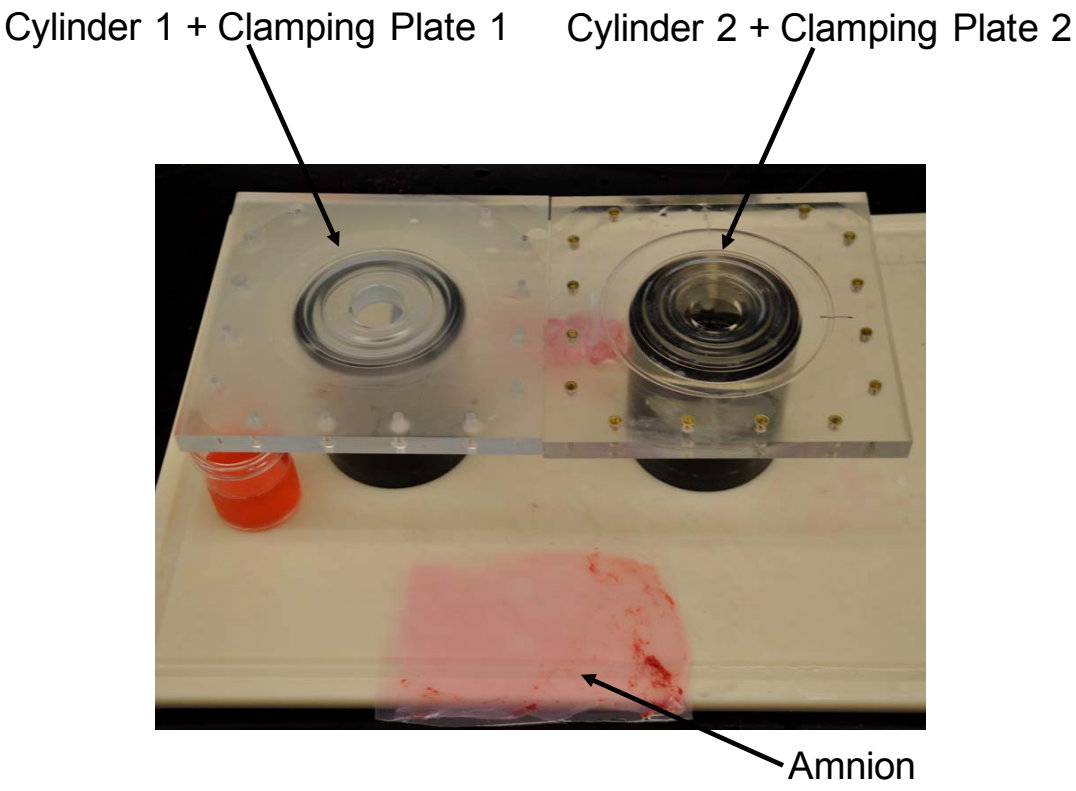

Figure 5-2. Photograph of the membrane inflation device during experimental set-up.

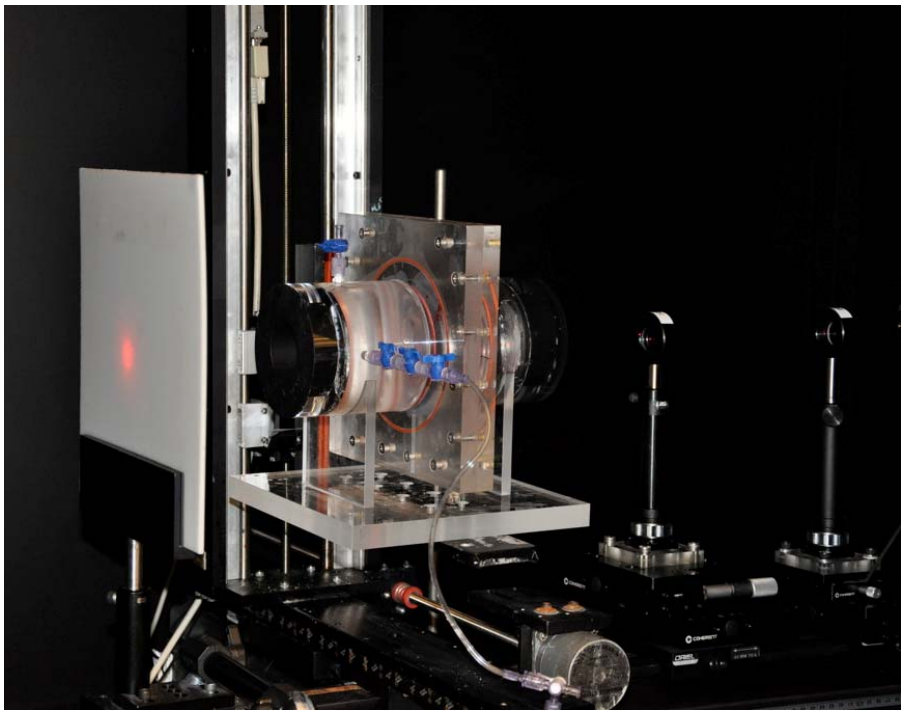

Figure 5-3. Image of the membrane inflation device mounted in the SALS device.

5.2.5 Analysis of membrane deformation

In order to ensure that the amnion was deforming homogenously, validation studies were performed first performed on latex, an assumed isotropic material, and then on the amnion layer of the FM (Appendix A). It was concluded from the validation studies that both the latex material and the amnion deformed homogenously. Thus, assumptions about the deformation of the amnion during burst testing can be made. Due to the geometry of the burst device and the homogenously deformed amnion (Figure 5-4), the same deformation assumption utilized in the analysis of cells during micropipette aspiration was exploited. Specifically, since the clamping plate thickness was 1.1 cm (Figure 5-4), and the amnion layer did not displace past 1.8-2.0 cm

(Figure 5-4), the burst device was treated as a large micropipette (Figure 5-5). In micropipette analysis, it is assumed that the equilibrium shapes of an aspirated cell or in this case the amnion are composed of spherical and cylindrical parts (Figure 5-5) [127]. In the case of a cell, as aspiration proceeds, the cell projection into the pipette grows, where the radius of the pipette is R_1, the radius of the spherical part of the cell in the pipette is R_2, the projection length of the cell is L (Figure 5-5a) [127]. However, when the $L \geq R_1$, the projection length continues to increase as a cylinder with a hemispherical cap with the same radius as the pipette, R_1 (Figure 5-5a) [127]. This same approach will be applied to the amnion during the membrane inflation studies, where R_1 is 1.5 cm (i.e. the diameter of the fixture opening) and L is the measured displacement of the center the inflated amnion (Figure 5-5b). However, when $L < R_1$, the geometry of the amnion will be treated as an oblate spheroid, such that the radius of the amnion, R_2, is less than R_1 (Figure 5-5b).

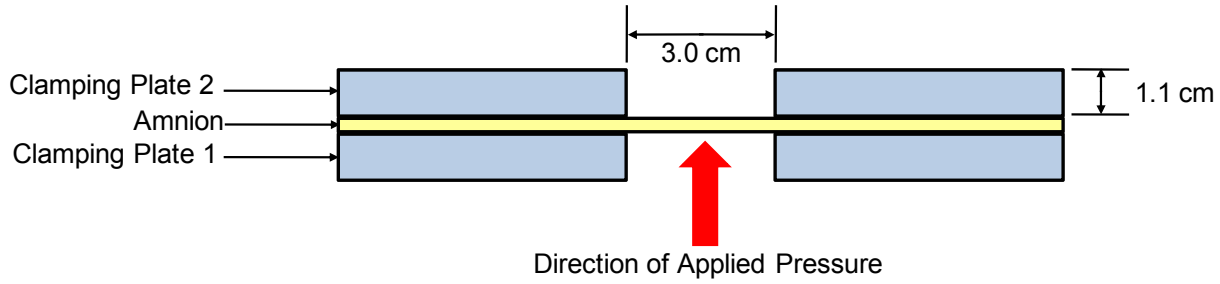

Figure 5-4. Schematic of amnion placed between the clamping plates of the membrane inflation device. The thickness of the clamping plate is 1.1 cm and contains a hole in the center that is 3.0 cm in diameter.

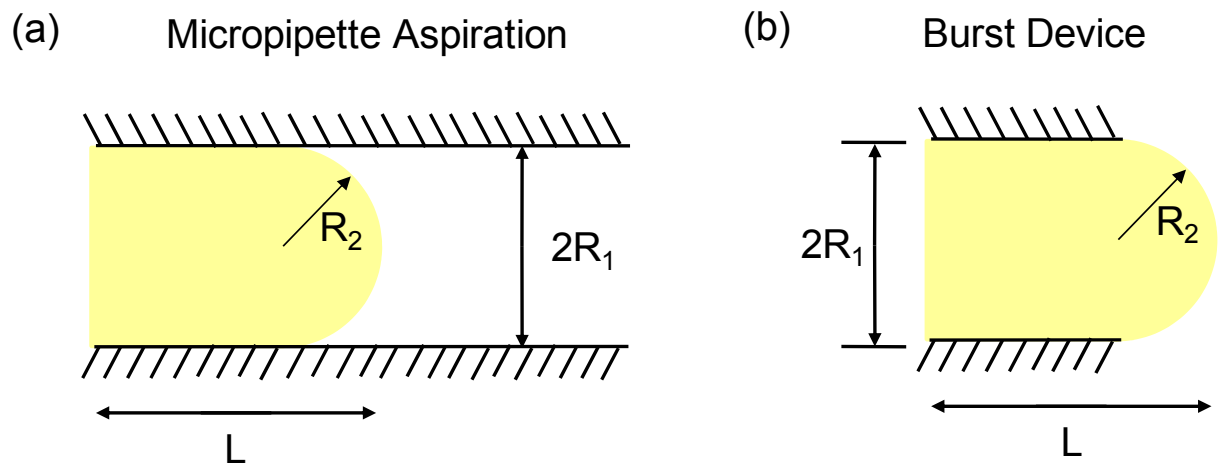

Figure 5-5. Schematic of (a) a cell inside a micropipette and (b) a pressurized membrane in the membrane inflation device. It is important to note the similar geometries between the experimental devices as well as between an aspirated cell and an inflated membrane. The equilibrium shape of an aspirated cell is composed of spherical and cylindrical parts. R1 is the diameter of (a) the micropipette or (b) the hole in the center of the clamping plate. R2 is the radius (a) spherical part of the cell in the pipette or (b) spherical part of the amnion. L is the projection length of the (a) cell into the micropipette or (b) amnion into the inflation device. When $L \geq R1$, the projection length of the cell or amnion increases with a hemispherical cap with a radius R1. In the case when $L < R1$, the geometry of the amnion will be modeled as an oblate spheroid.

In order to quantify the amount of stretch that the FM undergoes, areal stretch was calculated by dividing the surface area of the membrane prior to rupture by the initial unloaded surface area. Also, the surface area at each pressure level was calculated, and the areal stretch at each pressure level was evaluated. The surface areas were calculated based on the geometries discussed above (i.e. spheres and cylinders).

5.2.6 Stress analysis of the membrane

As per the validation studies presented in Appendix A, the deformation of the amnion during the burst studies is considered axisymmetric, meaning that the undeformed and deformed configurations of the amnion can be describe by generator equations that are revolved about a

common axis and the applied loads are independent of the angle through which the generated curves are rotated [128]. Figure 5-6 depicts an axisymetric membrane in its deformed configuration, which is denoted by a generator curve relative to the r and z coordinates. The principal curvatures are defined as:

$$\kappa_1 = \frac{d\phi}{ds} = \frac{d\phi}{dr_1}\frac{dr_1}{ds} \text{ and } \kappa_2 = \frac{1}{r_2} \tag{5-2}$$

Additionally from the geometry,

$$\cos\phi = \frac{dr_1}{ds} \text{ and } \sin\phi = -\frac{dz}{ds} \tag{5-3}$$

Substituting equation (5-3) into equation (5-2) result in the two principal curvatures:

$$\kappa_1 = \cos\phi\frac{d\phi}{dr_1} \text{ and } \kappa_2 = \frac{1}{r_2} = \frac{\sin\phi}{r_1} \tag{5-4}$$

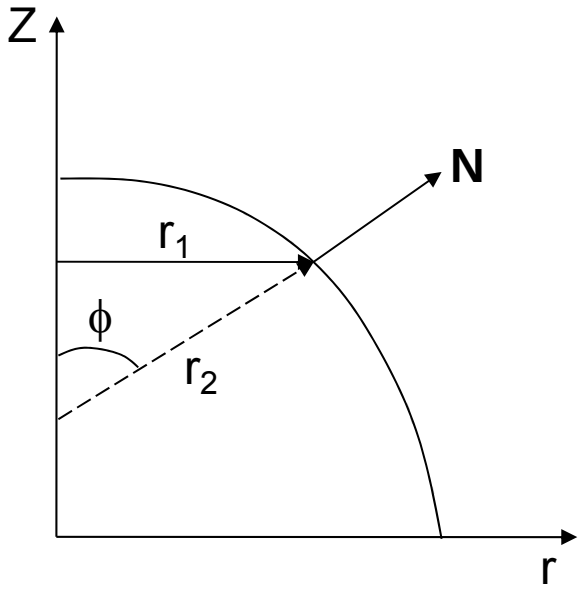

Figure 5-6. Schematic of a deformed axisymetric membrane relative to cylindrical coordinates, r and z. ϕ is defined as the change in orientation of the outward normal vector N as a function of arc length, s.

Finally, the equilibrium equations for an axisymetrically deformed membrane based on the principal curvatures presented in equation (5-4), can be defined as:

$$T_1 = \frac{P}{2\,\kappa_2} \text{ and } T_2 = \frac{P}{\kappa_2}\left(1 - \frac{\kappa_1}{2\kappa_2}\right) \tag{5-5}$$

where T_1 and T_2 are the meridional and circumferential (Figure 5-7) stress resultants, respectively, and P is the distension pressure.

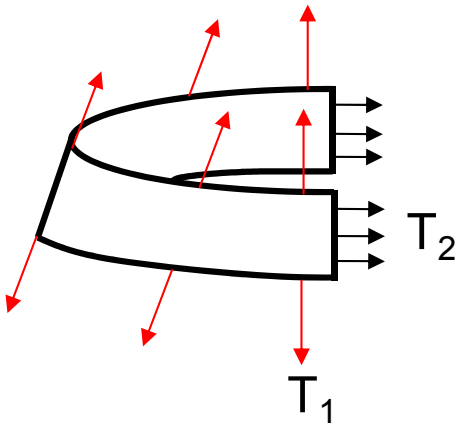

Figure 5-7. Free body diagrams of the meridional stress resultant (T_1, red arrows) and the circumferential stress resultant (T_2, black arrows) for an axisymmetric membrane.

An inflated elliptical membrane is special equilibrium case from equation (5-5). In this special case, an elliptical membrane remains in an elliptical configuration in both its reference and deformed configuration. The principal stress resultants for an inflated elliptical membrane can be defined as:

$$T_1 = \frac{Pa^2}{2(a^2\sin^2\phi + b^2\cos^2\phi)^{1/2}} \text{ and } T_2 = \frac{Pa^2}{(a^2\sin^2\phi + b^2\cos^2\phi)^{1/2}}\left(1 - \frac{a^2\sin^2\phi + b^2\cos^2\phi}{2b^2}\right) \tag{5-6},$$

where a and b are the deformed principal radii. When a = b, equation (5-5) reduces to the results for an inflated spherical membrane. Thus, when the projection length L is less than 1.5 cm (i.e. R_1 in Figure 5-5b) equation (5-5) will be employed. However, when $L \geq R_1$, equation (5-5) reduces to

$$T_1 = T_2 = \frac{Pa}{2} \qquad (5\text{-}7),$$

as in the case of micropipette aspiration.

5.2.7 Statistical analysis

When a mean value was presented, the standard error of the mean (SEM) was also presented. A one way repeated measures ANOVA was used to evaluate the differences between the NOI and preferred fiber directions at each pressure level. However, statistics were only performed on pressure levels up to 120 mmHg because only two samples ruptured at higher pressure values resulting in a small sample size. Differences were considered statistically significant when $p>0.05$.

5.3 RESULTS

5.3.1 Membrane inflation – microstructural characteristics

The collagen fiber alignment of the amnion in the unloaded, stress free state (0 mmHg) was considered random with an average NOI value of 40.16 ± 1.31 (Figure 5-8a). With increased pressure, there was a slight increase in the NOI values up to 100 mmHg with no change

thereafter (Figure 5-8), but this change was not considered statistically significant ($p = 0.315$). This phenomenon was also demonstrated through histograms of the average NOI values at various pressure levels (Figure 5-8b). It was established that the average NOI distribution continued to shift to the right with increased pressure indicating an increase in fiber alignment, but after 100 mmHg, the curve did not shift any further to the right, indicating that there was no change in fiber alignment thereafter (Figure 5-8b). It is important to note that the error bars were not presented in Figure 5-9 because the large error bars made the graph illegible. In order to gain a better understanding of how amnion fiber architecture adapts to increasing pressure, the rate of fiber alignment at each pressure level was computed (Figure 5-9). The largest change occurred at the 0-5 mmHg level, with minimal rates of change thereafter.

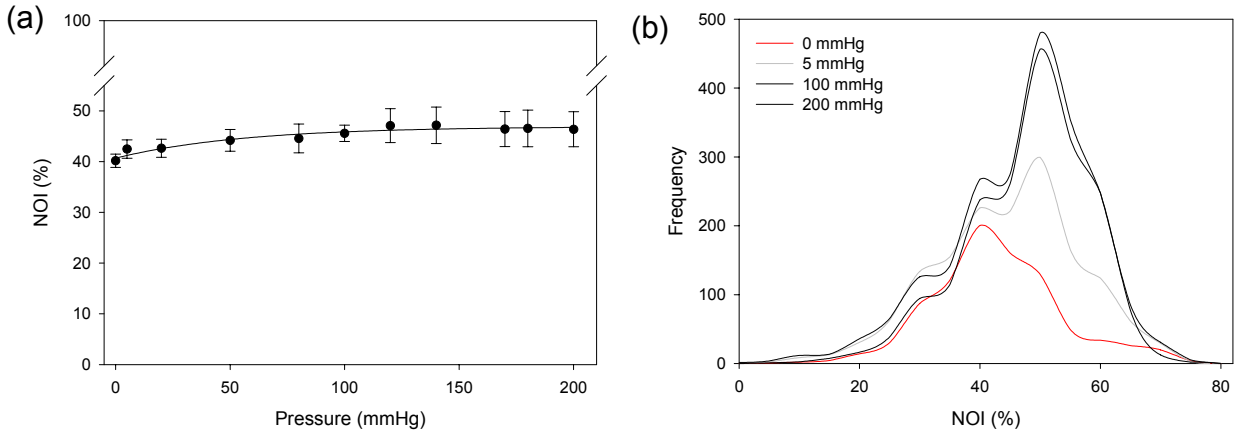

Figure 5-8. (a) The NOI increase with increased pressure, with the greatest change in NOI occurs under the first 5 mmHg. NOI continually increases with pressure up to 100 mmHg, with minimal change thereafter. It is important to note that these changes were not considered statistically significant. (b) This behavior can also be represented by histograms. When pressure is increased to 5 mmHg, the Frequency-NOI curve shift to the right indicating an increase in NOI values (grey line). The Frequency-NOI curves continue to shift to the right with increased pressure up to 100 mmHg (black line), with no subsequent changes.

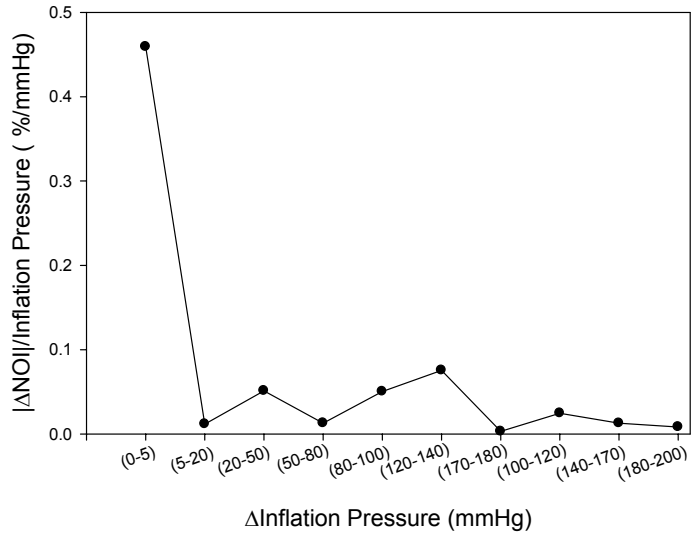

Figure 5-9. The largest rate of change in NOI change occurred at the 0-5 mmHg level, with and minimal rates of change past 5 mmHg.

Finally, the preferred direction of the collagen fibers did not change under loading ($p = 0.0598$) (Figure 5-10).

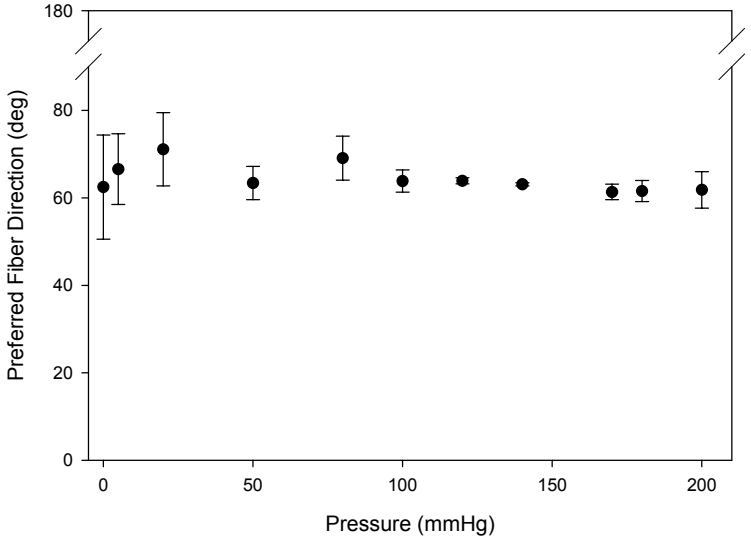

Figure 5-10. There were no changes in the preferred fiber direction under loading.

A representative image, Figure 5-11, depicts the microstructural changes that occur in the amnion under pressure. In the stress-free state (0 mmHg), the amnion was not homogenously aligned, while it did exhibit small regions of fiber alignment. However, with increased pressure, the amnion layer did exhibit a slight increase in fiber alignment as well as a minor change in the preferred fiber direction (Figure 5-11). The greatest amount of change in fiber alignment occurred between 0 mmHg and 5 mmHg, with a slight increase in NOI values from 5 mmHg to 100 mmHg (Figure 5-11), and there was no change in fiber orientation thereafter. Additionally, there was a small increasing trend in fiber direction. Rupture occurred at 120 mmHg. As previously discussed in section 1.4.3, it was anticipated that with increased pressure the collagen fibers of the amnion would uncrimp and straighten causing an increase NOI values. However, it was unclear how the amnion layer of the FM failed, catastrophically (Figure 5-11; scenario 1) or as a result of point defects (Figure 5-11; scenario 2). It has become evident that that the amnion layer of the FM fails catastrophically because no point defects were detected (Figure 5-11; 100 mmHg) prior to failure (Figure 5-11; 120 mmHg), as in scenario 1. Thus, the collagen fibers first began to uncrimp with increased loading. As pressure is increased, the fibers became fully straightened, and the fibers remained taught until failure occurred, at which point all fibers failed at once.

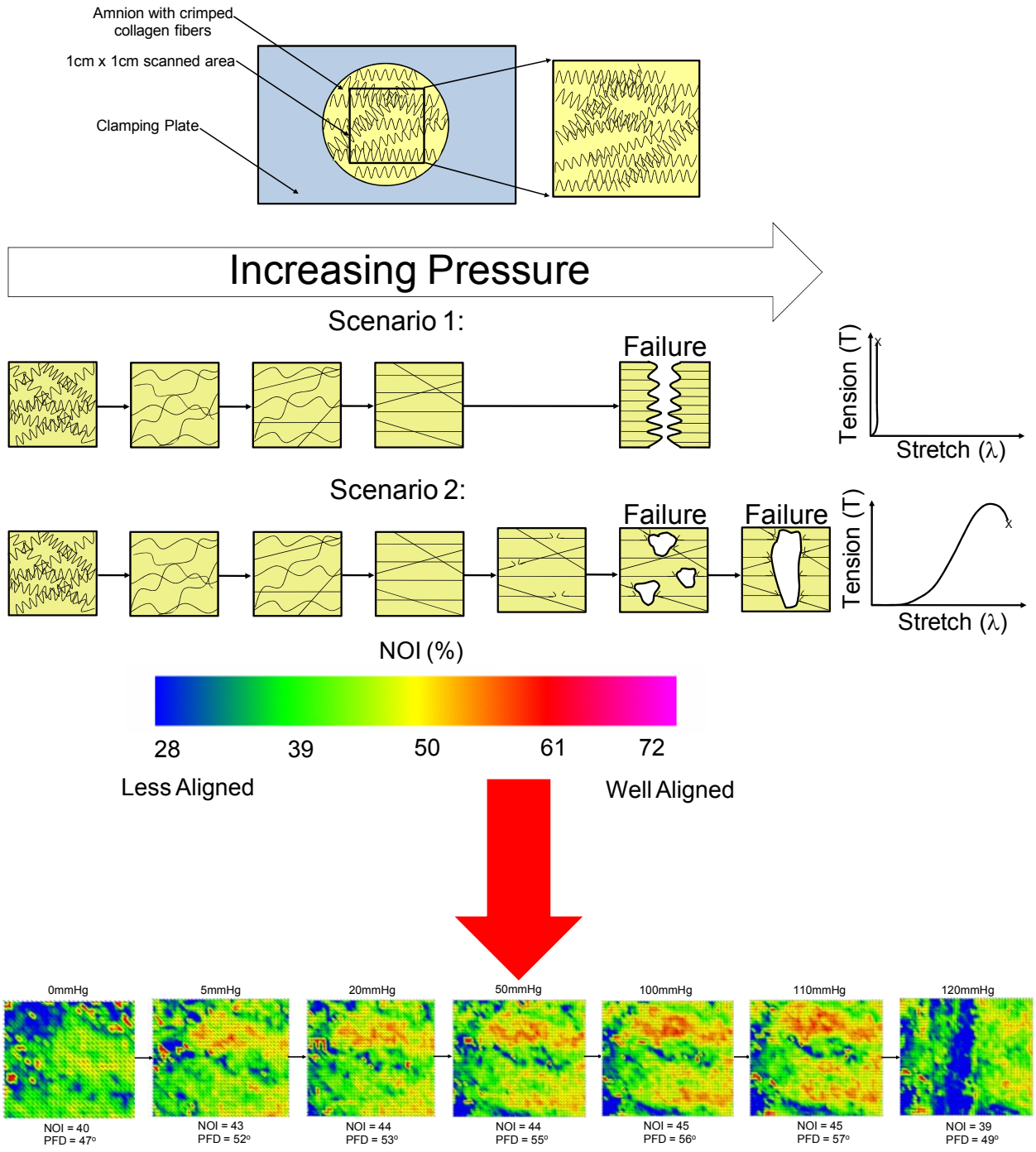

Figure 5-11. Representative image of the microstructural changes that occur in the amnion layer of the FM under isotropic loading. NOI values preferred directions (PFD) increased with increased pressure. However these changes were not found to be statistically significant. Since the change in preferred direction was not significant, the increase in fiber alignment was likely due to the uncrimping of the collagen fibers. Most importantly, failure of the amnion layer was found to be catastrophic. Point defects did not appear in the tissue leading up to failure. Failure of the amnion layer of the FM can therefore be characterized by scenario 1. Hence, the collagen fibers initially uncrimped, with minimal fiber rotation under loading until all fibers failed at once.

5.3.2 Membrane deformation and failure

A summary of the rupture pressures can be found in Table 5-1.

Table 5-1. Summary of rupture pressures for each specimen.

Sample	Rupture Pressure (mmHg)
1	93.70
2	214.06
3	105.79
4	150.66
5	116.34
6	246.50
mean ± SEM	**154.50 ± 25.53**

The average calculated areal stretch of the FM was presented for 5 mmHg, 20 mmHg, and the areal stretch prior to rupture (Table 5-2). It is assumed that 10 mmHg is the *in vivo* pressure at term gestation [106]. Thus, 5 mmHg and 20 mmHg were presented to provide a range of stretch values close to the assumed *in vivo* pressure. The average areal stretch at 5 mmHg, 20 mmHg, and prior to failure are 1.79 ± 0.18, 2.11 ± 0.09 and 2.51 ± 0.05, respectively. Additionally, the greatest change in areal stretch with increased pressure occurred between 0 mmHg and 5 mmHg, with little change after 20 mmHg (Figure 5-12). Note that 5 mmHg corresponds to approximately 5 N/m and 20 mmHg corresponds to approximately 20 N/m. Approximately is

used because there is a slight variation in the tension level over the surface of the amnion at 5 mmHg and 20 mmHg, which can be seen in Figure 5-13. This is further discussed below.

Table 5-2. Summary of areal stretch values at physiological loading, 5 mmHg, 20 mmHg, and the areal stretch value prior to membrane rupture. Each stretch is referenced to the unloaded configuration.

Sample	Areal Stretch at 5 mmHg	Areal Stretch at 20 mmHg	Areal Stretch at Rupture
1	2.23	2.32	2.54
2	1.78	2.05	2.59
3	1.12	2.09	2.41
4	1.74	1.78	2.32
5	1.82	2.02	2.55
6	2.05	2.32	2.63
mean ± SEM	**1.79 ± 0.18**	**2.11 ± 0.09**	**2.51 ± 0. 05**

However, pilot studies concluded that separation of the amnion from the choriodecidua caused the amnion to deform (Appendix B). The deformation associated with separation was as follows:

$$F = \begin{bmatrix} 1.041 \pm 0.021 & 0.044 \pm 0.026 \\ 0.023 \pm 0.026 & 1.035 \pm 0.029 \end{bmatrix}$$

Thus, the values presented in Table 5-2 are re-presented in Table 5-3 to account for the deformation associated with membrane separation:

Table 5-3. Summary of corrected areal stretch values at physiological loading, 10 mmHg, and areal stretch values prior to membrane rupture. These values account for the deformation associated with membrane separation. Each stretch is referenced to the unloaded configuration.

Sample	Areal Stretch at 5 mmHg	Average Stretch at 20 mmHg	Areal Stretch at Rupture
1	2.40	2.49	2.74
2	1.92	2.20	2.78
3	1.21	2.25	2.59
4	1.87	1.92	2.49
5	1.96	2.18	2.75
6	2.20	2.49	2.83
mean ± SEM	**1.93 ± 0.17**	**2.26 ± 0.09**	**2.69 ± 0.05**

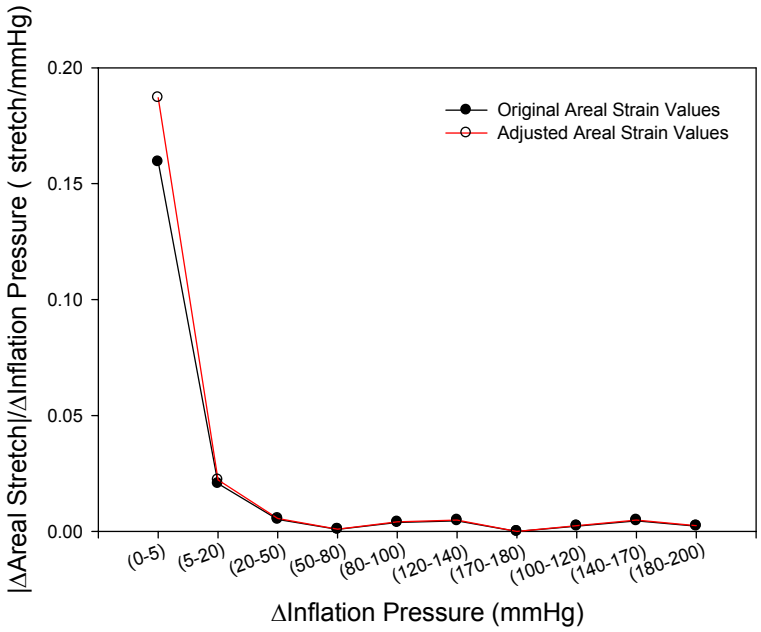

Figure 5-12. The greatest change in areal stretch in the amnion layer of the FM was between 0 mmHg and 5 mmHg with minimal change after 20 mmHg.

For pressures equal to or less than 20 mmHg, the projection length, L, of the amnion was less than R_1 and the average meridional membrane tension and the average circumferential membrane tension (T_1 and T_2, respectively) varied over the surface of the membrane, with the greatest tension at the top of the membrane (Figure 5-13). Note that ϕ goes from 0^o to 90^o. However, once $L \geq R_1$ (i.e. pressures greater than 20 mmHg), the membrane average tensions became uniform over the surface of the membrane, and increased tension simply resulted in an upwords shift in the T_1-Pressure and T_2-Pressure curves (Figure 5-13).

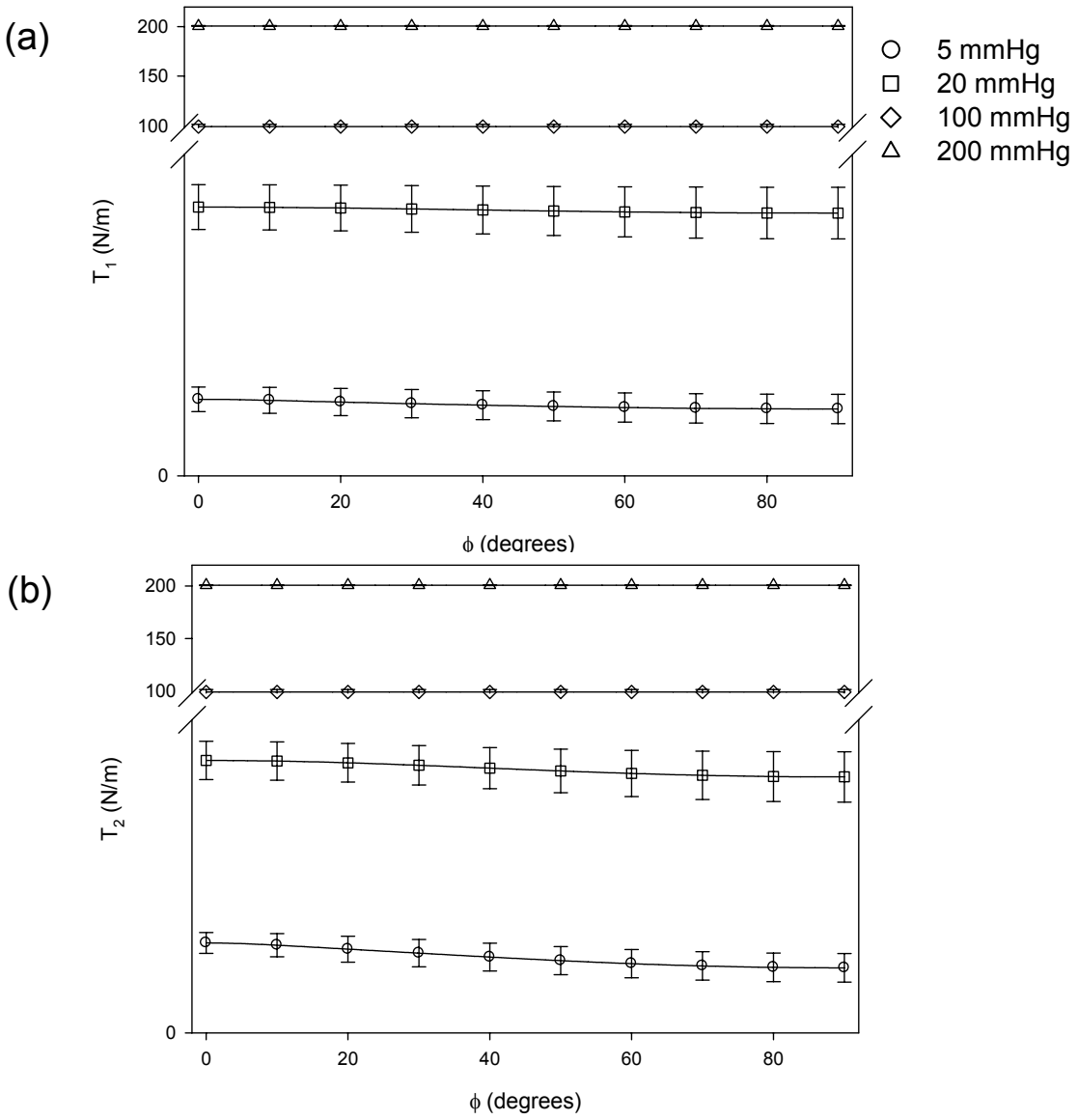

Figure 5-13. (a) The meridional membrane tension, T1, and (b) the average circumferential membrane tension, T2, at each pressure level. Note that at lower pressure levels, 5 to 20 mmHg, the T1 and T2 varies over the surface of the membrane. However, when $L \geq R_1$, the amnion deforms into a spherical geometry and the tensions become uniform.

Finally, the average areal strain at each average tension level was plotted, and it can be seen that an *in vivo* areal stretch of 2.56 ± 0.08 (section 3.3) corresponds to a tension level of 103 N/m (Figure 5-14).

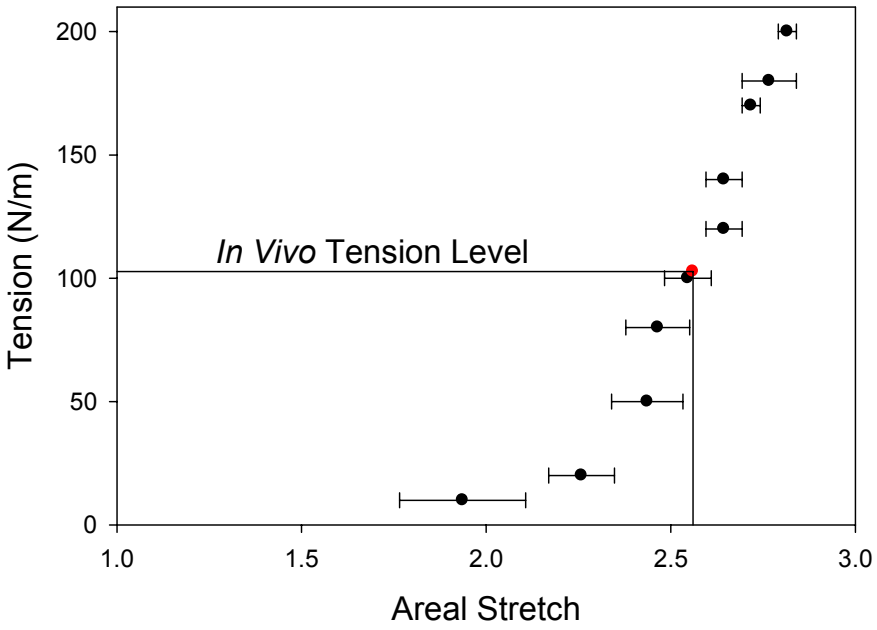

Figure 5-14. The in vivo deformation determined in section 3.3 was 2.56 ± 0.08, which corresponds to an in vivo pressure of 10 mmHg [106]. Thus, an areal stretch value of 2.56 corresponds to a tension value of 103 N/m.

5.4 DISCUSSION

One of the limitations of our current understanding of FM failure is that our knowledge is based on tissues either before or after failure. Prior to this study, it was unclear how the amnion layer of the non-weak FM will be deformed during membrane inflation studies, preventing investigation of the actual failure process. Using the developed novel device, we were be able to

gain insight into the FM failure process, including whether failure is catastrophic or initiates as small defects leading to complete failure. In this approach the amnion alone was investigated because it is known to dominate the mechanical response to the intact FM, with both stiffness and strength an order of magnitude greater than the choriondecidua layer [15]. Moreover, by performing this membrane inflation test, one was able to investigate how the collagen fibers of the amnion layer orient in order to support loading in the non weak amnion. Understanding the differences in the underlying microstructure of the non-weak FM is a key piece of information needed to fully understand how the FM fails and is the first step towards understanding how the structure-function relationship of the FM is altered in weakened FM.

5.4.1 Microstructural characteristics and implications

It was established that there is an increase in collagen fiber alignment with increased loading, although not significant ($p = 0.315$), which was likely due to the uncrimping of the collagen fibers and not large fiber rotations, since there was not a significant change in the preferred fiber direction with increased loading ($p = 0.598$) (Figure 5-8 and Figure 5-10). Moreover, the greatest change in fiber alignment occurred in the first 5mmHg of pressure, followed by a minor increase in fiber alignment up to 100 mmHg, with no change thereafter (Figure 5-9). These microstructural findings corroborate the mechanical findings presented in section 2.3.1 and section 2.3.2 as well as in section 4.3.1 and section 4.3.2, in that once the FM were loaded, the FM collagen fibers were recruited rapidly. Also, these findings suggest that the collagen fibers of the amnion layer remains heterogeneously aligned under isotropic loading, meaning that the collagen fibers were not strongly aligned in a preferred direction even when loaded, which can also been seen in Figure 5-11. Thus, the amnion can continue to accommodate the bulk loads of

the fetus and amniotic fluid as well as toleration of local deformations associated with fetal movement even in the loaded state. If the collagen fibers rotated into a preferred direction under loading, the FM would only be support load in the direction of the aligned collagen fibers causing the FM to rupture with minimal force.

5.4.2 Membrane deformation

It was established that the average maximum areal stretch of the amnion prior to failure was 2.51 ± 0.05, and areal stretch values at 5 mmHg and 20 mmHg were 1.79 ± 0.18 and 2.11 ± 0.09, respectively (Table 5-2). While there was variability among specimens in the rupture pressure (Table 5-1), the amount of deformation prior to failure was consistent. Each membrane stretched ~2.5 regardless of the rupture pressure. However, separation of the amnion layer and the choriodecidua layer resulted in a slight deformation of the amnion layer. Thus, when this deformation was accounted for, stretches at 5 mmHg and 20 mmHg were 1.93 ± 0.17 and 2.26 ± 0.09, respectively, with a stretch prior to rupture of 2.69 ± 0.05.

These values can be compared to the *in vivo* stretch measures presented in section 3.3. The maximum *in vivo* areal stretch estimated in section 3.3 was 2.56 ± 0.08, which is assumed to correlate to an intrauterine pressure of 10 mmHg. It is important to note that the *in vivo* deformation measurements performed in section 3.3 were completed on repeat Cesarean Section patients. Thus, these patients delivered approximately 2 weeks prior to the estimated term delivery date, and thus, the MRIs performed on these patients were also 2 weeks prior to the estimated delivery date. In consequence, these stretch measurements may be lower had these patients delivered at term, and the fetus grew for 2 more weeks. Upon comparing the areal stretch value of 2.56 (*in vivo* study) with the value of average maximum stretch value of 2.69

(membrane inflation), this phenomenon is evident. These results suggest that had the fetus remained in the uterus until term, the membrane likely would have stretched more. Finally, an *in vivo* tension value of 2.56 corresponded to a tension value of 103 N/m (Figure 5-14).

This results can be justified by the planar biaxial testing result found in section 2.3.1, Table 2-1, where the estimated upper bound tension level (T_{ub}) from the planar biaxial studies was found to be 25.62 ± 1.69 N/m. Note that the corresponding upper bound areal strain was found to be 0.59 ± 0.03 (corresponds to an areal stretch value of 1.59) (Table 2-1). However, the samples used for planar biaxial testing were preconditioned, causing these specimens to attain a different equilibrium state, resulting in a stiffer mechanical response. As discussed in the sections 2.2.4, 2.4.1, 2.4.3, and 4.4.3, preconditioning allowed for accurate and repeatable test results, and the mechanism of preconditioning and the relation between a preconditioned tissue's response and its actual *in vivo* properties is not clear. Thus, while the exact stretch values between the membrane inflation studies and the planar biaxial studies were not the same, the estimated upper bound tension levels were approximately the same (25.62 ± 1.69 N/m for the planar biaxial studies (Table 2-1) and ~20 N/m for the membrane inflation studies (Figure 5-12)). Additionally, since preconditioning was not performed during the membrane inflation studies, the areal stretch values were more comparable to the *in vivo* areal stretch values. In conclusion, the FM, or the amnion in this case, is loaded up to approximately its upper bound stretch value until labor occurs.

5.4.3 Membrane failure

As discussed previously, it was unclear how failure arises in the FM. One of the main goals of this study was to determine if failure is catastrophic or initiates as small defects leading to

complete failure (Figure 5-11). Through this study, it was established that failure at the fiber lever occured as a result of catastrophic failure. This finding suggests that no fibers are predisposed towards failure, meaning that no fiber is weaker than another fiber prior to biochemical weakening. This result provides a basis for establishing how the structure-function relationship of the FM is altered the "weak zone," which has unique mechanical properties that facilitates membrane rupture. It is likely that proteolytic enzymes, specifically MMP-2 and MMP-9, play a role in the weakening of the FM, and these enzymes perhaps work synergistically with mechanical forces to induce tissue failure. This speculation is supported by the known interplay between mechanical deformation and collagen degradation in soft collagenous tissues [98] [99, 100]. For example, Lee *et al.* demonstrated that tensile loading accelerates the proteolysis of bovine pericardium subjected to collagenase [98], while another study demonstrated that the degradation rate of collagen increased with stretch [100].

5.4.4 Limitations

As with newly developed devices, various circumstances arise during experimental testing. During the membrane inflation studies, the pressure decreased during scanning with the SALS device at higher pressures, likely due to stress relaxation in this tissue [15]. In order to minimize the pressure drop, a smaller area was scanned (i.e. 1 cm x 1 cm) as opposed to the entire membrane surface in an effort to reduce scan time. The pressure drop was ~10-15 mmHg by the end of the scan, which lasted ~7-10 minutes/scan. However, this pressure drop did not have a large effect if any on the structural measurements for two reasons. First, the pressure drop was minimal relative to the pressure level at which the scan was performed (e.g. 100 mmHg vs. 90

mmHg). Additionally, the SALS results remained consistent over the scanned 1cm x1cm scanned area. For example, if the pressure drop affected the SALS measurements, the results from the beginning of the scan would be drastically different than the SALS results at the end of the scan, which was not the case. Additionally, it has been demonstrated that stress-relaxation does not cause a change in D-spacing or angular orientation of collagen [125, 129].

As discussed in section 5.2.4, a 1cm x 1cm square section was scanned with the SALS device at the following pressures: 0mmHg, 5mmHg, 20mmHg, 50mmHg, 80mmHg, 100mmHg, after which the pressure was incrementally increased 10mmHg until membrane rupture. The 10mmHg increment was chosen because it was unknown what the rupture pressure would be in each specimen due to specimen variability. If a smaller increment was chosen, total test time would drastically increase as well as increase the pressure drop and manually applying a 1 mmHg increment of pressure with a syringe was logistically difficult. Thus, 10mmHg increments of pressure was applied. The fact that no flaws prior to failure were detected with the current 10 mmHg increment should not be construed as an experimental flaw. While finer pressure increments may have shown point defects, it is far more likely that there were none.

The average calculated areal stretch of the FM prior to rupture (2.51 ± 0.048) was similar to the value presented in section 3.3 (2.56 ± 0.08), which was estimated from MRI images. However, these tissues were not prepared in exactly the same way. It is likely that the tissue used for the membrane inflation studies were slightly stretch upon receiving them altering the unloaded reference state. Additionally, the tissue in the membrane inflation test was handled significantly during experimental set-up. Due to the delicate nature of this tissue, it is likely that this caused deformation in the amnion prior to the inflation test, altering the unloaded reference state. Thus, if they were prepared in exactly the manner, this distortion could be avoided, and it

is likely that the stretch at 5 mmHg and 20 mmHg would be more similar to the values presented in section 3.3.

Finally, only the amnion was used in this study because due to the use of the SALS device. Opaque tissues like the intact FM, must be clear with glycerol in order to remove the water content within the tissue. This process was necessary for accurate SALS measurements. However, clearing of the tissue may alter the mechanical properties of the tissue. The amnion layer of the FM is translucent, however, and this clearing process is not necessary for the this tissue. Thus, only the amnion layer was used in this study. This is justified in the fact that the amnion layer dominates the mechanical response of the tissue and most of the type I collagen in the FM. While there is type I collagen in the choriodecidua layer, it is present in a lesser amount. Also, it is assumed that the amnion layer and choriodecidua layer, which are firmly adhered prior to failure, stretch the same amount under *in vivo* loading prior to failure of the choriodecidua layer.

5.4.5 Summary and conclusions

Prior to this study, it was unclear how failure initiates in the FM and how the underlying microstructure of the FM dictates the mechanical response. Through this study, it was confirmed that under isotropic loading, there are not large fiber rotations and that the increased NOI values, an indicator of fiber alignment, was due to the uncrimping of collagen fibers. Additionally, it was confirmed that the collagen fibers recruit rapidly under loading, and the tissue did not stretch significantly more prior to failure, which may be an important aspect of membrane failure. Finally and most importantly, it was confirmed that failure at the fiber level in the amnion layer

of the FM is a catastrophic event. These findings provide a fundamental basis for understanding the altered structure-function relationship of the "weak zone" of the FM.

6.0 SUMMARY, IMPLICATIONS, AND FUTURE DIRECTIONS

6.1 SUMMARY OF MAIN FINDINGS

The main findings of the present study are summarized according to specific aim. The overall impact of this work is described in the following section 6.2.

6.1.1 Specific Aim 1: Characterize the sub-failure structure-strength behavior of the FM under physiological loading conditions.

In the first aim of the present study, it was hypothesized that the baseline structure-strength relationship of "non-weak" FM tissue must be established in order to improve our understanding of FM tissue biomechanics. Without this fundamental understanding, failure properties of the FM cannot be accurately investigated. In this study, it was found that under biaxial loading the FM demonstrated the classical "toe" region found in soft tissues at lower values of stretch, followed by a transition into a highly linear region. With increased values of stretch, the collagen fibers continued to straighten, until the upper bound stretch was obtained (i.e. the point where all collagen fibers are straight). The average upper bound areal strain (areal stretch-1) was found to be to 0.48 ± 0.05, which corresponded to a tension level of 24.31 ± 1.77. Note, that the estimated physiological loading level was 34.90 ± 0.73, which corresponded to an areal strain

level of 0.50 ± 0.05 34.90 ± 0.73. These findings suggested that after the upper bound strain is obtained, the FM has limited stretching ability thereafter. Thus, little or no structural reserve exists in the FM. Additionally, it was found that the FM behaves as an effectively isotropic material under loading, allowing the FM to adapt to the bulk loads of the fetus and the amniotic fluid as well as tolerate fetal movement throughout gestation. The results from this study provide a better understanding of the sub-failure structure-function relationship of the FM and provide information on how the FM transitions to failure.

6.1.2 Specific Aim 2: Implement a structural constitutive model to investigate the sub-failure response of the FM.

The goal of this aim was to build on the results of Specific Aim 1 and to further characterize the sub-failure structure function relationship of the FM. The results of this study provided the first data on the effective collagen fiber stiffness of the intact FM from planar biaxial experiments, which was related to the fiber angular distribution of the FM. The results of this study, demonstrated that the FM collagen fibers were recruited at high strain values, yet once recruitment begins, the FM collagen fibers were recruited rapidly. These results indicate that FM is loaded close to its failure stretch, suggesting that the FM contains minimal structural reserve and may be an important aspect of its failure properties. Also, since failure did not occur during sub-failure loading, it is apparent that collagen fibers do not begin to fail until all collagen fibers are fully recruited. Additionally, the fiber angular results confirm the finding in Specific Aim 1. While on a per specimen basis there appeared to be fiber alignment in the FM, the collagen fibers were not aligned globally in relation to any anatomic structure in the uterus or placenta, and the FM is an effectively isotropic material. These findings further contribute the understanding of

the physiologic structure-function relationship of the FM. Furthermore, these findings lay the basis for understanding how the FM transitions to normal, physiological failure.

6.1.3 Specific Aim 3: Characterize structural/strength sequelae during failure of the FM in the "non-weak" regions.

In the third aim, it was hypothesized that performing membrane inflation studies while concurrently quantifying the fiber architecture of the FM, specifically the amnion layer, will elucidate how the non-weak FM transitions to failure. This was achieved through the use of a novel device that was integrated into the SALS system, which performed membrane inflation tests up to failure while simultaneously quantifying the collagen fiber architecture. Through this study, it was determined that under isotropic loading, there were not large fiber rotations and that the increased NOI values, an indicator of fiber alignment, was due to the uncrimping of collagen fibers. Additionally, it was confirmed that the collagen fibers recruited rapidly under loading, and the tissue did not stretch significantly more prior to failure, which likely facilitates membrane failure at a prescribed time. The calculated areal stretch values between 5 mmHg and 20 mmHg (i.e. 10 mmHg is the assumed physiological intrauterine pressure prior to labor) was 1.79 ± 0.18 and 2.11 ± 0.09, respectively, with pressure prior to rupture occurring at 2.51 ± 0.05. However, separation of the amnion from the choriodecidua causes a modest amount of deformation in the amnion layer. Thus, when this deformation was accounted for, the areal stretch values at 5 mmHg and 20 mmHg were 1.93 ± 0.17 and 2.26 ± 0.09, respectively, with pressure prior to rupture occurring at 2.69 ± 0.05. In Specific Aim 1, it was determined that the *in vivo* areal stretch was 2.56 ± 0.08, which is assumed to correspond to an intrauterine pressure of 10 mmHg, and an *in vivo* tension value of 2.56 corresponded to a tension value of 103 N/m.

Additionally, the greatest rate of change in areal stretch during the membrane inflation studies occurred at 5 mmHg with a small additional increase in areal stretch at 20 mmHg and no change thereafter. Thus, it can be inferred from the rupture studies that the upper bound areal stretch occurred at 20 mmHg, which corresponded to approximately 20 N/m. These findings are corroborated with the planar biaxial mechanical data from Specific Aim 1, wherein the upper bound tension of the intact FM was determined to be 25.62 ± 1.69 N/m. Finally, prior to this study it was unclear how failure initiates in the FM and how the underlying microstructure of the FM dictates the mechanical response. It was confirmed that failure at the fiber level in the amnion layer of the FM is a catastrophic event. These findings provide a fundamental basis for understanding the altered structure-function relationship of the "weak zone" of the FM.

6.2 IMPLICATIONS OF MAIN FINDINGS

6.2.1 Implication of the structure-function relationship of the non-weak FM on the normal, physiological behavior of the FM

The sub-failure studies performed in Specific Aims 1 and 2 suggested that the FM collagen fibers become fully loaded and are straightened well below estimated physiological loading levels. This indicates that the FM collagen fibers have *little or no structural reserve.* In contrast, other soft tissues such as pericardium, heart valves, and ligaments' physiological operating ranges are either in the early linear region or in the "toe" region of the stress-strain curves [88, 113-117]. However, the FM appears to be loaded proportionally much closer to its failure stretch. In addition, these soft tissues have a large structural reserve, indicating that their

physiological loading ranges are well below their failure strengths [88, 116, 117]. The structural reserves in these tissues prevent them from being deformed past their failure strength. If failure does occur in these tissues, it is usually due to fatigue or a pathological condition. In contrast, the FM is intrinsically designed to fail at a prescribed time, and since the FM has minimal structural reserve in comparison to other soft tissue, failure is probably easily facilitated during labor.

6.2.2 Implication of the structure-function relationship of the FM on FM failure

As demonstrated in Specific Aims 1 and 2, the FM collagen fibers are recruited at high strain values, yet once recruitment begins, the FM collagen fibers were recruited rapidly. Specific Aim 3 substantiated these findings as well as confirmed that failure of the amnion, which is known to dominate the mechanical response of the FM, fails catastrophically at the fiber level. Thus, no fiber is predisposed towards failure prior to biochemical weakening. However, membrane rupture is clearly not entirely a result of physical forces because in 10% of term labor and 40% of premature labor, membrane rupture occurs before contractions begin. It has been demonstrated that proteolytic enzymes, specifically MMP-9 and MMP-2, play a role in membrane rupture [1, 64-67]. Thus, proteolytic enzymes likely play a role in membrane rupture [1], and perhaps work synergistically with mechanical forces to induce tissue failure. This speculation is supported by the known interplay between mechanical deformation and collagen degradation in soft collagenous tissues [98] [99, 100]. For example, Lee *et al.* demonstrated that tensile loading accelerates the proteolysis of bovine pericardium subjected to collagenase [98]. Also, another study demonstrated that the degradation rate of collagen increased with stretch [100]. Thus, weakening of the FM is likely due to the degradation of the basement membrane as well as the

compact layer. There is evidence that MMP-9 is up-regulated in late gestation, and MMP-9 is known to weaken collagen type IV, which is found in the basement membrane of the amnion layer as well as around the trophoblast and the decidua. To date, there is no evidence that the fibrillar collagens, namely type I, are degraded in the human FM. Thus, weakening of the strong compact layer of the amnion, which contains predominantly type I collagen, may be facilitated by the degradation of the molecules that organize collagen type I, such as decorin, biglycan, the fibulin family. There is evidence the MMP-2 can digest decorin [130]. This weakening of the FM can be exacerbated by mechanical stress. For example, collagen fibers are composed of three polypeptide chains (tropocollagens) intertwined to form a triple helix or collagen molecule. The stretching of the collagen molecule may result in the opening of new sites making it more susceptible to enzymatic degradation [100]. If only certain sites were exposed during stretch, then only these collagen fibers would be more susceptible to failure and thus, not all the collagen fibers will fail at once. Additionally, decorin was found to mechanically interact with collagen fibrils via specific binding to the collagen D-period. Thus, if only certain binding sites were exposed due to stretching of the collagen fiber only certain fibers would be affected by enzymatic degradation and thus more susceptible to failure. Another possible mechanism for the increased degradation rate could be that the enzymatic breakdown of a given collagen molecule or binding protein causes the remaining stress in the tissue to be transferred to a neighboring molecule or fibril, respectively, which may then rupture. If this is a widespread event, rapid break down of the collagen fibers could ultimately result in a catastrophic failure of the tissue [100]. While the exact mechanism is unknown, it may be that mechanical stress may facilitate weakening of the collagen fibers by attacking the molecules that organize collagen Type 1, such as decorin, biglycan, the fibulin family. Irrespective of the exact mechanisms, we speculate that

enzymatic degradation of the FM collagen in the "weak zone" may be accentuated by mechanical stress.

6.2.3 Implication of the results on premature rupture of the FM

To date, there are no physical risk factors associated with the biomechanical or structural properties that could be detected with diagnostic tools. The immediate aim of this work was not to develop a diagnostic tool but to establish an improved understanding of the fundamentals of membrane function. In order to understand FM failure, the structure-function relationship of the fetal membrane, which depends on the underlying microstructure, needs to be established in the non-weakened, near/full term FM. Without this fundamental understanding, the relationship between physical rupture and programmed enzymatic weakening activity is not possible. This study provided the fundamental understanding of the structure-function relationship of near/full term, non-weakened FM at the sub-failure and failure level, imparting a platform for future investigation of how the structure-strength relationship of the FM is altered in the "weak zone" resulting in FM rupture. Finally, after it is establish how membrane weakening via enzymatic degradation leads to mechanical rupture of the FM in normal pregnancy, one can then begin to investigate what occurs incorrectly during PROM or PPROM. If one could narrow down what is actually causing the weakening of the FM (i.e. MMP up-regulation, TIMP down-regulation, disease, etc.) resulting in rupture, then risk factors can be identified and prevention methods can be developed.

6.3 FUTURE STUDIES

6.3.1 Examining the sub-failure and failure properties of weakened FM

The "weak zone" of the FM has unique mechanical properties which facilitates tissue failure and comparing the "weak zone" and "non-weak" zone tissues will allow one to elucidate the unique micro-mechanical mechanisms that result in normal, term FM failure. Thus, future studies should include investigation of sub-failure and failure properties of the weakened FM. This would entail repeating Specific Aims 1 and 3 on weakened FM.

As a first step, the sub-failure properties of term "weak" FM would need to be established via planar biaxial testing as was done in Specific Aim 1. These results could then be compared to the sub-failure properties of "non-weak" FM, elucidating how weakened FM transitions to failure. In the current study, it was determined that that the FM collagen fibers are recruited at high strain values, yet once recruitment begins, the FM collagen fibers were recruited rapidly. These results indicate that FM is loaded close to its failure stretch, suggesting that the FM contains minimal structural reserve and may be an important aspect of its failure properties. However, weakened collagen fibers may not behave in the same manner, and understanding these differences will provide insight into how failure occurs in the "weak zone." Figure 6-1 is a schematic of four the possible sub-failure behaviors of the weakened FM. First, the sub-failure properties of the weakened tissue may not be any different than "non-weak" FM. Thus, the resulting sub-failure Tension-stretch curve would be exactly the same as described in the current study (Figure 6-1; curve 1, grey line). In the second scenario, the collagen fibers are recruited rapidly, but the tissue fails at a lower tension level (Figure 6-1, curve 2, green line). This would

indicate that the FM fibers are weakened equally, and all fibers fail at once. Thus, the weakened tissue would fail at a lower tension level than the "non-weak" FM would.

The third scenario is depicted by curve 3 (Figure 6-1; dotted blue line). The collagen fibers are not recruited as rapidly, and the Tension-stretch response is not as stiff as the "non-weak" FM. However, failure occurs at the same tension as in the normal tissue. This could indicate that fiber failure may be occurring during collagen recruitment, but not enough fibers are failing to cause complete tissue failure. In the last possible situation, the collagen fibers are not recruited rapidly, and the tissue fails at a lower tension value (Figure 6-1; curve 4, orange line). This would indicate that fiber failure occurs while other fibers are being recruited. However, the recruited fibers cannot bear the extra load from the failed fibers resulting in complete tissue failure at lower tension values. Once it is established how the underlying collagen fiber architecture is altered as evidence in Figure 6-1, one can then establish risk factors which alter the collagen architecture as well as develop therapies to prevent or arrest premature membrane rupture.

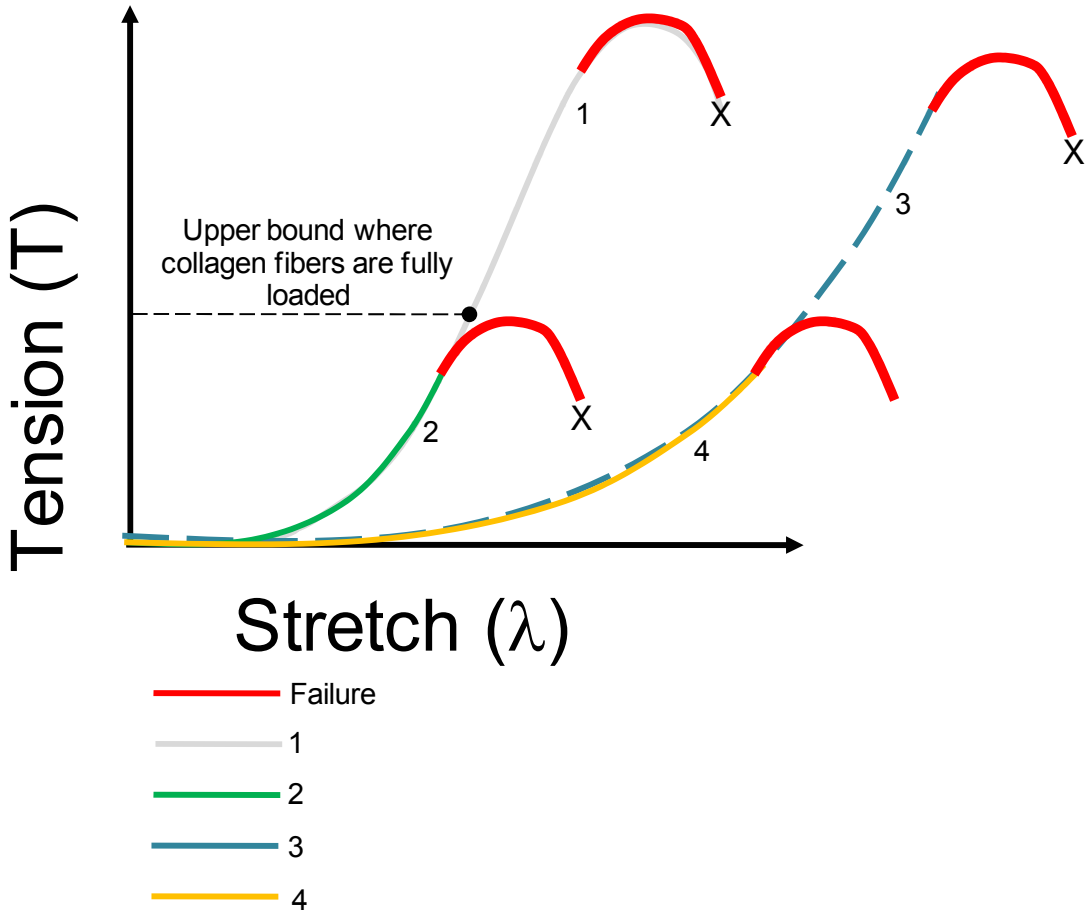

Figure 6-1. Curve 1 (grey) describes the physiologic sub-failure behavior, where failure, represented as the red line, occurs soon after. Fetal membranes that fail prematurely can be described by three possible scenarios, depicted in curves 2-4. In curve 2 (green), the collagen fibers are recruited rapidly, but the tissue fails at a lower tension level. The second scenario is depicted in curve 3 (blue, dotted line). The collagen fibers are not recruited as rapidly. Thus, more stretch is required to fully straighten the collagen fibers. However, failure occurs at the same tension as in the normal tissue. In the third possible situation, curve 4 (orange), the manner in which collagen is recruited and the manner in which it fails is different from the physiological behavior. In this scenario, the collagen is straightened less rapidly, and the tissue fails at a lower tension. Once it is established how the underlying collagen fiber architecture is altered as evidence in curve 2-4, one can then establish risk factors which alter the collagen architecture as well as develop therapies to prevent or arrest premature membrane rupture.

After the sub-failure properties have been established, one can then begin to investigate the failure properties of term "weak" FM. Thus, failure studies would be performed with the use of novel membrane inflation device described in section 5.2.3 as was done in Specific Aim 3. Failure of the weakened FM could manifest in different way. For example, if the sub-failure properties of the weakened FM were described by the first sub-failure behavior discussed (Figure 6-1; curve 1, grey line), FM failure could either be catastrophic or a result of small point defects leading to total failure. However, if the sub-failure behavior of the weakened FM was described by the second scenario, failure is likely to be a catastrophic event because all collagen fibers were weakened equally (Figure 6-1; curve 2, green line). Finally, if the sub-failure behavior is described by either the third or fourth scenario, it would be likely that failure would be a result of point defects leading to total tissue failure (Figure 6-1; curve 3, dotted, blue line and curve 4, orange line).

6.3.2 Development of a structural constitutive model for failure

In addition to the sub-failure and failure studies discussed in section 6.3.1, current approaches towards structural constitutive modeling used in Specific Aim 2 will be extended to develop a structural constitutive model for FM tissue failure at the fiber level. The key aspect of this approach is that one can use the sub-failure results of "non-weak" and "weak" FM from section 2.3.1 and section 6.3.1, respectively, to guide the overall model formulation. Then key structural information obtained in sections 2.3.1, 5.3.1, 5.3.2 and 6.3.1 will be utilized to determine key failure characteristics to guide the model form. The model will first be matched to the "non-weak" zone tissue for "baseline" parameter determination. Next, one can vary key structural parameters (e.g. fiber stiffness, fiber strain at failure, fiber stress at failure) to determine which

parameter leads to the greatest changes in tissue failure characteristics. This will be followed by fitting the "weak" zone membrane inflation failure data from section 6.3.1. This approach will allow for unique parametric studies to determine what major structural elements lead to tissue failure.

6.3.3 Examining the effects of cytokines on mechanical properties of the FM

A next step would be the investigation of the effects of collagen remodeling and apoptosis on failure due to altered collagen fiber architecture with the membrane inflation device presented in section 5.2.3. Recent studies have shown that TNFα and IL-1β induced collagen remodeling and apoptosis [68]. Also, recent evidence suggests that TNFα induces IL-1β in choriodecidua explants [131]. We hypothesize that by treating the non-weak zone FM with cytokines known to be involved with the weak zone, we can reproduce the weak zone effects of the FM. After incubation of FMs *in vitro* with agents known to cause apoptosis, the amnion layer will be separated from the intact FM for membrane inflation testing. The treated amnion tissue can be incrementally loaded until failure occurs (see section 5.2.4), allowing one to determine how the weakened amnion will fail. These results should corroborate the work done by Moore et. al [61, 62, 68, 83, 97]. The biophysical and correlating biochemical studies that are described above will provide insight into the transition from a non weak FM to a weak one that can rupture. This understanding will plausibly allow us to anticipate and develop strategies to intervene to prevent premature FM weakening which leads to rupture and preterm birth.

APPENDIX A

MEMBRANE INFLATION DEVICE – DESIGN AND VALIDATION

A.1 TECHNICAL DRAWINGS FOR DEVICE DESIGN

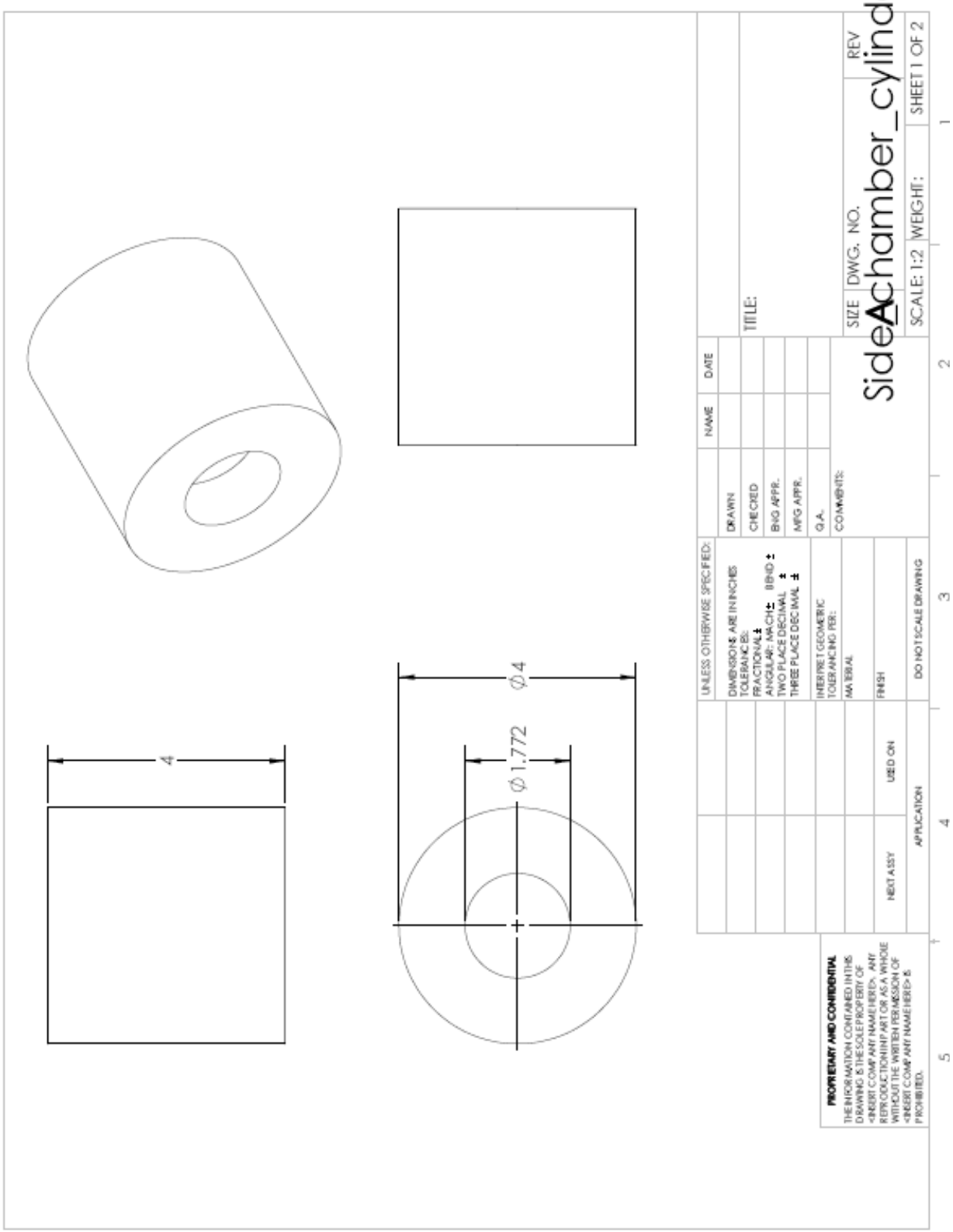

Figure A - 1. Technical drawing for the hollow cylinder.

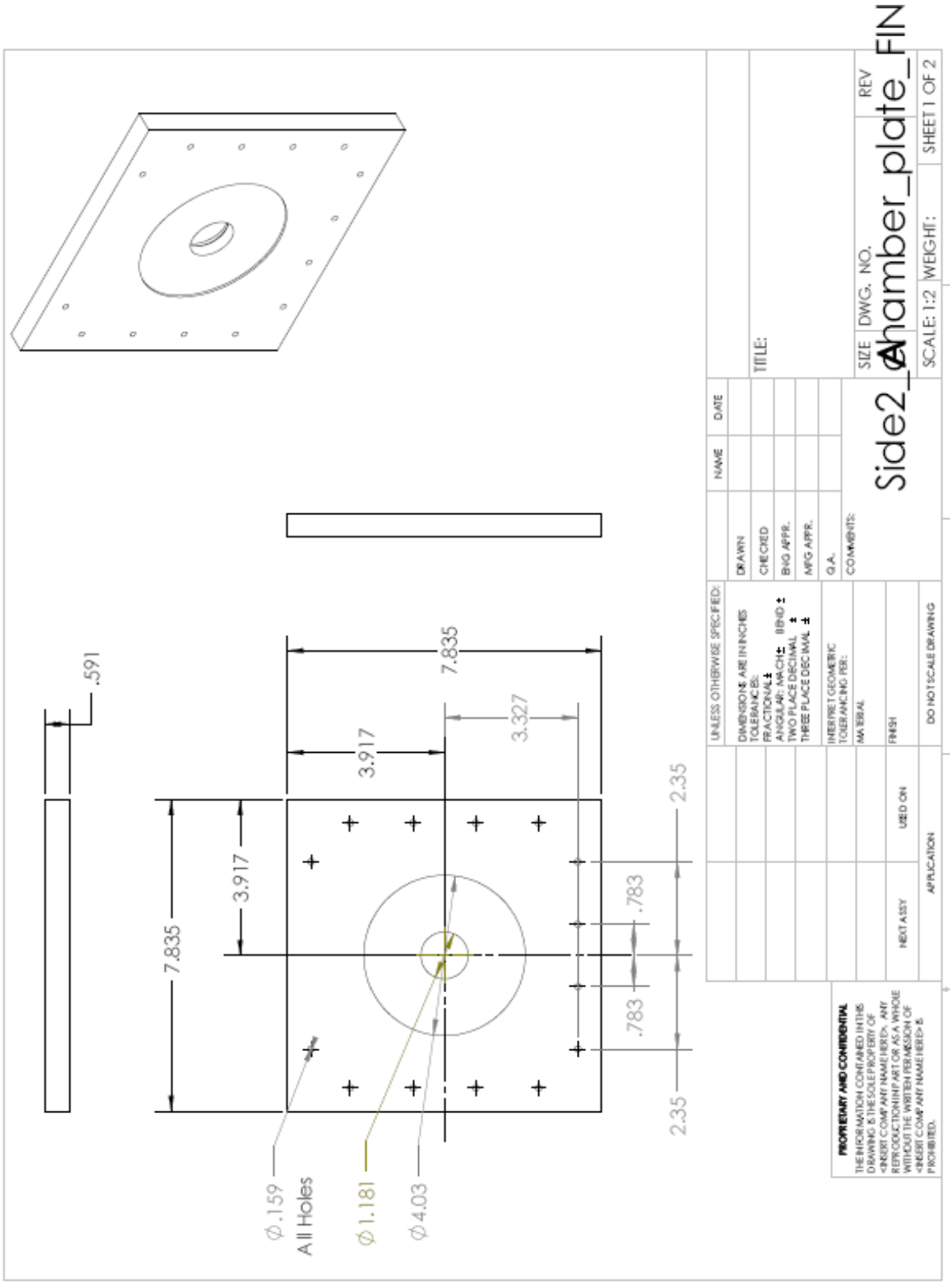

Figure A - 2. Technical drawing for the clamping plate1.

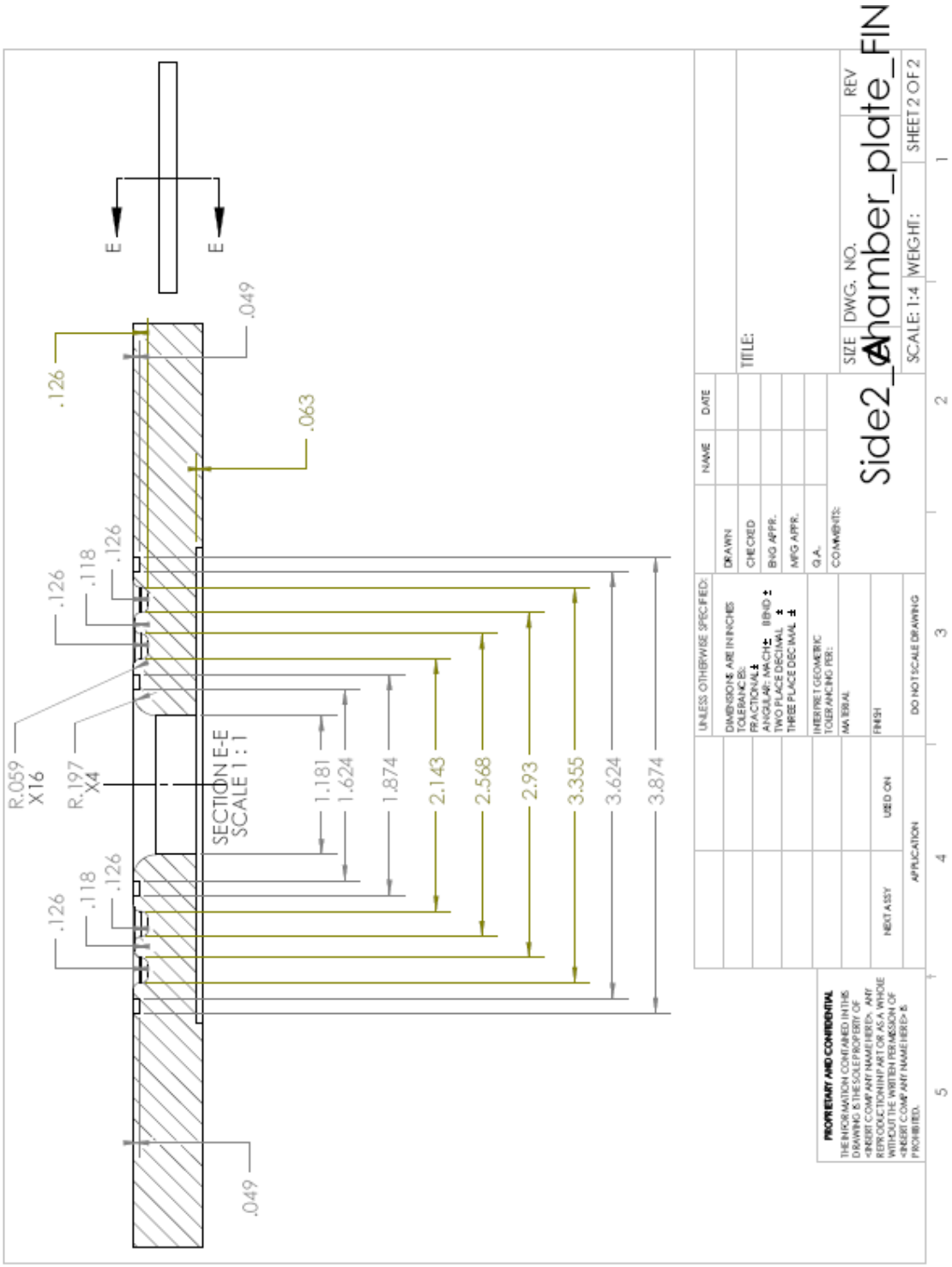

Figure A - 3. Section view of clamping plate1.

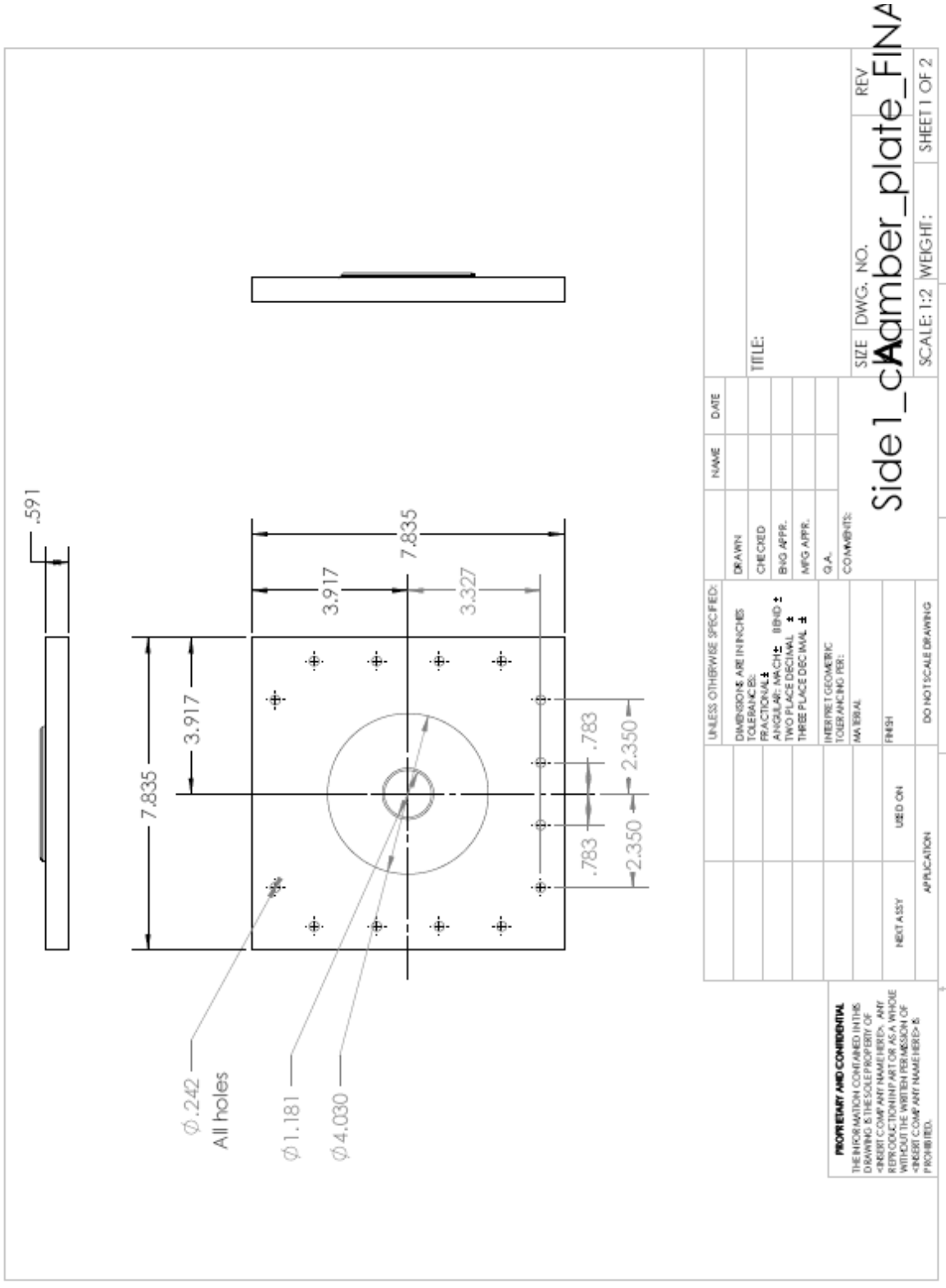

Figure A - 4. Technical drawing for the clamping plate2.

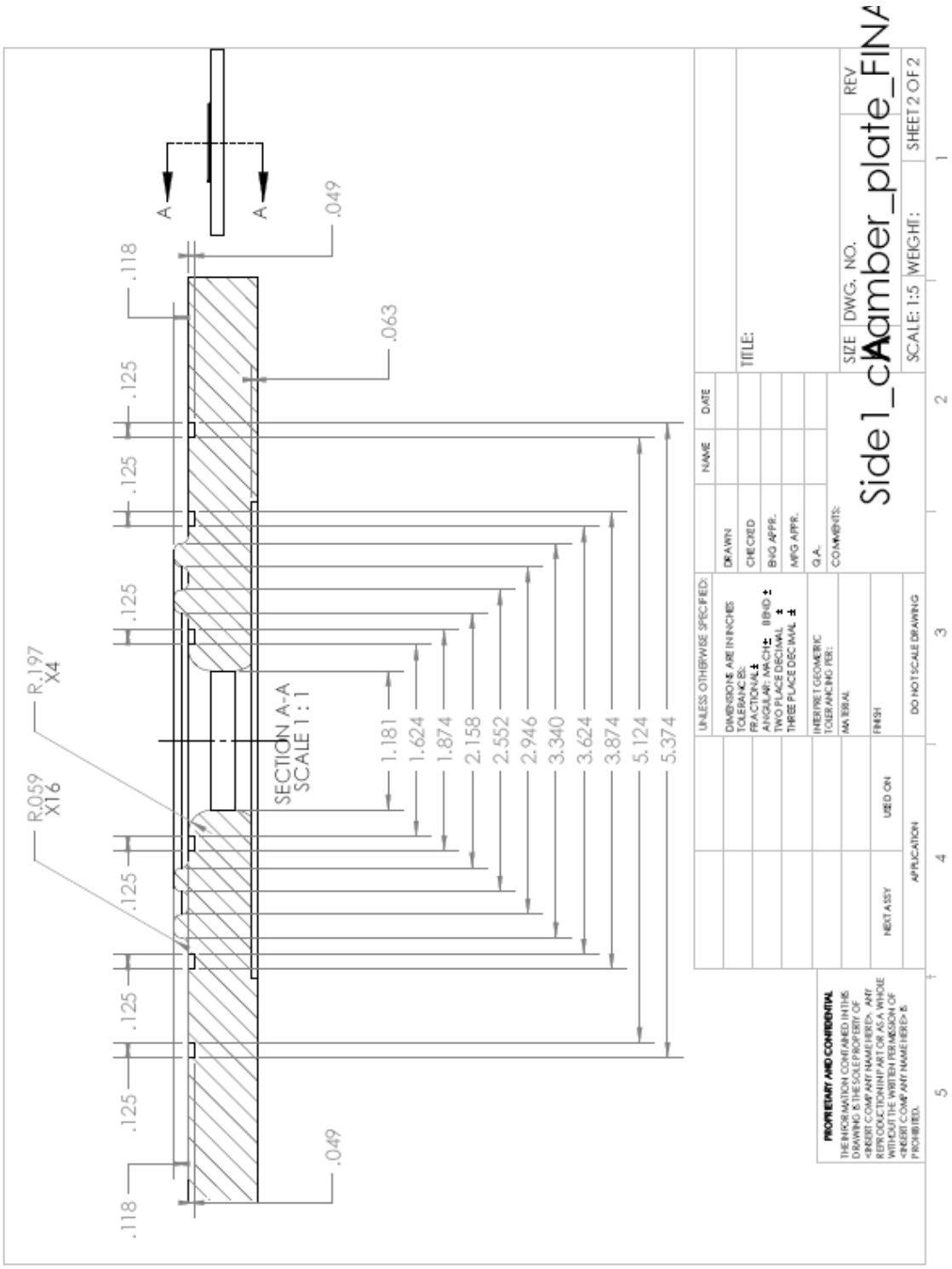

Figure **A - 5.** Section view of clamping plate 2.

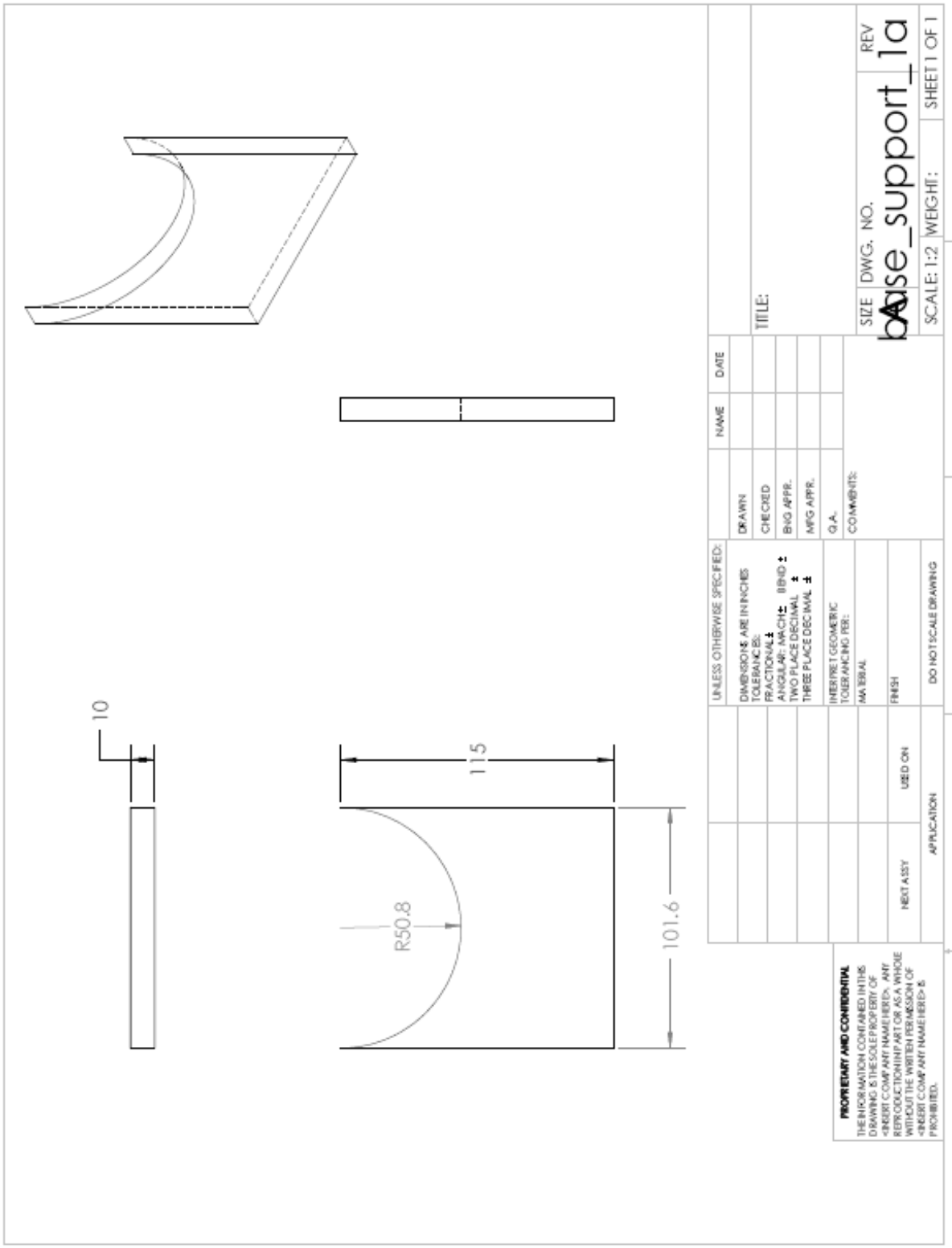

Figure A - 6. Technical drawing for device cradle.

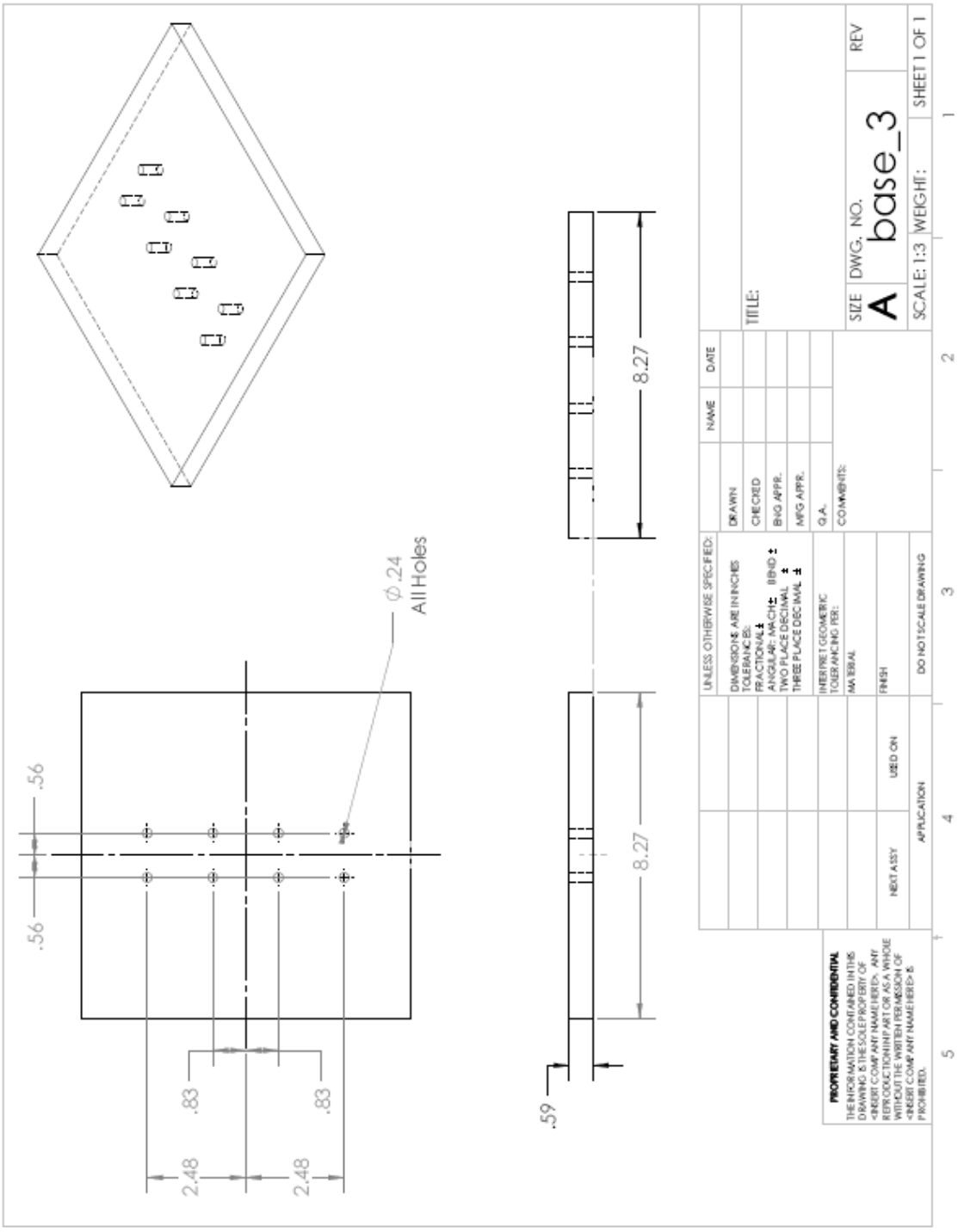

Figure A - 7. Technical drawing for base of cradle.

A.2 DEVICE VALIDATION

A.2.1 Device validation – cast acrylic windows

In order to verify that the cast acrylic windows of the membrane inflation device (Figure 5-1; part e) did not cause the laser of the SALS device (Figure 5-1; part f) to be distorted when it passed from cylinder 1 (Figure 5-1; part a) through cylinder 2 (Figure 5-1; part c), a pilot study was performed. First the laser beam scattered was passed through air, and the beam profile was captured on the screen of the SALS device (Figure A - 8a). Then the burst device was filled with PBS (pH 7.4) at room temperature, which is used during burst testing, and placed in line and directly perpendicular to the laser beam. The beam profile was again capture on the screen of the SALS device (Figure A - 8b). The beam profiles were segmented (Figure A - 8 c and d) and the pixel coordinates from the surface of the segmented images were extracted and plotted comparison (Figure A - 7e). There were not observable differences between the two beam profiles (Figure A - 8e; R2 = 0.9259). In conclusion, the laser beam was not refracted by the acrylic windows of the burst device, and the device design is amenable to accurate structural measurements.

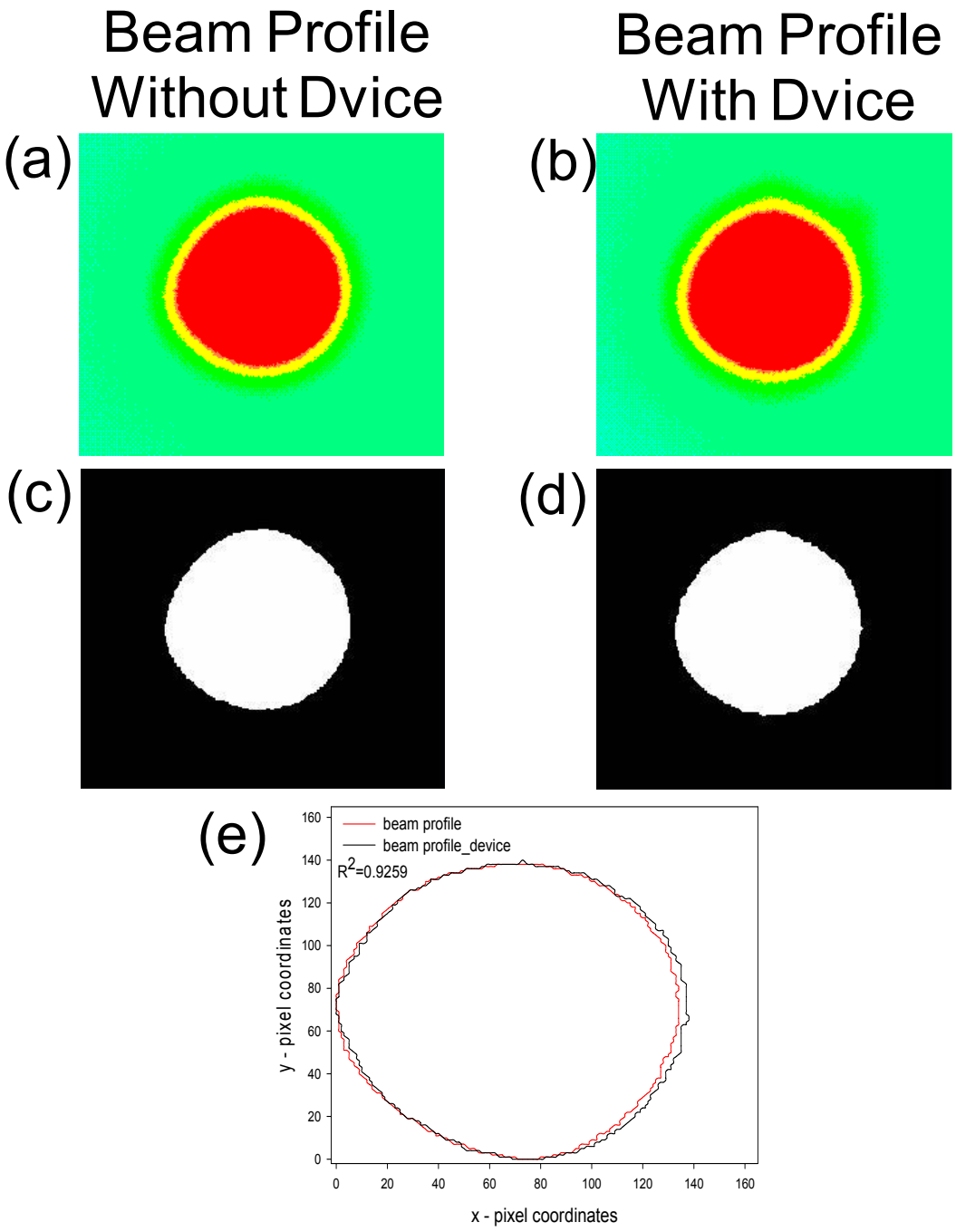

Figure A - 8. (a) Laser beam profile without the device (i.e. beam was passed through air). (b) The device was filled with PBS and placed in front of the laser beam. (c,d) The laser beam profiles were then segmented. (e) Finally, the segmented images were compared and it was determined that the laser beam of the SALS device was not distorted by the acrylic windows of the SALS device.

A.2.2 Device validation – Homogenous Deformation

In order to ensure that the amnion layer of the FM was deforming homogenously, validation studies were performed. The first study was performed on latex rubber, an assumed isotropic material. Latex rubber was placed inside the burst device and was inflated. Images were taken of the profiles of the inflated latex from the top view and side view of the burst device (Figure A - 9 a and b). The profile images were then segmented with free software, Medical Image Processing, Analysis, and Visualization (MIPAV), for the NIH website (http://mipav.cit.nih.gov/) (Figure A - 9 c and d). Next, the pixel coordinates from the surface of the segmented images were extracted and plotted comparison (Figure A - 9e). The R^2 value between the two profile curves was 0.9105, where (Figure A - 9e). Thus, it is assumed that the latex deformed homogenously and any difference in the plotted curves can be contributed to experimental error associated with manual segmentation of the profile images and image quality. However, it is important to note, that the latex distends past its fixture opening during inflation, which can be seen in both the images and the plotted image profiles (Figure A - 9).

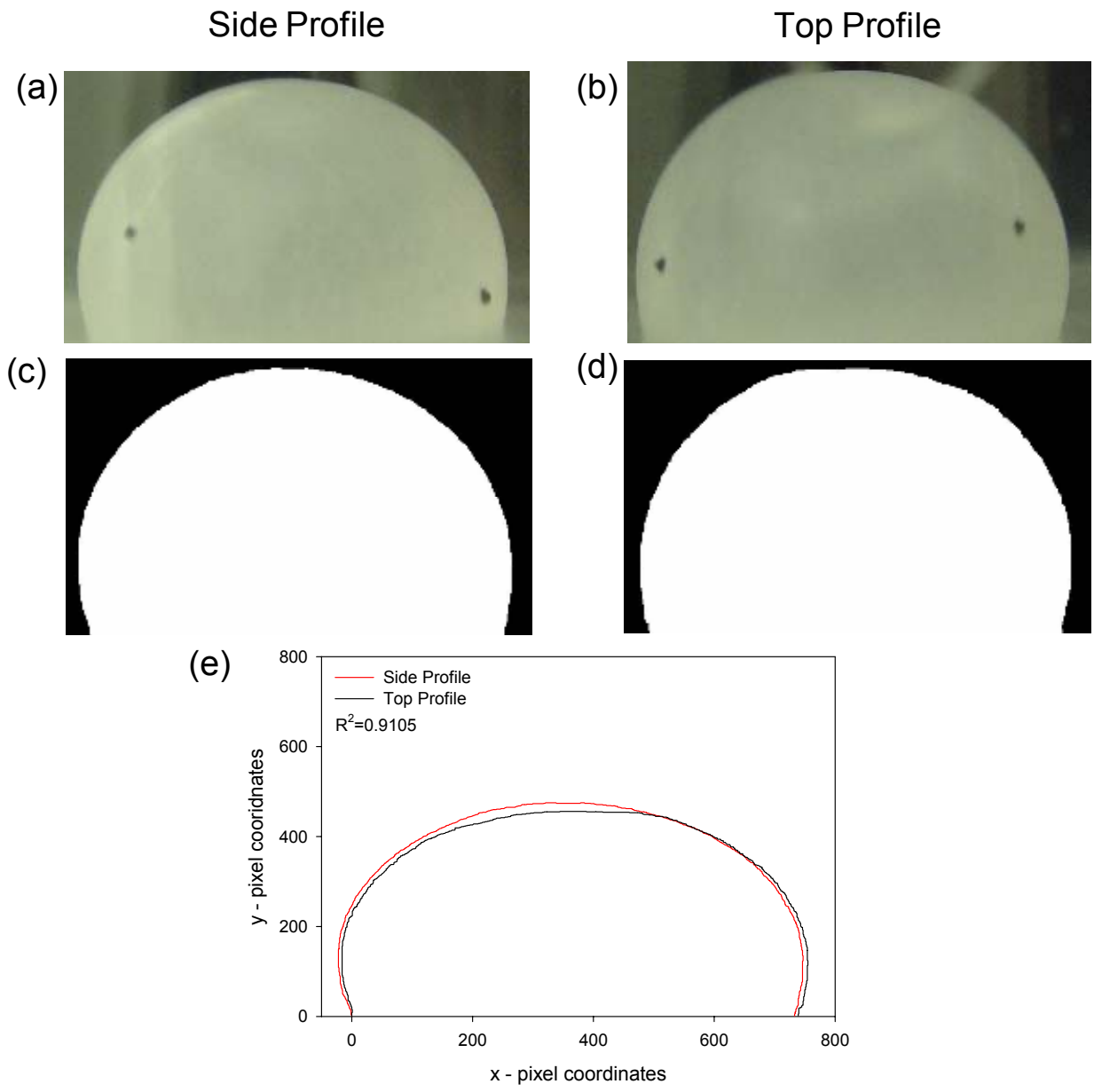

Figure A - 9. Image of the (a) side and the (b) top profile of inflated latex with (c,d) corresponding segmented images. (e)The surfaces of the segmented images were compared, and it was determined that the latex deformed homogenously.

Next, the same study was performed on the amnion (Figure A - 10). The amnion was inflated until the total displacement was of the amnion was ~15mm, since pilot study revealed that the amnion ruptured at a displacement of ~18-20 mm. The same conclusions can be made regarding the amnion tissue. It does in fact deform homogenously, evidence by an R^2 value of 0.9398 between the two profile curves (Figure A - 10e). Again, any difference between the profile curves can be attributed to experimental error associated with manual thresholding of the profile images and image quality. Conversely, the amnion layer does not does not distend past its fixture opening as does the latex during inflation (Figure A - 9). Note, that if the amnion was capable of displacing more the 18-20 mm, it probably would distend past its fixture opening like the latex.

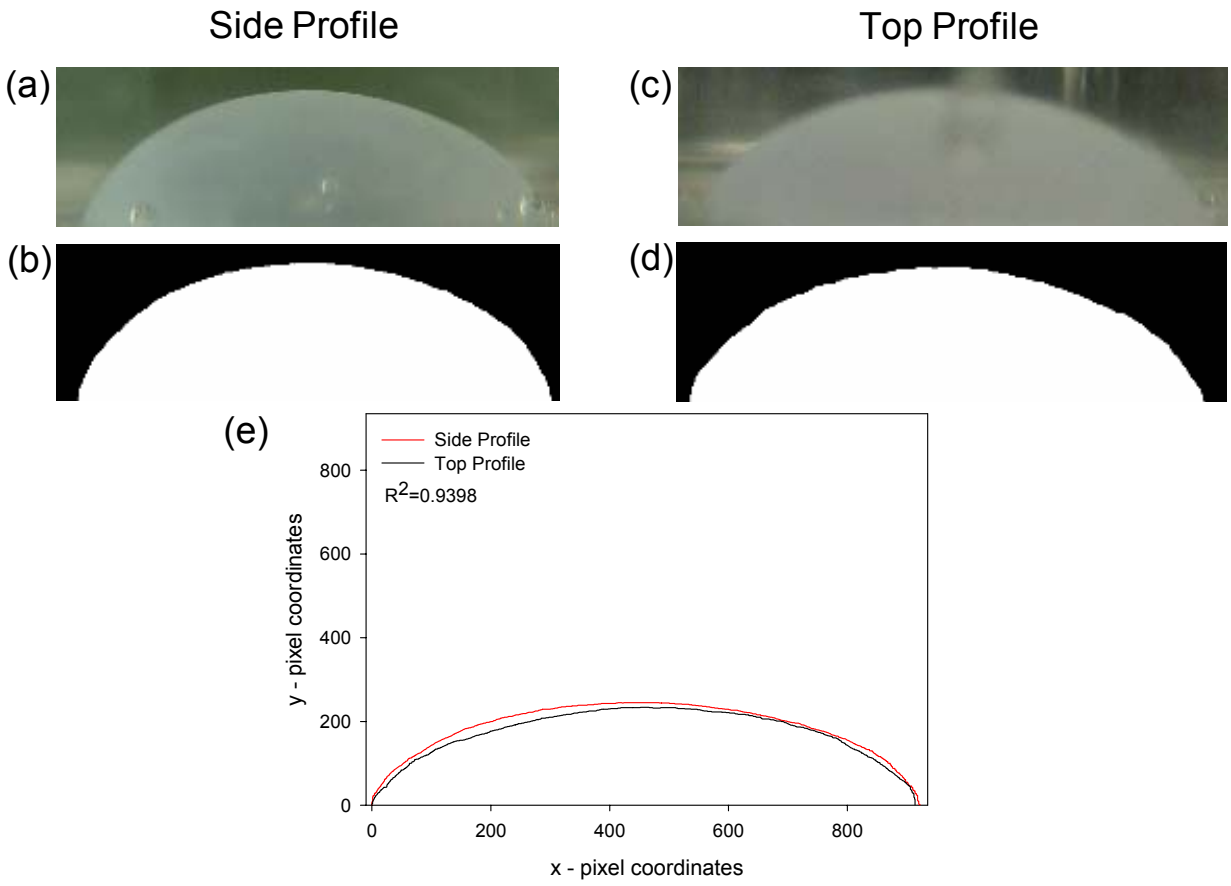

Figure A - 10. Image of the (a) side and the (b) top profile of inflated amnion layer of the FM with (c, d) corresponding segmented images. (e)The surfaces of the segmented images were compared, and it was determined that the amnion deformed homogenously.

APPENDIX B

QUANTIFICATION OF AMNION DEFORMATION ASSOCIATED WITH LAYER SEPARATION

B.1 METHODS

B.1.1 Tissue procurement and specimen preparation

FM specimens were collected from women undergoing Cesarean section or Vaginal deliveries at MetroHealth Medical Center, Cleveland Ohio after normal term (37-42 weeks) pregnancies. A CWRU/MetroHealth Medical Center institutional review board (IRB) approved protocol was utilized. FM of patients with clinical chorioamnionitis, meconium, maternal diabetes, or multiple gestations were specifically excluded. For these initial studies, FM fragments from regions distant from the "weak zone" as determined by methods previously described were selected [61, 62]. Fresh FM fragments were stored in 1X Minimum Essential Medium and shipped to Pittsburgh, PA overnight on ice. FM specimens were tested on the day of receipt. Next, a 20 mm x 20 mm square was dissected from the intact FM specimens sent to our laboratory. Four fiducial markers were placed in the center of the tissue in a 2 x 2 array (Figure B - 1).

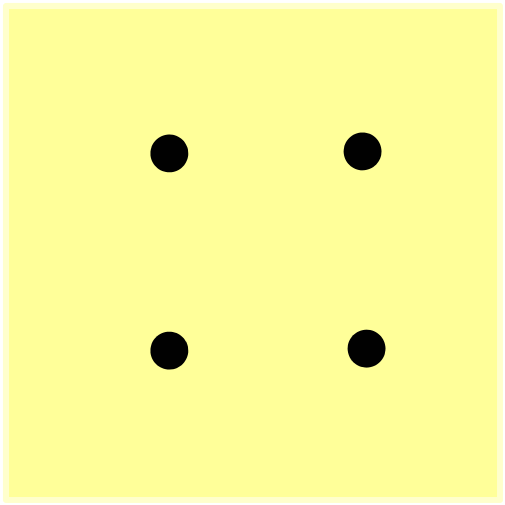

Figure B - 1. Square specimen with fiducial markers placed in a 2 x 2 array.

Next, the amnion layer was peeled off of the choriodecidua layer, and an image was immediately taken of the 4 marker positions. Images were then taken at 0.5, 1, 1.5, 2, and 4 hours in order to track the marker displacements over time. This procedure was completed on 8 samples.

B.2 RESULTS

Upon initial separation, the amnion layer of the FM deformed. However, over a 4 hour period no further deformation was attained (Figure B - 2). The values presented in Figure B - 2 are presented as mean ± SEM. Thus, areal deformation used in chapter 5.0 was based on the deformation values at 4 hours. The areal deformation estimated from the following equation:

$$Areal\ Stretch = \lambda_1 \cdot \lambda_2 \tag{B-1}$$

and was calculated to be 1.077.

Time	$F = \begin{bmatrix} F_{11} & F_{12} \\ F_{21} & F_{22} \end{bmatrix}$
0 Hours:	$F = \begin{bmatrix} 1.038 \pm 0.017 & -0.011 \pm 0.032 \\ 0.071 \pm 0.032 & 1.038 \pm 0.023 \end{bmatrix}$
0.5 Hours:	$F = \begin{bmatrix} 1.043 \pm 0.018 & 0.049 \pm 0.030 \\ 0.020 \pm 0.023 & 1.041 \pm 0.027 \end{bmatrix}$
1 Hours:	$F = \begin{bmatrix} 1.038 \pm 0.018 & 0.004 \pm 0.013 \\ 0.072 \pm 0.028 & 1.044 \pm 0.025 \end{bmatrix}$
1.5 Hours:	$F = \begin{bmatrix} 1.040 \pm 0.019 & 0.006 \pm 0.017 \\ 0.094 \pm 0.034 & 1.039 \pm 0.027 \end{bmatrix}$
2 Hours:	$F = \begin{bmatrix} 1.043 \pm 0.019 & 0.021 \pm 0.024 \\ 0.049 \pm 0.012 & 1.035 \pm 0.028 \end{bmatrix}$
4 Hours:	$F = \begin{bmatrix} 1.041 \pm 0.021 & 0.044 \pm 0.026 \\ 0.023 \pm 0.026 & 1.035 \pm 0.029 \end{bmatrix}$

Figure B - 2. Upon initial separation, the amnion deformed stretched 1.038 in the F11 direction and 1.038 in the F22 direction. After the initial separation, the amnion did not continue to deform. (n = 8)

BIBLIOGRAPHY

1. Moore, R.M., Mansour, J.M., Redline, R.W., Mercer, B.M., Moore, J.J., The Physiology of Fetal Membrane Rupture: Insight Gained from the Determination of Physical Properties. Placenta, 2006. **27**: p. 1037-1051.

2. O'Rahilly, R. and F. Mèuller, Human embryology & teratology. 3rd ed. 2001, New York: Wiley-Liss. xii, 505.

3. Nikas, G., A. Ao, R.M. Winston, and A.H. Handyside, Compaction and surface polarity in the human embryo in vitro. Biol Reprod, 1996. **55**(1): p. 32-7.

4. Tulsiani, D., Introduction to mammalian reproduction. 2003, Boston: Kluwer Academic Pub. xii, 403.

5. Strachan, T. and A.P. Read, Human molecular genetics 3. 3rd ed. 2004, London ; New York Independence, KY: Garland Science ; Distributed in the USA by Taylor & Francis. xxv, 674.

6. Ornella, P., Alviano, F., Bagnara, G.P., Bilic, G., Buhring, M.E., Hennerbichler, S., Liu, B., Magatti, M., Mao, N., Miki, T., Marongiu, F., Nakajima, H., Nikaido, T., Portmann-Lanz, C.B., Venkatachalam, S., Soncini, M., Stadler, G., Surbekk, D., Takahashi, A., Sakuragaw, H.R.N., Wolbank, S., Ziesberger, S., Zisch, A., Strom, S.C., Concise Review: Isolation and Characterization of Cells from Human Term Placenta: Outcome of the First International Workshop on Placenta Derive Stem Cells. Stem Cell Express, 2007.

7. Glasser, S., Aplin, J.D., Linda, C.G., Tabibzadeh, S., The endometrium. 2002: Informa Health Care. 675.

8. Brauer, P.R., Human embryology: the ultimate USMLE step 1 review. 2003: Elsevier Health Sciences. 103.

9. Moore, K.L. and T.V.N. Persaud, Before We Are Born: Essentials of Embryology and Birt Defects. 6 ed. 2003, Philadelphia: Saunders.

10. Rana, M.W. and A.H. Rana, Human embryology made easy. 1998: CRC Press. 351.

11. Ilancheran, S., Y. Moodley, and U. Manuelpillai, Human fetal membranes: a source of stem cells for tissue regeneration and repair? Placenta, 2009. **30**(1): p. 2-10.

12. Oyen, M.L., Cook, R.F., Calvin, S.E., Mechanical failure of human fetal membrane tissues. Journal of Materials Science: Materials in Medicine, 2004. **15**: p. 651-658.

13. Akira, I., Takahashi, S., Hirakawa, S., Mori, Y., Interleukin-1 and connective tissue metabolism of fetal membranes, in *The Extracellular Matrix of the Uterus, Cervix and Fetal Membranes: Synthesis, Degradation and Hormonal Regulation*, P.C. Leppert and J.F. Woessner, Editors. 1991, Perinatology Press: Ithaca, NY.

14. Parry, S., Strauss, J.F., Premature Rupture of The Fetal Membranes. New England Journal of Medicine, 1998. **338**(10): p. 663-670.

15. Oyen, M.L., Cook, R.F., Stylianopoulos, T., Barocas, V.H., Calvin, S.E., Landers D.V., Uniaxial and biaxial mechanical behaviour of human amnion. Journal of Materials Research, 2005. **20**(11): p. 2902-2909.

16. Kellicot, W.E., Outlines of Chordate Development. 1913, New Your: Henry Holt and Company. 471.

17. (CDC), C.f.D.C.a.P., Infant Mortality-United States, 1992. Morbidity and Moratality Weekly Report (MMWR), 1994. **43**(49): p. 905-9.

18. Martin, J.A., B.E. Hamilton, P.D. Sutton, S.J. Ventura, F. Menacker, and M.L. Munson, Births: final data for 2003. Natl Vital Stat Rep, 2005. **54**(2): p. 1-116.

19. Mathews TJ and M. MF, Infant mortality statistics from the 2003 period linked birth/infant death data set, in *National vital statistics reports*. 2006, National Center for Health Statistics: Hyattsville, MD.

20. Outcomes, C.o.U.P.B.a.A.H., Preterm Birth: Causes, Consequences, and Prevention, ed. R.E.a.B. Behrman, A.S. 2007: National Academies Press.

21. Committee to Study the Prevention of Low Birth Weight, D.o.H.P.a.D.I.o.M., Preventing low birth weight. Washington: Natonal Academy Press, 1985.

22. Hernandez, J.A., Offitt, J., Buttfield, L.J., The cost of care of the less than 1000 gram infant. Clin Perinatol, 1986. **13**: p. 461-76.

23. Mercer, B.M., Preterm Premature Rupture of the Membranes. Obstetrics and Gynecology, 2003. **101**(1): p. 178-93.

24. Batemen, J.F., Lamande, S.R., Ramshaw, J.A.M, Collagen Superfamily, in *Extracellular Matrix. Volume2. Molecular Components and Interactions*, W.D. Comper, Editor. 1996, Harwood Academic Publishers: Amsterdam, Netherlands.

25. Koide, T., Triple helical collagen-like peptides: engineering and applications in matrix biology. Connect Tissue Res, 2005. **46**(3): p. 131-41.

26. Gelse, K., E. Poschl, and T. Aigner, Collagens--structure, function, and biosynthesis. Adv Drug Deliv Rev, 2003. **55**(12): p. 1531-46.

27. Weiss, J.B. and S. Ayad, An introduction to collagen, in *Collagen in Health and Disease*, J.B. Weiss and M.I.V. Jayson, Editors. 1982, Churchill Livingstone: Edinburgh, LondonNew York.

28. Nimni, M.E. and R.D. Harkess, Molecular Structure and Functions of Collagen, in *Collagen Volume I Biochemistry*, M.E. Nimni, Editor. 1988, CRC Press: Boca Raton, FL.

29. Nimni, M.E. and R.D. Harkness, Molecular structure and functions of collagens., in *Collagen Volume I Biochemistry.*, M.E. Nimni, Editor. 1988, CRC Press: Boca Raton, FL.

30. Engel, J., THE ZIPPER-LIKE FOLDING OF COLLAGEN TRIPLE HELICES AND THE EFFECTS OF MUTATIONS THAT DISRUPT THE ZIPPER. Annu. Rev. Biophys. Chem., 1991. **20**: p. 137-52.

31. Viidik, A., C. Danielsen, and H. Oxlund, On fundamental and phenomenological models, structure and mechanical properties of collagen, elastin and glycosaminoglycan complexes. Biorheology, 1982. **19**: p. 437-451.

32. Price, J.P., Njus, G.O., Conway, T.A. Ultrastructural Properties of Rat Tail Tendon. in *Fifteenth Southern Biomedical Engineering Conference*. 1996.

33. Kastelic, J., A. Galeski, and E. Baer, The multicomposite structure of tendon. Connect Tissue Res, 1978. **6**(1): p. 11-23.

34. Cheville, N.F., Utrastructural pathology: an introduction to interpretation. 1994: Wiley-Blackwell.

35. Wnek, G.E. and G.L. Bowlin, Encyclopedia of Biomaterials and Biomedical Engineering: A-K. 1 ed. 2004: Taylor & Francis, Inc. 1600.

36. Fung, Y.C., Biomechanics: Mechanical Properties of Living Tissues. 2nd ed. 1993, New York: Springer Verlag. 568.

37. Lindblom, A. and M. Paulson, Basement Membranes, in *Extracellular Matrix, Volume I, Tissue Function*, W.D. Comper, Editor. 1996, Hardwood academic publishers: Amsterdam, Netherlands.

38. Ottani, V., M. Raspanti, and A. Ruggeri, Collagen strucutre and functional implications. Micron, 2001. **32**: p. 251-260.

39. Kadler, Holmes, Trotter, and Chapman, Collagen fibril formation. Biochemistry Journal, 1996. **316**: p. 1-11.

40. Prockop and Fertala, The Collagen Fibril:The Almost Crystalline Structure. y. Journal of Structural Biolog, 1998. **122**: p. 111-118.

41. Diamant and e. al, Collagen; ultrastructure and its relation to mechanical properties as a function of aging. Proc R Soc Lond B, 1972. **180**: p. 293-315.

42. Hukins, D.W.L., Biomechanical properties of collagen, in *Collagen in Health and Disease*, J.B. Weiss and M.I.V. Jayson, Editors. 1982, Churchill Livingstone: Edinburgh, London New York.

43. Betsch, D.F. and E. Baer, Structure and mechanical properties of rat tail tendon. Biorheology, 1980. **17**(1-2): p. 83-94.

44. Baer, E., Hiltner, A., Friedman, B., Structural hierarchies and interactions in the tendon composite. Mechanics of Composite Materials, 1976. **12**(4): p. 619-629.

45. Kastelic, J., I. Palley, and E. Baer, A structural mechanical model for tendon crimping. J Biomech, 1980. **13**(10): p. 887-93.

46. Rowe, R.W., The structure of rat tail tendon fascicles. Connect Tissue Res, 1985. **14**(1): p. 21-30.

47. Yahia, L.H. and G. Drouin, Microscopical investigation of canine anterior cruciate ligament and patellar tendon: collagen fascicle morphology and architecture. J Orthop Res, 1989. **7**(2): p. 243-51.

48. Alexander, P., Extracellular Matrix Proteases & Protein Technical Guide. 2002. **2**.

49. Nagase, H., Matrix Metalloproteinases 1, 2, and 3: Substrate Specificities and Activation Mechanism, in *The Extracellular Matrix of the Uterus, Cervix and Fetal Membranes: Synthesis, Degradation and Hormonal Regulation*, P.C. Leppert and J.F. Woessner, Editors. 1991, Perinatology Press: Ithaca, NY.

50. Birkedal-Hansen, H., W.G. Moore, M.K. Bodden, L.J. Windsor, B. Birkedal-Hansen, A. DeCarlo, and J.A. Engler, Matrix metalloproteinases: a review. Crit Rev Oral Biol Med, 1993. **4**(2): p. 197-250.

51. Tam, E.M., Y.I. Wu, G.S. Butler, M.S. Stack, and C.M. Overall, Collagen binding properties of the membrane type-1 matrix metalloproteinase (MT1-MMP) hemopexin C domain. The ectodomain of the 44-kDa autocatalytic product of MT1-MMP inhibits cell invasion by disrupting native type I collagen cleavage. J Biol Chem, 2002. **277**(41): p. 39005-14.

52. Nagase, H., R. Visse, and G. Murphy, Structure and function of matrix metalloproteinases and TIMPs. Cardiovasc Res, 2006. **69**(3): p. 562-73.

53. Lei H, V.-O.F., Paavola, LG, Strauss, JF, 92-kDa gelatinase (matrix metalloproteinase-9) is induced in rat amnion immediately prior to parturition. Biology of Reproduction, 1995. **53**: p. 339-44.

54. Lei, M., H. Ghezzo, M.F. Chen, and D.H. Eidelman, Airway smooth muscle orientation in intraparenchymal airways. J Appl Physiol, 1997. **82**(1): p. 70-7.

55. Paavola, L., Furth, EE, Delgado, V, Boyd, CO, Jacobs, CC, Lei, H, Strauss JF, Striking changes in the structure and organization of rat fetal membranes precede parturition. Biology of Reproduction, 1995. **53**: p. 321-338.

56. Lei HF, F.E., Kalluri R, Chiou T, Tilly K, Tilly JL, Elkon KB, Jeffrey JJ, Strauss JF, A program of cell death and extracellular matrix degradation is activated in the amnion before the onset of labor. J Clin Invest, 1997. **98**: p. 1971-8.

57. Manabe Y, H.N., Fukumoto M, Tensile strength and collagen content of amniotic membrane do not change after the second trimester or during delivery. Obstet Gynecol, 1991. **78**(1): p. 24-7.

58. Malak TM, B.S., Structural characteristics of term human fetal membranes: a novel zone of extreme morhological alteration within the rupture site. Br J Obstet Gynaecol, 1994. **101**: p. 375-86.

59. McLaren, J., Taylor, D.J., Bell, S.C., Increased incidence of apoptosis in non-labor-affected cytotrophoblast cells in term fetal membranses the cervix. Human Reproduction, 1999. **14**: p. 2895-2900.

60. McLaren, J., Taylor, D.J., Bell, S.C., Increased Concentration of pro-matrix metalloproteinase 9 in term fetal membranes overylying the cervix befor labor: implications for membrane remodeling and rupture. American Journal of Obstetrics and Gynecology, 2000. **182**: p. 409-416.

61. El Khwad, M., Stetzer B., Moore, R.M., Kumar, D., Mercer, B., Arikat, S., Redline, R.W., Mansour, J.M., Moore, J.J., Term Human Fetal Membranes Have a Weak Zone Overlying the Lower Uterine Pole and Cervix Before Onset of Labor. Biology of Reproduction, 2005. **72**: p. 720-726.

62. El Khwad, M., Pandey, V., Stetzer, B., Mercer, B., Kumar, D., Moore, R.M., Fox, J., Redline, R.W., Mansour, J.M., Moore, J.J., Fetal Membranes From Term Vaginal Deliveries Have a Zone of Weakness Exhibiting Characteristics of Apoptosis and Remodeling. Journal for the Society of Gynecologic Investigation, 2006. **13**(3): p. 191-5.

63. Reti, N.G., Lappas, M., Riley, C., Wlodek, M., Permezel, M., Walker, S., Rice, G.E., Why do membranes rupture at term? Evidence of increased cellular apoptosis in the supracervical fetal membranes. American Journal of Obstetrics and Gynecology, 2007. **196**: p. 484.e1-484.e10.

64. Vadillo-Ortega, F., Gonzalez-Avila, G., Furth, E.E., Lei, H., Muschel, R.J., Stetler-Stevenson, W.G., Strauss, J.F. 3rd, 92-kd type IV collagenase (matrix metalloproteinase-9) activity in human amniochorion increases with labor. Am J Pathol, 1995. **146**(1): p. 148-56.

65. Atsuyuki, O., Hisashi, Y., Someya, A., Shigeru, I., Kinoshita, K., Nagaoka, I., Changes in Matrix Metalloproteinase 2 Activities in Amniochorions During Premature Rupture of Membranes. Journal of the Society for Gynecologic Investigation, 2006. **13**(8): p. 592-597.

66. Yonemoto, H., Young, C.B., Ross, J.T., Guilbert, L.L., Fairclough, R.J., Olson, D.M., Changesin Matrix Metalloproteinase (MMP)-2 and MMP-9 in the Fetal Amnion and Chorion During Gestation and at Term and Preterm Labor. Placenta, 2006. **27**: p. 669-677.

67. Goldman, S., Weiss, A., Shalev E., Differential activity of the gelatinases (matrix metalloproteinases 2 and 9) in the fetal membranes and decidua, associated with labour. Molecular Human Reproduction, 2003. **9**(6): p. 367-373.

68. Kumar, D., Fung, W., Moore, R.M., Pandey, V., Fox, J., Stetzer, B., Mansour, J.M., Mercer, B.M., Redline, R.W., Moore, J.J., Proinflammartory Cytokines Found in Amniotic Fluid Induce Collagen Remodeling, Apoptosis, and Biophysical Weakening of Cultured Human Fetal Membranes. Biology of Reproduction, 2006. **74**: p. 29-34.

69. Artal R, B.R., Hobel CJ, Hollister D, An in vitro model for the study of enzymatically mediated biomechanical changes in the chorioamniotic membranes. Am J Obstet Gynecol, 1979. **133**: p. 656-9.

70. Artal R, S.R., Neuman M, Burstein AH, Stojkov J, The mechanical properties of prematurely and non--prematurely ruptured membranes. Am J Obstet Gynecol, 1976. **125**(5): p. 655-9.

71. Oxlund, H., Helmig, R, Halaburt, JT, Uldbjerg, N, Biomechanical analysis of human chorioamniotic membranes. Eur J Obstet Gynecol Reprod Biol, 1990. **34**(3): p. 247-55.

72. Helmig R, O.H., Petersen LK, Uldbjerg N, Different biomechanical properties of human fetal membranes obtained before and after delivery. Eur J Obstet Gynecol Reprod Biol, 1993. **48**(3): p. 183-9.

73. Polishuk WZ, K.S., Peranio A, The physical properties of fetal membranes. Obstet Gynecol, 1962. **20**: p. 2004-10.

74. Parry-Jones E, P.S., A study of the elasticity and tension of fetal membranes and of the relation of the area of the gestational sac to the area of the uterine cavity. Br J Obstet Gynaecol, 1976. **83**(3): p. 205-12.

75. Al-Zaid NS, B.-R.M., Goldspink G, Bursting pressure and collagen content of fetal membranes and their relation to premature rupture of the membranes. Br J Obstet Gynaecol, 1980. **87**(3): p. 227-9.

76. Lavery JP, M.C., The viscoelastic nature of chorioamniotic membranes. Obstet Gynecol, 1977. **50**(4): p. 467-72.

77. Lavery JP, M.C., Deformation and creep in the human chorioamniotic sac. Am J Obstet Gynecol, 1979. **134**(4): p. 366-75.

78. Lavery JP, M.C., Knight RD, The effect of labor on the rheologic response of chorioamniotic membranes. Obstet Gynecol, 1982. **60**(1): p. 87-92.

79. Calvin, S.E. and M.L. Oyen, Microstructure and Mechanics of the Chorioamnion Membrane with an Emphasis on Fractrue Properties. Ann. N.Y. Acad. Sci, 2007. **1101**: p. 166-185.

80. MacLachlan, T.B., A method for the investigation of the strength of hte fetal membranes. American Journal of Obstetrics and Gynecology, 1965. **91**: p. 309-313.

81. Schober, E.A., Kusy, R.P., Whitley, J.Q., Savitz, D.A, Effect of thickness on the fracture characteristics of fetal membranes. Journal of Materials Science: Materials in Medicine, 1994. **5**: p. 130-137.

82. Schober, E.A., R.P. Kusy, and D.A. Savitz, Resistance of fetal membranes to concentrated force applications and reconciliation of puncture and burst testing. Ann Biomed Eng, 1994. **22**(5): p. 540-8.

83. Arikat, S., Novince, R.W., Mercer., B.M., Kumar, D., Fox, J.M., Mansour, J.M., Moore, J.M., Separation of amnion from choriodecidua is an integral event to the rupture of normal term fetal membranes and constitutes a significant component of the work required. American Journal of Obstetrics and Gynecology, 2006. **194**(1): p. 211-7.

84. Liao, H. and S.M. Belkoff, A failure model for ligaments. J Biomech, 1999. **32**: p. 183-188.

85. Natali, A.N., Pavan, P.G., Carniel, E.L., Lucisano, M.E., Taglialavoro, G., Anisotropic elasto-damage constitutive model for the biomechanical analysis of tendons. Medical Engineering and Physics, 2005. **27**: p. 209-214.

86. Natali, A.N., E.L. Carniel, P.G. Pavan, F.G. Sander, C. Dorow, and M. Geiger, A visco-hyperelastic-damage constitutive model for the analysis of the biomechanical response of the periodontal ligament. J Biomech Eng, 2008. **130**(3): p. 031004.

87. DeVita, R. and W.S. Slaughter, A constitutive law for the failure behavior of medial collateral ligaments. Biomechanical Modeling and Mechanobiology, 2007. **6**(3): p. 189-97.

88. Bartel, D.L., Davy, D.T., and Keaveny T.M., Orthopaedic Biomechanics Mechanics and Design in Musculoskeletal Systems. 2006, Upper Saddle River: Pearson Education, Inc. 371.

89. Layton, B.E. and A.M. Sastry, A mechanical model for collagen fibril load sharing in peripheral nerve of diabetic and nondiabetic rats. J Biomech Eng, 2004. **126**(6): p. 803-14.

90. Ionescu, I., Guilkey, J.E., Berzins, M., Kirby, R.M., Weiss, J.A, Simulations of Soft Tissue Failure Using the Material Point Method. Journal of Biomechanical Engineering, 2006. **128**: p. 917-924.

91. Volokh, K.Y., Prediction of arterial failure based on a microstructural bi-layer fiber-matrix model with softening. J Biomech, 2008. **41**(2): p. 447-53.

92. Slaughter, W.S. and M.S. Sacks, Modeling fatigue damage in chemically treated soft tissues. Functional Biomaterials, 2001. **198-1**: p. 255-260.

93. Donzelli, P.S., Spilker, R.L., Ateshian, G.A., Mow, V.C., Contact analysis of biphasic transversely isotropic cartilage layers and correlations with tissue failure. Journal of Biomechanics, 1999. **32**: p. 1037-1047.

94. Niebur, G.L., Feldstein, M.J., Keaveny, T.M., Biaxial Failure Behavior of Bovine Tibial Trabecular Bone. Journal of Biomechanical Engineering, 2002. **124**: p. 699-705.

95. Kosmopoulos, V. and T.S. Keller, Damage-based finite-element vertebroplasty simulations. European Spine Journal, 2004. **13**: p. 617-625.

96. Breuls, R.G., C.V. Bouten, C.W. Oomens, D.L. Bader, and F.P. Baaijens, A theoretical analysis of damage evolution in skeletal muscle tissue with reference to pressure ulcer development. J Biomech Eng, 2003. **125**(6): p. 902-9.

97. Pandey, V., Jaremko, K., Moore, R.M., Mercer, B.M., Stetzer, B., Kumar, D., Fox, J.M., Mansour, J.M., Moore, J.J, The force required to rupture fetal membranes paradoxically increases with acute in vitro repeated stretching. American Journal of Obstetrics and Gynecology, 2007. **196**(2): p. 165.e1-7.

98. Ellsmere, J.C., R.A. Khanna, and J.M. Lee, Mechanical loading of bovine pericardium accelerates enzymatic degradation. Biomaterials, 1999. **20**: p. 1143-1150.

99. Coulson, W.F., THE EFFECT OF PROTEOLYTIC ENZYMES ON THE TENSILE STRENGTH OF WHOLE AORTA AND ISOLATED AORTIC ELASTIN. BIOCHIMICA ET BIOPHYSICA ACTA, 1971. **237**: p. 378-386.

100. Huang, C. and I.V. Yannas, Mechanochemical Studies of Enzymatic Degradation of Insoluble Collagen Fibers. Journal of Biomedical Material Research Symposium, 1977. **8**: p. 137-154.

101. Joyce, E.M., J.J. Moore, and M.S. Sacks, Biomechanics of the fetal membrane prior to mechanical failure: review and implications. Eur J Obstet Gynecol Reprod Biol, 2009. **144 Suppl 1**: p. S121-7.

102. Freytes, D.O., Rundell, A.E., Vande Geest, J., Vorp, D.A., Webster, T.J., and Badylak, S.F., Analytically derived material properties of multilaminated extracellualr matrix devices using the ball-burst test. Biomaterial, 2005. **26**: p. 5518-5531.

103. Sacks, M.S., Biaxial mechanical evaluation of planar biological materials. Journal of Elasticity, 2000. **61**: p. 199-246.

104. McLaren J, M.T., Bell SC., Structural characteristics of term human fetal membranes prior to labor: identification of an area of altered morphology the cervix. Hum Reprod, 1999. **14**(1): p. 237-41.

105. Sacks, M.S., D.B. Smith, and E.D. Hiester, A small angle light scattering device for planar connective tissue microstructural analysis. Ann Biomed Eng, 1997. **25**(4): p. 678-89.

106. Cunningahm, F.G., McDonald, P.C., Leveno, K.S., Gant, N.F., Gilstrap, J., William's Obstetrics, ed. A.a. Lang. 1993, Norwalk, Conneticut.

107. Kubik-Huch, R.A., Wildermuth, S., Gettuzzi, L., Rake, A., Siefert, B., Chaoui, R., Marincek, B., Fetus and Uteroplacental Unit: Fast MR Imaging with Three-dimensional Reconstructuion and Volumetry - Feasibility Study. Radiology, 2001. **219**(2): p. 567-573.

108. Billiar, K.L. and M.S. Sacks, Biaxial mechanical properties of the natural and glutaraldehyde treated aortic valve cusp--Part I: Experimental results. Journal of Biomechanical Engineering, 2000a. **122**(1): p. 23-30.

109. Sacks, M.S. and C.J. Chuong, Orthotropic mechanical properties of chemically treated bovine pericardium. Ann Biomed Eng, 1998. **26**(5): p. 892-902.

110. Sacks, M.S., A method for planar biaxial mechanical testing that includes in-plane shear. J Biomech Eng, 1999. **121**(5): p. 551-5.

111. Stella, J.A., J. Liao, Y. Hong, W. David Merryman, W.R. Wagner, and M.S. Sacks, Tissue-to-cellular level deformation coupling in cell micro-integrated elastomeric scaffolds. Biomaterials, 2008. **29**(22): p. 3228-36.

112. Sacks, M.S., D.B. Smith, and E.D. Hiester, The aortic valve microstructure: effects of transvalvular pressure. Journal of Biomedical Materials Research, 1998. **41**(1): p. 131-41.

113. Reece, I.J., R. van Noort, T.R. Martin, and M.M. Black, The physical properties of bovine pericardium: a study of the effects of stretching during chemical treatment in glutaraldehyde. Ann Thorac Surg, 1982. **33**(5): p. 480-5.

114. Crofts, C.E. and E.A. Trowbridge, The tensile strength of natural and chemically modified bovine pericardium. Journal of Biomedical Materials Research, 1988. **22**: p. 89-98.

115. Zioupos, P., J.C. Barbenel, and J. Fisher, Mechanical and Optical Anisotropy of Bovine Pericardium. Medical and Biological Engineering and Computing, 1992. **30**: p. 76-82.

116. Sacks, M.S., A. Mirnajafi, W. Sun, and P. Schmidt, Bioprosthetic heart valve heterograft biomaterials: structure, mechanical behavior and computational simulation. Expert Rev Med Devices, 2006. **3**(6): p. 817-34.

117. Thorton, G.M., Schwab, T.D., and Oxlan, T.R., Cyclic loading causes faster rupture and strain rate than static loading in medial collateral ligament at high stress. Clinical Biomechanics, 2007. **22**: p. 932-940.

118. Millar, L.K., Stollber, J., DeBuque, L., Bryant-Greenwood, G., Fetal membrane distention: Determination of the intrauterine surface area and distention of the fetal membranes preterm and at term. American Journal of Obstetrics and Gynecology, 2000. **182**(1, Part1): p. 128-134.

119. Parry-Jones, E. and S. Priya, A study of the elasticity and tension of fetal membranes and of the relation of the area of the gestational sac to the area of the uterine cavity. Br J Obstet Gynaecol, 1976. **83**(3): p. 205-12.

120. Humphrey, J.D. and F.C.P. Yin, A new constitutive formulation for characterizing the mechanical behavior of soft tissues. Biophysical Journal, 1987. **52**: p. 563-570.

121. Sacks, M.S., Incorporation of experimentally-derived fiber orientation into a structural constitutive model for planar collagenous tissues. J Biomech Eng, 2003. **125**(2): p. 280-7.

122. Sacks, M.S., A method for planar biaxial testing that includes in-plane shear. Journal of Biomechanical Engineering, 1999. **121**: p. 551-555.

123. Sasaki, N. and S. Odajima, Elongation mechanism of collagen fibrils and force-strain relations of tendon at each level of structural hierarchy. J Biomech, 1996. **29**(9): p. 1131-6.

124. Sasaki, N. and S. Odajima, Stress-strain curve and Young's modulus of a collagen molecule as determined by the X-ray diffraction technique. Journal of Biomechanics, 1996. **29**: p. 655-658.

125. Liao, J., L. Yang, J. Grashow, and M.S. Sacks, The relation between collagen fibril kinematics and mechanical properties in the mitral valve anterior leaflet. J Biomech Eng, 2007. **129**(1): p. 78-87.

126. Artal R, S.R., Neuman M, Burstein AH, Stojkov J, The mechanical properties of prematurely and non--prematurely ruptured membranes. Am J Obstet Gynecol, 1979. **125**(5): p. 655-9.

127. Derganc, J., Bozic, B., Svetina, S., Bostjan, Z, Stability Analysis of Micropipette Aspiration of Neutrophils. Biophysical Journal, 2000. **79**: p. 153-162.

128. Humphery, J.D., Cardiovascular Solid Mechanics. 2002: Springer Verlag.

129. Purslow, P.P., T.J. Wess, and D.W. Hukins, Collagen orientation and molecular spacing during creep and stress-relaxation in soft connective tissues. J Exp Biol, 1998. **201**(Pt 1): p. 135-42.

130. Imai, K., Hiramatsu, A., Fukushima, D., Pierschbacher, M.,D., Okada, Y., Degradation of decorin by matrix metalloproteinases: identification of the cleavage sites, kinetic analysis and transforming growth factor-beta1 release. Biochem J, 1997. **322**: p. 809-814.

131. Sato, T., J. Keelan, and M. Mitchell, Critical paracrine interactions between TNF-alpha and IL-10 regulate lipopolysaccharide-stimulated human choriodecidual cytokine and prostaglandin E2 production. J Immunol, 2003. **170**(1): p. 158-66.